Stable Isotope Paleoaltimetry of the Peruvian Central Andes from the Miocene to Modern Using Hydrated Volcanic Glass

A Thesis
Presented in Partial Fulfillment of the Requirements for the
Degree of Master of Science
with a
Major in Geology
in the
College of Graduate Studies
University of Idaho
by

Emily J. White

Major Professor: Elizabeth Cassel, Ph.D.
Committee Members: Daniel Breecker, Ph.D.; Eric Mittelstaedt, Ph.D.; Jessica Stanley, Ph.D.
Department Administrator: Leslie Baker, Ph.D.

August 2019

AUTHORIZATION TO SUBMIT THESIS

This thesis of Emily J. White, submitted for the degree of Master of Science with a Major in Geology and titled "Stable Isotope Paleoaltimetry of the Peruvian Central Andes from the Miocene to Modern Using Hydrated Volcanic Glass" has been reviewed in final form. Permission, as indicated by the signatures and dates below, is now granted to submit final copies to the College of Graduate Studies for approval.

Major Professor: _____ Date: _____
Elizabeth Cassel, Ph.D.

Committee Members: _____ Date: _____
Daniel Breecker, Ph.D.

_____ Date: _____
Eric Mittelstaedt, Ph.D.

_____ Date: _____
Jessica Stanley, Ph.D.

Department Administrator: _____ Date: _____
Leslie Baker, Ph.D.

ABSTRACT

Topography is a dynamic reflection of the duration and characteristics of interdependent tectonic and climatic regimes. The growth of high elevations and high relief in large continental orogens, such as the Andes of South America and the Himalayas-Tibetan Plateau of Asia, drive substantial perturbations in global atmospheric circulation (Molnar and England, 1990) and dictate biodiversity (Raymo and Ruddiman, 1992). As a result, paleoclimate reconstructions and models of geodynamic drivers for surface uplift depend on the timing and style of the emplacement of these topographic features. The Central Andes are the type example of subduction-driven orogenesis and magmatism (Horton, 2018) and contain two parallel mountain chains, the Western and Eastern Cordillera, with mean elevations reaching 6 km. At the center of this orogen, the Altiplano-Puna plateau has a mean elevation of 4 km and covers a 600,000 km^2 area (Isacks, 1988), making it the highest subduction-driven plateau in the world (Decou et al., 2011). Despite the inherent importance of this region, the timing and style of surface uplift that led to the modern topography of the Central Andes is not well understood (Allmendinger et al., 1997; Garzione et al., 2017).

Proposed models for the timing of surface uplift range from late Oligocene to late Miocene (Garzione et al., 2017). Paleotopographic studies in the Central Andes have used a wide range of different tools, including stable isotope geochemistry, river incision modeling, genetic divergence, leaf morphology, and structural analysis to identify phases of surface uplift and make predictions about geodynamic drivers for uplift (Gregory-Wodzicki, 2000; Ghosh et al., 2006; Schildgen et al., 2007; Thouret et al., 2007; Garzione et al., 2008; Picard et al., 2008; Ehlers and Poulsen, 2009; Lease and Ehlers, 2013; Saylor and Horton, 2014; Kar et al., 2016). Current uplift models for the Central Andes include gradual, rapid, and non-uniform, surface uplift. Proposed geodynamic mechanisms for Andean orogenesis include contractional deformation (Hindle et al., 2005), removal of dense lower lithosphere and or crustal flow (Mamani et al., 2010), ablative subduction or thermal weakening (Isacks, 1988; Gosh et al., 2006), magmatic additions of mantle material (Sempere et al., 2008) and lithospheric delamination (Garizone et al., 2008). Several localized studies attribute paleoisotopic shifts to orogen-wide surface uplift, but this extrapolation has produced conflicting models for the timing of Central Andean surface uplift (Garzione et al., 2008;

Ehlers and Poulsen, 2009; Saylor and Horton, 2014). These models lack adequate constraints on the modern distribution of hydrogen and oxygen isotopes ratios across the orogen, which are necessary to reconstruct the specific timing and mechanisms of surface uplift. By sampling across the width of the orogen, it is possible to identify orogen-wide shifts in paleoisotopic values, which likely result from regional surface uplift or regional climatic changes.

The research presented in this thesis includes 1) a comparison of modern isotopic values of meteoric waters in soil and precipitation to hydrogen isotope values of meteoric waters extracted from volcanic glass and 2) hydrogen isotopic values of Miocene–modern volcanic glass samples across the Peruvian Central Andes to reconstruct the past distribution of isotopic values and identify regional drivers of paleoisotopic change (i.e., climate and/or surface uplift). Chapter I provides a general geologic overview of the Peruvian Central Andes with a focus on aspects that are pertinent to this study. Chapter II presents a comparison between several meteoric water proxies to quantify past elevations. Hydrogen (and oxygen, where possible) isotope values of meteoric water are compared between records that correspond to average rainfall over ca. 10,000 years (hydrated volcanic glass), ca. 5–10 years (soil water), and 2 years (precipitation). This modern isotopic dataset spans the width of the orogen, from the Pacific coast to the Amazon Basin. Comparison of these proxies enables reconstruction of how short- and long-term isotopic records change with respect to climatic variability and through time. Chapter III provides an assessment of the spatial distribution of past surface topography through time by directly comparing modern and ancient hydrogen isotope ratios of hydrated volcanic glasses in the Central Andes. This study provides new constraints on the timing of Peruvian Central Andean surface uplift.

ACKNOWLEDGEMENTS

I would like to thank the members of my committee, Drs. Elizabeth Cassel, Eric Mittelstaedt, Jessica Stanley, and Daniel Breecker. I also would like to thank Dr. Elizabeth Cassel, Dr. Brian Yanites, Dr. Daniel Breecker, Andrew Canada, Allyson White, Derry Xu, and Brigid Lynch, who traveled a long way to join me in the field in southern Peru and help with sample and data collection. My field seasons would not have been possible without their assistance. I am also thankful for great collaboration with Dr. Chris Poulsen, Phoebe Aron, and Dr. Daniel Breecker that allowed me to compile the research presented in Chapter II and III. My sincere thanks also go to Dr. Daniel Breecker, Dr. Jamie Barnes, Dr. Toti Larson, and Jeff Cullen for their guidance and support during volcanic glass δD analysis in the Light Stable Isotope Lab at the University of Texas-Austin. Dr. Daniel Stockli, Dr. Lisa Stockli, and Zach Foster-Baril also provided guidance and assistance with zircon U-Pb Geochronology in the UTChron facilities at the University of Texas-Austin.

Thank you to Terry Evans for always being there, for great conversation, and for helping me with all of the paperwork I could never keep track of. To Dr. Thomas Williams and Dr. Jerry Fairley - thank you for your support along the way. Also, to the many UI and WSU graduate students that made the past few years memorable, particularly Cody, Zach, Meg, Tom, Thomas, Courtney, Jeff, Ross, Gabi, and Bev.

I am very grateful to the funding organizations that provided immense support to many aspects of my research. This thesis is based upon work supported by the National Science Foundation Graduate Research Fellowship Program under Grant No. 1144254 and several student grants from the Geological Society of America, ExxonMobil, the Society for Sedimentary Geology, University of Idaho's Graduate & Professional Student Association, and the American Association of Women Geoscientists.

Finally, I would like to thank my family and friends, particularly my mom, dad, and sister who have supported me throughout this entire process. I will forever appreciate your love and encouragement. Most importantly, I wish to express my deepest gratitude to Andrew for his unconditional love, constant laughter, and endless support.

TABLE OF CONTENTS

LIST OF TABLES

LIST OF FIGURES

CHAPTER I

Introduction - Generalized Geologic Background of the Peruvian Central Andes, Southern Peru

MESOZOIC GEOLOGY

The Andes reflect a prolonged history of terrane accretion, magmatism, and contractional deformation. From the late Paleozoic to the mid-Cretaceous, predominant tensional deformation was accommodated through regional extension across much of western South America, which formed a marine backarc basin (Mamani et al., 2010). Carboniferous to Triassic magmatic arcs developed in this extensional environment (Boekhout et al., 2013). Extension during the Triassic has been attributed to the onset of late Paleozoic orogen collapse (Dewey, 1988; Mpodozis and Kay, 1992; Ramos, 2009) associated with an intracontinental rift system (Kontak et al., 1990; Sempere et al., 2002) or backarc extension (Noble et al., 1978; Reitsma, 2012). The Late Triassic landward migration of magmatic arc activity occurred with emplacement of intrusive rocks of the Chocolate Formation (310–91 Ma), including diorite, tonalite, granodiorite, monzonite, and intermediate rocks (Mukasa, 1986a; Clark et al., 1990; Mamani et al., 2010). Intrusion of these rocks over a prolonged period of magmatism may reflect an increased plate convergence rate and subsequent trench rollback (Ramos, 1988a).

At ~200 Ma, the Nazca plate began to subduct along a large portion of the Andean margin, initiating orogenesis and magmatism that continues today (Haschke et al., 2006; Decou et al., 2013; Boekhout et al., 2013). High-magnitude shortening of rocks across the Central Andes since the Late Jurassic progressively built high topography of the Western Cordillera (McQuarrie, 2002; Long, 2012). Periods of intensified thrusting are potentially associated with variations in the convergence rate of the Nazca plate beneath the South American continent (Isacks, 1988; Oncken et al., 2006). Backarc rifting during the Jurassic considerably widened and deepened a backarc basin as the magmatic arc migrated trenchward

to the present-day coastline (Sempere et al., 2002; Demouy et al., 2012; Boekhout et al., 2013).

CENOZOIC GEOLOGY

Southern Peru has been a tectonically and magmatically active region since the Late Cretaceous as a result of active subduction along the western continental margin (Pardo-Casas and Molnar, 1987; Somoza, 1998). The Toquepala arc (91–45 Ma) was the first continental arc produced from subduction of the Nazca Plate in Peru and is associated with emplacement of the Coastal Peruvian batholith (Mukasa, 1986b; Decou et al., 2011). During this arc magmatism, there was steep subduction at the Andean margin and a rapid acceleration in convergence rate from ~5 cm/yr at ~60 Ma to ~15 cm/yr by ~40 Ma (Pardo-Casas & Molnar, 1987; Somoza, 1998). Accelerated plate convergence led to reactivation of arc volcanism at this time (Mukasa, 1986a). The Eocene transition from the Toquepala arc to the Andahuaylas-Anta arc is defined by a ca. 150 km northward migration of the magmatic arc (Mamani et al., 2010). This transition likely caused extension in the forearc (Decou et al., 2011) that created a number of basins in the backarc, arc, and forearc and fragmented or terminated existing basins (Sempere et al., 2008; Mamani et al., 2010). Initiation of the Andahuaylas-Anta arc (45–30 Ma) is interpreted to accompany shallowing of the subducting slab and a decrease in convergence rate to ~6 cm/yr (Somoza, 1998). These changes caused strong interplate coupling, crustal shortening, and decreased volcanic activity inboard of previous arc volcanism (Noble et al., 1978; Somoza, 1998; Roperch et al., 2006; Oncken et al., 2006; Mamani et al., 2010). Substantial broadening of southern Peru occurred after ~30 Ma, as the active arc extended across much of the present plateau (Allmendinger et al. 1997; Wörner et al. 2000; Haschke et al., 2002). This was accompanied by major crustal thickening generated through oroclinal bending in the forearc (Roperch et al., 2006).

During the mid-Oligocene, magmatism expanded over a larger area due to westward migration of the Tacaza arc (30–24 Ma) system as a result of slab steepening (Mamani et al., 2010) and increased convergence rates of ~15 cm/yr (Somoza, 1998). Slab steepening induced mantle upwelling and decompression that led to heating of the lower crust (Mamani et al., 2010) and eruption of voluminous high-potassium mafic lavas (Trumbull et al., 2006;

Roperch et al., 2006). Westward migration of the arc continued through the Huaylillas, Barroso, Upper Barroso, and current magmatic arcs (Fornari et al., 2002; Mamani et al., 2010). In the early Miocene, the Huaylillas arc (24–10 Ma) continued to progress west and is marked by the most extensive and voluminous ignimbrites to be deposited in southern Peru and northern Chile (Wörner et al. 2000). The Barroso arc (10–3 Ma) was located close to the modern-day arc on its western edge but is distinguished by widespread volcanism caused by low convergence rates in the Central Andes (Somoza, 1998; Mamani et al., 2010). The Upper Barroso arc (3–1 Ma) was narrower than the Barroso arc because the eastern limb of the Barroso arc moved west at this time. This arc is represented by various stratovolcanoes and smaller mafic lava fields along the Western Cordillera (Mamani et al., 2010).

MODERN STRUCTURE OF THE CENTRAL ANDES

The Andean belt is segmented into the Northern Andes, Central Andes, and Southern Andes, which, in total, extend along the entire length of western South America. The Central Andes are further segmented into the Northern Central Andes (5°S–13°S), Central Andean orocline (13°S–28°S), and Southern Central Andes (28°S–37°S) (Fig. 1.1; Horton, 2018). In the Central Andes, the Nazca plate currently subducts at a 30º angle and converges at a rate of ~ 8 cm/yr resulting in active arc volcanism (Somoza, 1998). In two discrete segments, the Nazca plate is subducting at a 5–10º angle beneath the South American plate (2–15°S and 28°–33°30′S; Gregory-Wodzicki, 2000; Hampel, 2002). These “flat slab zones” are marked by a lack of recent volcanic activity and are interpreted as products of subduction of the Nazca Ridge and the Juan Fernández Ridge starting at ca. 11 Ma (Gregory-Wodzicki, 2000; Hampel, 2002). Southern Peru is located within the Central Andean orocline segment of the Central Andes and is situated between these two flat slab zones.

The Central Andean orocline is comprised of a forearc region (Coastal Cordillera), magmatic arc (Western Cordillera), hinterland (Altiplano), retroarc fold-thrust belt (Eastern Cordillera), and modern fold-thrust belt in the foreland basin system (Sub-Andean zone) (Figs. 1.1 and 1.2; Beck et al., 1996; Horton and DeCelles, 1997). The forearc consists of remnants from the Mesozoic volcanic arc and a forearc depression known as the Pacific Piedmont (Gregory-Wodzicki, 2000). The modern magmatic arc sits ~230 km east of the

trench within the Western Cordillera and encompasses many young stratovolcanoes with dacitic to andesitic lavas and pyroclastic rocks (Mamani et al., 2010). Crustal thicknesses in the Western Cordillera are ≥ 70 km locally based on seismic array data (Beck and Zandt, 2002) and modern elevations reach up to 6 km. The Altiplano is an internally drained basin situated between the Western Cordillera and the Eastern Cordillera (Allmendinger et al., 1997; Gregory-Wodzicki, 2000). The Altiplano plateau has mean elevations of 3.6 km and crustal thicknesses of > 55 km (Beck et al., 1996). The Eastern Cordillera is the product of crustal thickening (~70 km mean crustal thickness) and a locus of surface uplift since the Late Cretaceous (Decou et al., 2013). In the Sub-Andean zone, the foreland system consists of an active thin-skinned fold-thrust belt in eastern Peru and a foreland basin in Brazil and Bolivia (Allmendinger et al., 1997).

REFERENCES

Allmendinger, R.W., Jordan, T.E., Kay, S.M., and Isacks, B.L., 1997. The evolution of the Altiplano-Puna Plateau of the central Andes. Annual Review of Earth and Planetary Sciences, 25, 139–174.

Alván, A., von Eynatten, H., Dunkl, I., and Gerdes, A., 2015. Zircon U–Pb geochronology and heavy mineral composition of the Camaná Formation, southern Peru: Constraints on sediment provenance and uplift of the Coastal and Western Cordilleras. Journal of South American Earth Sciences, 61, 14–32.

Beck, S.L., and Zandt, G., 2002. The nature of orogenic crust in the central Andes. Journal of Geophysical Research: Solid Earth, 107, 107 (B10).

Beck, S.L., Zandt, G., Myers, S.C., Stephen, C., Wallace, T.C., and Silver, P.G., 1996. Crustal thickness variations in the central Andes. Geology, 24, 407–411.

Boekhout, F., Sempere, T., Spikings, R., and Schaltegger, U., 2013. Late Paleozoic to Jurassic chronostratigraphy of coastal southern Peru: Temporal evolution of sedimentation along an active margin. Journal of South American Earth Sciences, 47, 179–200.

Clark, A.H., Farrar, E., Kontak, D.J., Langridge, R.J., Arenas, M.J., France, L.J., McBride, S.L., Woodman, P.L., Wasteneys, H.A., Sandeman, H.A., and Archibald, D.A., 1990. Geologic and geochronologic constraints on the metallogenic evolution of the Andes of southeastern Peru. Economic Geology and the Bulletin of the Society of Economic Geologists, 85, 1520–1583.

Decou, A., von Eynatten, H., Dunkl, I., Frei, D., and Wörner, G., 2013. Late Eocene to Early Miocene Andean uplift inferred from detrital zircon fission track and U-Pb dating of Cenozoic forearc sediments (15–18ºS). Journal of South American Earth Sciences, 45, 6–23.

Decou, A., von Eynatten, H., Mamani, M., Sempere, T., and Wörner, G., 2011. Cenozoic forearc basin sediments in Southern Peru (15–18ºS): Stratigraphic and heavy mineral constraints for Eocene to Miocene evolution of the Central Andes. Sedimentary Geology, 237, 55–72.

Demouy, S., Paquette, J.-L., de Saint Blanquat, M., Benoit, M., Belousova, E.A., O'Reilly, S.Y., García, F., Tejada, L.C., Gallegos, R., and Sempere, T., 2012. Spatial and

temporal evolution of Liassic to Paleocene arc activity in southern Peru unraveled by zircon U-Pb and Hf in-situ data on plutonic rocks. Lithos, 155, 183–200.

Dewey, J.F., 1988. Extensional collapse of orogens. Tectonics, 7 (6), 1123–1139.

Ehlers, T.A., and Poulsen, C.J., 2009. Influence of Andean uplift on climate and paleoaltimetry estimates. Earth and Planetary Science Letters, 281, 238–248.

Fornari, M., Baldellón, E., Espinoza, F., Ibarra, I., Jiménez, N., and Mamani, M., 2002. Ar-Ar dating of late Oligocene-early Miocene volcanism in the Altiplano, *in* 5th International Symposium on Andean Geo dynamics: Paris, Institut de recherché pour le développe ment and Université Paul Sabatier, Extended abstract, 223–226.

Garzione, C.N., Gregory, H., Libarkin, J., Withers, S., MacFadden, B., Eiler, J., Ghosh, P., Mulch, A., 2008. The Rise of the Andes. Science, 320, 1304–7.

Garzione, C.N., McQuarrie, N., Perez, N.D., Ehlers, T.A., Beck, S.L., Kar, N., Eichelberger, N., Chapman, A.D., Ward, K.M., Ducea, M.N., Lease, R.O., Poulsen, C.J., Wagner, L.S., Saylor, J.E., Zandt, G., and Horton, B.K., 2017. Tectonic Evolution of the Central Andean Plateau and implications for the growth of plateaus. Annual Review of Earth and Planetary Sciences, 45, 529–559.

Gregory-Wodzicki, K.M., 2000. Uplift history of the Central and Northern Andes: A review. Geological Society of America Bulletin, 112, 1091–1105.

Ghosh, P., Garzione, C.N., and Eiler, J.M., 2006. Rapid uplift of the Altiplano revealed through 13C–18O bonds in paleosol carbonates. Science, 311, 511–515.

Hampel, A., 2002. The migration history of the Nazca Ridge along the Peruvian active margin: A re-evaluation. Earth and Planetary Science Letters, 203, 665–679.

Haschke, M.R., Siebel, W., Günther, A., and Scheuber, E., 2002. Repeated crustal thickening and recycling during the Andean orogeny in north Chile (21º–26ºS). Journal of Geophysical Research, 107, 1–18.

Haschke, M., Sobel, E.R., Blisniuk, P., Strecker, M.R., and Warkus, F., 2006. Continental response to active ridge subduction. Geophysical Research Letters, 33 (15).

Horton, B.K., 2018. Tectonic regimes of the central and southern Andes: Responses to variations in plate coupling during subduction. Tectonics, 37, 402–429.

Isacks, B.L., 1988. Uplift of the Central Andean Plateau and bending of the Bolivian Orocline. Journal of Geophysical Research, 93 (B4), 3211–3231.

Kar, N., Garzione, C.N., Jaramillo C., Shanahan, T., Carlotto, V., Pullen, A., Moreno, F., Anderson, V., Moreno, E., and Eiler, J., 2016. Rapid regional surface uplift of the northern Altiplano plateau revealed by multiproxy paleoclimate reconstruction. Earth and Planetary Science Letters, 447, 33–47.

Kontak, D.J., Farrar, E., Clark, A., and Archibald, D.A., 1990. Eocene tectono-thermal rejuvenation of an upper Paleozoic-lower Mesozoic terrane in the Cordillera de Carabaya, Puno, southeastern Peru, revealed by K-Ar and 40Ar/39Ar dating. Journal of South American Earth Sciences, 3, 231–246.

Lease, R,O., and Ehlers, T.A., 2013. Incision into the eastern Andean Plateau during Pliocene cooling. Science, 341, 774–776.

Long, S.P., 2012. Magnitudes and spatial patterns of erosional exhumation in the Sevier hinterland, eastern Nevada and western Utah, USA: Insights from a Paleogene paleogeographic map. Geosphere, 8, 881–901.

Mamani, M., Worner, G., and Sempere, T., 2009. Geochemical variations in igneous rocks of the Central Andean orocline (13ºS to 18ºS): Tracing crustal thickening and magma generation through time and space. Geological Society of America Bulletin, 122, 162–182.

McQuarrie, N., 2002. The kinematic history of the central Andean fold-thrust belt, Bolivia: Implications for building a high plateau. Geological Society of America Bulletin, 114 (8), 950–963.

Molnar, P., and England P., 1990. Late Cenozoic uplift of mountain ranges and global climatic change: Chicken or egg?. Nature, 346, 29–34.

Mpodozis, C., and Kay, S.M., 1992. Late Paleozoic to Triassic evolution of the Gondwana margin- evidence from Chilean Frontal Cordilleran batholiths (28°S to 31°S). Geological Society of America Bulletin, 104 (8), 999–1014.

Mukasa, S.B., 1986a. Zircon U-Pb ages of super-units in the Coastal Batholith, Peru: Implications for magmatic and tectonic processes. Geological Society of America Bulletin, 97, 241–254.

Mukasa, S.B., 1986b. Common Pb isotopic compositions of the Lima, Arequipa and Toquepala segments in the Coastal Batholith, Peru: Implication for magma genesis. Geochimica et Cosmochimica Acta, 50, 771–782.

Noble, D.C., Silberman, M.L.,Mégard, F., and Bowman, H.R., 1978. Comendite (peralkaline rhyolites) in the Mitu Group, central Peru: evidence of Permian–Triassic extension in the Central Andes. United States Geological Survey Journal of Research, 6, 453–457.

Oncken, O., Hindle, D., Kley, J., Elger, K., Victor, P., and Schemmann, K., 2006. Deformation of the central Andean upper plate system-facts, fiction, and constraints for plateau models. In: Oncken, O., et al., eds., The Andes. Frontiers in Earth Sciences, Springer, Berlin, 3–27.

Pardo-Casas, F., and Molnar, P., 1987. Relative motion of the Nazca (Farallon) and South American plates since Late Cretaceous time. Tectonics, 6, 233–248.

Picard, D., Sempere, T., and Plantard, O., 2008. Direction and timing of uplift propagation in the Peruvian Andes deduced from molecular phylogenetics of highland biotaxa. Earth and Planetary Science Letters, 271, 326–336.

Ramos, V.A., 1988a, Tectonics of the Late Proterozoic-early Paleozoic: A collisional history of southern South America. Episodes, 11 (3), 168–174.

Ramos, V.A., 2009. Anatomy and global context of the Andes: Main geologic features and the Andean orogenic cycle. In: Kay, S.M., Ramos, V.A., and Dickinson, W.R., eds., Backbone of the Americas: Shallow Subduction, Plateau Uplift, and Ridge and Terrane Collision. Geological Society of America Memoir, 204, 31–65.

Raymo, M.E., and Ruddiman W.F., 1992. Tectonic forcing of late Cenozoic climate. Nature, 359, 117–122.

Reitsma, M.J., 2012. Reconstructing the late Paleozoic: Early Mesozoic plutonic and sedimentary record of south-east Peru: Orphaned back-arcs along the western margin of Gondwana (PhD Thesis). University of Geneva, 246.

Roperch, P., Sempere, T., Macedo, O., Arriagada, C., Fornari, M., Tapia, C., García, M., and Laj, C., 2006. Counterclockwise rotation of late Eocene-Oligocene fore-arc deposits in southern Peru and its significance for oroclinal bending in the central Andes. Tectonics, 25, TC3010.

Sempere, T., Carlier, G., Soler, P., Fornari, M., Carlotto, V., Jacay, J., Arispe, O., Neraudeau, Cardenas, J., Rosas, S., and Jimenez, N., 2002. Late Permian-Middle Jurassic lithospheric thinning in Peru and Bolivia, and its bearing on Andean-age tectonics. Tectonophysics, 345 (1–4), 153–181.

Sempere, T., Folguera, A., and Gerbault, M., 2008. New insights into the Andean evolution: An introduction to contributions from the 6th ISAG symposium (Barcelona, 2005). Tectonophysics, 459, p. 1–13.

Schildgen, T.F., Hodges, K.V., Whipple, K.X., Reiners, P.W., and Pringle, M.S., 2007. Uplift of the western margin of the Andean plateau revealed from canyon incision history, southern Peru. Geology, 35, 523–526.

Somoza, R., 1998. Updated Nazca (Farallon)-South America relative motions during the last 40 My: Implications for the mountain building in the Central Andean region. Journal of South American Earth Sciences, 11, 211–215.

Thouret, J.C., Wörner, G., Gunnell, Y., Singer, B., Zhang, X., and Souriot, T., 2007. Geochronologic and stratigraphic constraints on canyon incision and Miocene uplift of the Central Andes in Peru. Earth and Planetary Science Letters, 263, 151–166.

Trumbull, R., Riller, U., Oncken, O., Scheuber, E., Munier, K. and Hongn, F., 2006. The time-space distribution of Cenozoic arc volcanism in the Central Andes: A new data compilation and some tectonic considerations. In: Oncken, O., et al., eds., The Andes. Frontiers in Earth Sciences, Springer, Berlin, 29–43.

Wörner, G., Hammerschmidt, K., Henjes-Kunst, F., Lezaun, J., and Wilke, H., 2000. Geochronology (40Ar-39Ar-, K-Ar-, and He-exposure-) ages of Cenozoic magmatic rocks from northern Chile (18º–22ºS). Implications for magmatism and tectonic evolution of the Central Andes. Revista Geológica de Chile, 27, 205–240.

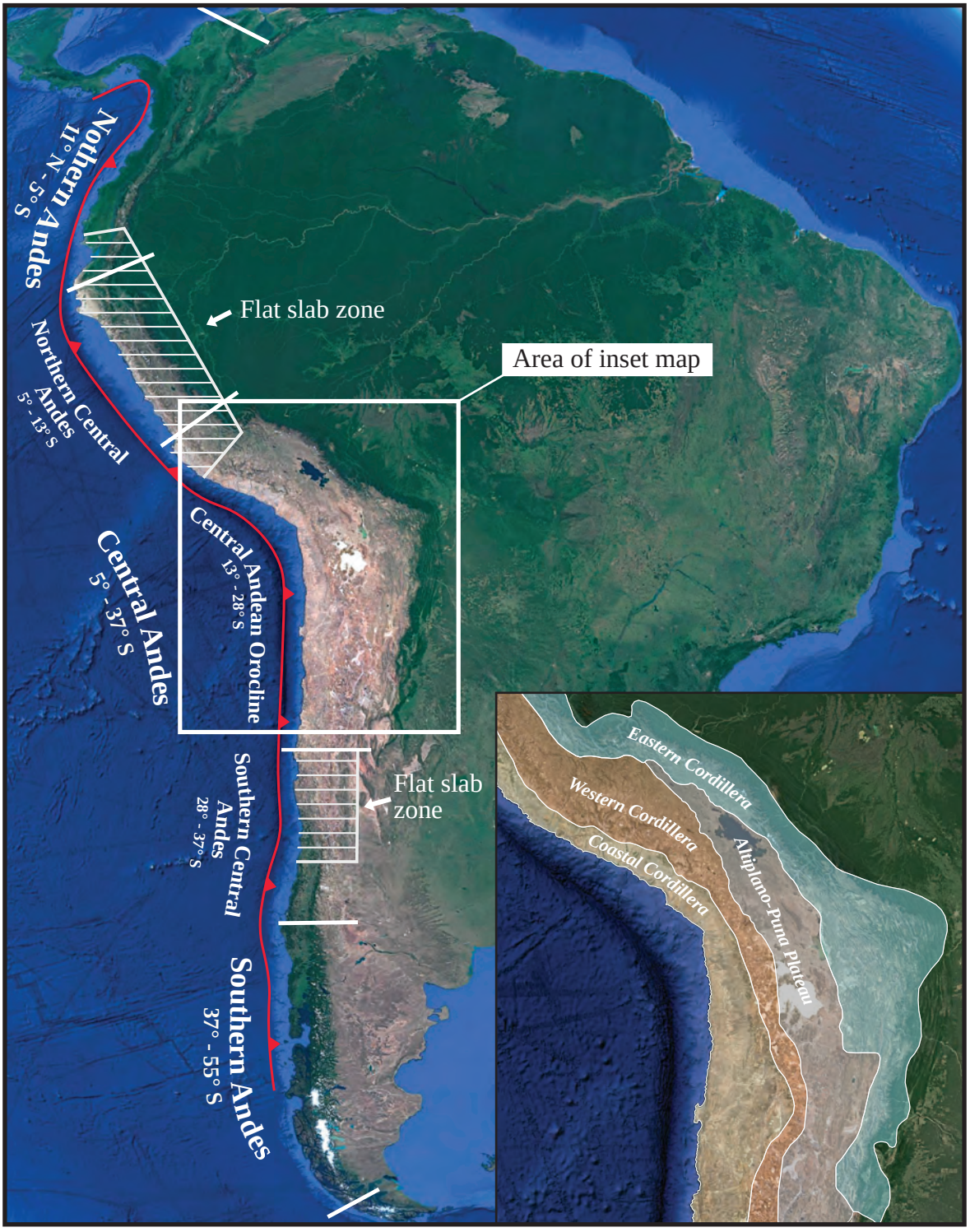

Figure 1.1. Map of South America displaying latitudinal subdivisions of the Andes (e.g., Horton, 2018). The map also displays the location of the two "flat slab zones" (e.g., Gregory-Wodzicki, 2000; Hampel, 2002), the Altiplano-Puna Plateau, and the trench location of the subducting Nazca Plate. Inset: map of physiographic regions in the Central Andes.

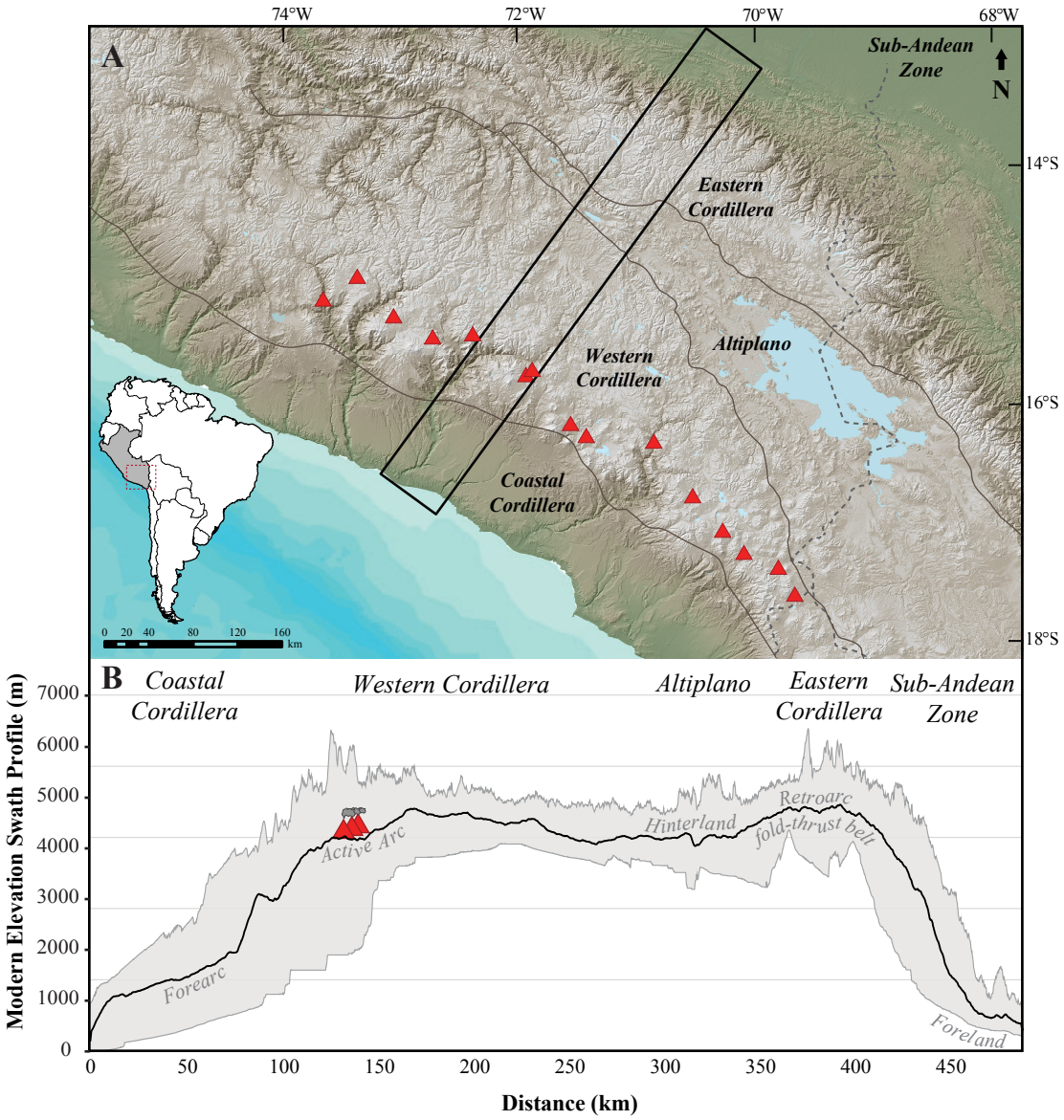

Figure 1.2. A) Map of Southern Peru displaying location of current magmatic arc (red triangles) and Coastal Cordillera, Eastern and Western Cordillera, Altiplano, and Sub-Andean zone boundaries. Swath profile (in B) outlined in black box. B) Modern elevation swath profile across study area in the Peruvian Central Andes.

CHAPTER II

A Comparison of Modern Meteoric Water Proxies in the Peruvian Central Andes, Southern Peru

ABSTRACT

Reliable paleoaltimetric reconstructions of the Peruvian Central Andes are dependent on characterization of how isotopic lapse rates change through time. Paleoisotopic studies that contain spatially distributed data derived from multiple isotopic proxies yield the best constraints on sources of observed paleoisotopic variability. This is particularly true when fractionation differences between these different isotopic systems and proxies are quantified. Here we compare hydrogen isotope ratios of modern hydrated volcanic glass from ≤ 5 Ma tuffs to hydrogen and oxygen isotope ratios of modern soil water and precipitation, all from samples collected across the Peruvian Central Andes. These data constitute the first orogen-wide isoscape using these three proxies. Hydrogen isotope ratios (δD) from volcanic glass within the Coastal Cordillera of the Peruvian Central Andes show moisture recycling at low coastal elevations (< 2500 m). Soil water and precipitation δD values from the eastern slope of the Eastern Cordillera are consistent with rainout of Atlantic-derived air masses between the Amazon Basin and the high peaks of the Eastern Cordillera. In the Western Cordillera, δD values of meteoric waters extracted from volcanic glasses and soils indicate modern mixing between Pacific-derived air masses and Atlantic-derived air masses. This indicates Pacific-derived air masses are an important control on modern meteoric water δD values in the Peruvian Central Andes and should therefore be considered in studies of Central Andean paleoaltimetry.

INTRODUCTION

Paleotopographic studies commonly use variations in stable isotope ratios of H, C, and O within a variety of proxies to assess phases of surface uplift (e.g., Garzione et al., 2006; Ghosh et al., 2006; Picard et al., 2008; Saylor and Horton, 2014; Kar et al., 2016).
To quantify sources of isotopic variability of past records, we first measure modern stable isotopic values of hydrogen and oxygen in various meteoric water proxies to generate an isotopic profile of the modern Peruvian Central Andes. The modern spatial distribution of stable isotopes of meteoric waters across an orogen can inform past temporal variations in stable isotopic distributions that give insight into paleoelevation models. The Peruvian Central Andes contain the internally drained Altiplano plateau, which is separated from the Pacific coast by the Western Cordillera and from the Amazon rainforest by the Eastern Cordillera. Air mass trajectories generated from global climate models have limited resolution relative to the scale of the Andes to fully quantify the control on isotopic distributions through seasonality and precipitation contribution of the two air masses (Pacific and Atlantic derived) present in the Central Andes (Minvielle and Garreaud, 2011). A range of climatic parameters can also affect the spatial distribution of isotope values of precipitation in this region. For example, many inland regions are characterized by significant evaporation, which can lead to fractionation of raindrops as they descend or of meteoric water on the land surface (Stewart, 1975; Gat and Airey, 2006; Yamada and Uyeda, 2006). In addition, moisture recycling from evapotranspiration can sustain rainout across a region by resupplying water back into an air mass (Yoshimura et al., 2003; Davie, 2008; Peng et al., 2011). Air mass mixing of moisture sources may also cause spatial or seasonal variability (Tian et al., 2007; Noone, 2012). These potential complications can lead to deviations from a predictive Rayleigh distillation model (Bershaw et al., 2016) by increasing isotopic values of meteoric water supplied by air masses.

The Central Peruvian climate is currently shaped by westerly Pacific-derived air masses and dominant easterly Atlantic-derived air masses (Garreaud, 2000). Upwards of 70% of annual precipitation in southern Peru occurs during the austral summer (December-February) (Minvielle and Garreaud, 2011; Sulca, 2016). During the austral summer, easterly winds bring most of the moisture across the Altiplano, but westerly winds capable of producing measurable precipitation also reach the Altiplano (Vuille, 1999; Garreaud et al.,

2003). The isotopic distribution of meteoric waters across the high topographic region in the Peruvian Central Andes is therefore dependent on where these air masses meet and how much precipitation is contributed from each air mass.

We use hydrated volcanic glass, precipitation, and soil water to quantify the modern isotopic distributions of meteoric waters across the Central Andes in southern Peru. Hydrated volcanic glass has proven utility as a proxy for paleo-meteoric waters (e.g., Cassel et al., 2014, 2018; Pingel et al., 2016; Jackson et al., 2019) and yields isotopic data that can be compared with other proxies (Dettinger et al., 2015). Precipitation (this study and the International Atomic Energy Agency (IAEA) database) and soil water datasets enable compilation of varied and spatially extensive isotopic data. Inter-proxy comparison is particularly informative because volcanic glass represents hydration and isotopic equilibration over 1–10 thousand years (Cassel and Breecker, 2017), soil water represents mean isotopic values over ca. 5–10 years, and this precipitation record represents a multi-season average weighted mean over 2 years. It is therefore important to consider any short-term climatic variability that may impose a strong effect on precipitation data, such as seasonality or precipitation amount.

METHODS

For this study, we use stable isotope paleoaltimetry to quantify how the ≤ 5 Ma paleoisotopic record relates to the modern topography of the Peruvian Central Andes. Stable isotope paleoaltimetry is based on the progressive depletion of deuterium (^{2}H) and oxygen-18 (^{18}O) relative to hydrogen-1 (^{1}H) and oxygen-16 (^{16}O) in air masses with increasing elevation (Dansgaard, 1964; O'Neil, 1986). As an air mass rises and adiabatically cools, it preferentially precipitates water with a higher deuterium to hydrogen and oxygen-18 to oxygen-16 ratio (Merlivat and Nief, 1967), resulting in progressive depletion (lower δD and $\delta^{18}O$ values) of the residual vapor source. The relationship between the hydrogen and oxygen isotope values of precipitation is linear (Craig, 1961), so both isotopic systems can be used and compared between paleoaltimetric proxies. Volcanic glass records the isotopic composition of meteoric water as glass hydrates (Friedman et al. 1993; Cassel and Breecker, 2017). Glass hydration occurs through diffusion of meteoric water into the glass structure and exchange of soluble

cations for H and O within the glass (Fig. 2.1; Cerling et al., 1985; Valle et al., 2010; Gin et al., 2013). Subsequent silicate bonding prevents further exchange with ambient water and results in an outer, nanoporous silica layer that effectively traps the isotopic signature of meteoric water during the hydration period (Cailleteau et al., 2008; Parruzot et al., 2015). Through this process, volcanic glass starts with 0.1–0.5 wt.% magmatic water in the glass structure when erupted (Giachetti et al., 2015) and gain up to 10 wt.% meteoric water within 10,000 years (Giachetti et al., 2015; Cassel and Breecker, 2017).

We sampled unwelded ignimbrites and ash-fall tuffs deposited from ca. 0.5 to 5 Ma as well as modern soil and precipitation at a wide range of elevations and across a large spatial extent of the Peruvian Central Andes (Fig. 2.2). Volcanic glass was separated using standard metal-free crushing, sieving, acid abrasion, magnetic separation, and density separation techniques as discussed in Cassel and Breecker (2017). This procedure was slightly modified for ≤ 5 Ma pumiceous glass samples by reducing acid abrasion time to avoid acid pitting. To separate volcanic glass, samples were crushed and sieved to 70–150 μm size fractions and then acid washed three times for 30 sec in 10% HCl and twice for 10–15 sec in 8% HF to remove carbonate and clay. Glass was then separated from the remaining non-magnetic phenocrysts (e.g. quartz and feldspar) using methylene iodide (MI) with a specific gravity of 3.32. This density separation was completed through gradual addition of acetone to produce density layers that correspond to the highly variable density of glass within samples (700–2450 kg/m^3; Shipley and Sarna-Wojcicki, 1982). To reduce contamination from sources of non-meteoric water (i.e., fluid inclusions and hydrous minerals; Moore, 2008), all analyzed separates consisted of ≥ 98% glass. Many samples were density-separated multiple times to achieve this high purity because of the widely variable character of glass shards within samples.

Isotopic analyses of volcanic glass and soil water were completed in the Light Stable Isotope Lab at The University of Texas-Austin. Prior to all analyses, ~3 mg glass separates were packed in Ag capsules and vacuum heated at 75 °C for at least 12 hr to eliminate remnant surface water. Replicate aliquots (n = 3) of each sample were analyzed to ensure precise reproduction of isotopic ratios. Hydrogen isotope ratios of volcanic glasses were determined using a TC/EA coupled with a MAT 253 gas source isotope ratio mass spectrometer (IRMS) and calibrated using international standards NBS 30 (biotite), USGS-57

(biotite), USGS-58 (muscovite), NBS-22 (oil), IAEA CH-7 (polyethylene foil), and IAEA-CH-3 (cellulose) as well as two internal volcanic glass standards (Table A1). The uncertainty used for each glass sample was either the 2σ analytical precision of mass spectrometer based on NBS-22 or the 2σ uncertainty of sample replicates, whichever was greater for each glass sample. The NBS-22 standard was used for error assessment because of its homogeneity and pyrolization efficiency.

Glass values were shifted to account for the known fractionation between meteoric water and volcanic glass during the hydration process (Friedman et al., 1993). To calculate the fractionation between meteoric water and volcanic glass, we compared hydrogen isotope ratios of hydrated volcanic glass to soil water δD values from samples collected from the same location. We determined an average fractionation ($10^3 \ln\alpha_{\text{glass-water}}$) for the region of -16.06‰ (± 5.99; 1σ). We used this fractionation factor to back-calculate the original δD values of meteoric waters available to hydrate glasses at the time of volcanic glass deposition. Unlike previous studies that use precipitation δD values for environmental water in the calculation of fractionations (Friedman et al., 1993; Seligman et al., 2016), we use soil water because it represents a longer-term average for modern environmental water. Soil water is also likely subject to the same surface processes that are present during the hydration of volcanic glass (e.g., evaporation). The main difference between these two proxies is that glasses (≤ 5 Myr) record longer-term seasonal variations than soil waters collected from the same location.

Soil samples were collected across the width of the Peruvian Central Andes, 5–418 km from the Pacific coast (Figs. 2.2 and 2.3). Where possible, soils were collected near tuff samples to permit direct correlation. Soil pits targeted unirrigated soils away from recent stream floodplains and were excavated to a depth of 80–100 cm. Soil samples were collected in glass tubes and immediately sealed with a rubber stopper and wax film to prevent exchange with the atmosphere and were collected every 20 cm during excavation to minimize evaporation. We utilize samples collected at depths of ≥ 50 cm to minimize the effects of evaporation and seasonal bias (Breecker et al., 2009; Xu et al., 2017).

Soil waters were extracted using cryogenic vacuum extraction methods following the procedures of West et al. (2006). Water samples were equilibrated with CO_2 for 24 hr at 25 °C then analyzed using continuous-flow mass spectrometry. Hydrogen and oxygen isotope

ratios of extracted soil waters were calibrated using the water standards Desal PAT, Essential Ice, KONA DEEP, Texas DI-3, and NM-BREAK. Soil samples have an analytical error of ±0.07‰, which is less than the analytical error of the mass spectrometer (±2‰) so the mass spectrometer uncertainty of the soil waters was used. Soil samples were extracted and analyzed for hydrogen and oxygen isotope ratios by collaborator Dr. Daniel Breecker and undergraduate students at the University of Texas-Austin.

Biweekly precipitation samples for this study were collected at precipitation stations for one to two years. Stations were set up using a funnel system consisting of two nested containers, where one container provided protection from debris contaminants and the other was used for rainfall collection. The funnel directed precipitation into the inner container, which was filled with a small layer of mineral oil to prevent surface evaporation (after Fiorella et al., 2015). Waters were collected in plastic vials with limited headspace to prevent isotopic exchange with air. Precipitation samples were collected by Dr. Christopher Poulsen and Phoebe Aaron and analyzed in the Stable Water Isotope Lab at the University of Michigan Ann Harbor. Precipitation samples were analyzed for hydrogen and oxygen isotope ratios using a Picarro L2120-i Cavity Ring-Down Spectrometer (CRDS). An analytical uncertainty (±2‰) of the CRDS is used for all precipitation samples because the samples have a smaller analytical uncertainty than the instrument.

RESULTS

All results for volcanic glass, soil water, and precipitation (this study and IAEA) are listed in Tables 2.1 and 2.2. Figure 2.3 shows spatial variations in δD values for all modern data types (volcanic glass, soil water, and precipitation) and Figure 2.4 shows $\delta^{18}O$ and δD values for soil water (δD_{soil}, $\delta^{18}O_{soil}$) and precipitation (δD_{precip}, $\delta^{18}O_{precip}$). Hydrogen isotope ratios (δD_{glass}) of hydrated volcanic glass range from -2.8‰ to -196.8 ± 4.0‰ (n = 38) from the Pacific coast across the Western Cordillera. Across the Peruvian Central Andes from the Pacific coast to the Eastern Cordillera, $\delta^{18}O_{soil}$ values range from -2.1‰ to -23.9‰ ± 2.0‰ (δD: -18.2‰ to -185.8‰ ± 2.0‰) (n = 23). $\delta^{18}O_{precip}$ values range from -4.4‰ to -18.84‰ ± 2.0‰ (δD: -29.7‰ to -133.4‰ ± 2.0‰) (n = 5) and -15.2‰ to -23.5‰ (δD: -108.3‰ to -172.5‰ ± 2.0‰) for IAEA precipitation (n = 12) from the Coastal Cordillera to the Eastern

Cordillera (Figs. 2.3 and 2.4). Soil water values yield a Local Meteoric Water Line (LMWL) with a similar slope to the Global Meteoric Water Line (GWML = 8* $\delta^{18}O$ + 10) but differ in y-intercept value ($\delta D = 7.78*\delta^{18}O - 0.506$; $r^2 = 0.975$). The LMWL for weighted mean values of both collected precipitation (2016/2017) and IAEA precipitation (2001/2002) is close to the GMWL ($\delta D = 7.83*\delta^{18}O + 9.68$; $r^2 = 0.985$) (Fig. 2.4).

The spatial distribution of isotopic values for all datasets defines three distinct clusters of values between the Pacific coast and the Amazon Basin (Fig. 2.3). This includes high δD values near the Pacific coast, high δD values in the Amazon Basin, and depleted values in the Altiplano and moving up the windward sides of both the Western and Eastern Cordillera. Between the Pacific coast and 120 km inland, δD values range from -2.8‰ to -55.4‰ ± 4.0‰ with a mean of -29.1‰ (Fig. 2.3). Modern sample elevations range across this region from 97 m at the coast to 3,035 m 120 km inland (Fig. 2.3). Between 114 km to 400 km inland of the Pacific, from the peaks of the Western Cordillera to the peaks of the Eastern Cordillera, samples collected between 2,697 m and 4,757 m elevation range in δD_{glass} value from -97.5‰ to -196.8‰ ± 3.5‰. On the eastern slope of the Eastern Cordillera nearest the Amazon Basin, δD_{glass} values range from -44.3‰ to -63.6‰ ± 2.0‰. These values are correlated with lower elevations of ~750 m to the east of the Eastern Cordillera (Fig 2.3).

DISSCUSSION

Recent–modern δD values of volcanic glass, soil, and precipitation collected across the Peruvian Central Andes show similar patterns between the Pacific coast and Amazon Basin. Near the coastline, δD values do not correlate with elevation. Shifted δD_{glass} values are higher (-2.8‰ to -13.2‰ ± 4.0‰) closest to the coast (0–18 km) but vary between -16.8‰ and -55.4‰ within 91 km of the coast (Fig. 2.3). We attribute this variation from of δD_{glass} values 18–91 km inland to a higher degree of evapotranspiration of surface waters or evaporation during volcanic glass hydration. The limited soil water and precipitation data in this coastal region are in agreement with mean δD_{glass} values. Precipitation collected 119 km inland has a high δD value that likely reflects vapor that propagates up deeply incised canyons on the western slope of this orogen, where this sample was collected. This interpretation is supported by precipitation data collected at a similar distance inland but outside these

canyons, which have ~70‰ lower δD values. This data along with the δD_{glass} values from the Western Cordillera imply elevation does not affect δD values when moisture comes from the Pacific until air masses are forced out of canyons.

All samples collected from the windward slopes of both the Eastern and Western Cordillera show notable changes in δD values of two distinct air masses from low elevation regions (Pacific coast and Amazon Basin). Atlantic -derived air masses migrate up the Eastern Cordillera and across the Altiplano and Pacific-derived air masses travel up the Western Cordillera via steep river canyons. Channeling of Pacific moisture in these canyons is noted by previous workers (Gay, 2005; Hesse, 2012) and enables moisture transport that would otherwise be blocked by topography of the Coastal Cordillera. Since minimal precipitation derived from the Pacific is currently recognized to reach the Altiplano (Minvielle and Garreaud, 2011), δD values east of the Western Cordillera (~200 km inland) are most likely influenced by easterly Atlantic-derived air masses. δD values increase from ca. -200‰ to ca. -145‰ ~140 km inland, suggesting easterly derived air masses mix with Pacific-derived moisture at the heads of canyons (Fig. 2.3).

δD_{precip} values of samples collected across the Altiplano are more variable than δD_{soil} values, likely reflecting the shorter-term averages and seasonal variability of precipitation data. δD_{soil} values are closer to δD_{glass} values and therefore may represent a reliable modern proxy to compare to paleo-proxies. Overall, the isotopic profile of modern glass, soil, and precipitation samples collectively reflect the shape of the topographic profile of the orogen. It is important to note, however, that these data cannot be accounted for by a simple 1-D Rayleigh distillation model. This is because air mass mixing in the region and evaporation in the Coastal Cordillera does not cause hydrogen isotope values to predictably deplete with increased elevation. In Chapter III, we compare this modern isotopic profile to paleoisotopic values to constrain the drivers of geochemical variance in ancient meteoric waters over time.

REFERENCES

Bershaw, J., Saylor, J.E., Garzione, C.N., Leier, A. and Sundell, K.E., 2016. Stable isotope variations ($\delta^{18}O$ and δD) in modern waters across the Andean Plateau. Geochimica et Cosmochimica Acta, 194, 310–324.

Cailleteau, C., Frédéric, A., Devreux, F., Gin, S., Jestin, J., Jollivet, P., and Spalla, O., 2008. Insight into silicate-glass corrosion mechanisms. Nature Materials, 7, 978–983.

Cassel, E.J., and Breecker, D.O., 2017. Long-term stability of hydrogen isotope ratios in hydrated volcanic glass. Geochimica et Cosmochimica Acta, 200, 67–86.

Cassel, E.J., Breecker, D.O., Henry, C.D., Larson, T.E., and Stockli, D.F., 2014. Profile of a paleo-orogen: High topography across the present-day Basin and Range from 40 to 23 Ma. Geology, 42, 1007–1010.

Cassel, E.J., Smith, M.E., and Jicha, B., 2018. The impact of slab rollback on Earth's surface: Uplift and extension in the hinterland of the North American Cordillera. Geophysical Research Letters, 45, 10,996–11,004.

Cerling, T., Brown, F.H., and Bowman, J.R., 1985. Low-temperature alteration of volcanic glass: Hydration, Na, K, 18O and Ar mobility. Chemical Geology: Isotope Geoscience section, 52, 281–293.

Craig, H., 1961. Standard for reporting concentrations of deuterium and oxygen-18 in natural waters. Science, 133, 1833–1834.

Dansgaard, W., 1964. Stable isotopes in precipitation. Tellus XVI, 436–468.

Davie, T., 2008. Fundamentals of hydrology, Routledge, New York, 169.

Dettinger, M.P., and Quade, J., 2015. Testing the analytical protocols and calibration of volcanic glass for the reconstruction of hydrogen isotopes in paleoprecipitation. Geological Society of America Memoirs, 212, 261–276.

Friedman, I., Gleason, J., Sheppard, R.A., and Gude, A.J., 1993a. Deuterium fractionation as water diffuses into silicic volcanic ash. Geophysical Monograph Series, 78, 321–323.

Friedman, I., Gleason, J., and Warden A., 1993b. Ancient climate from deuterium content of water in volcanic glass. Geophysical Monograph Series, 78, 309–319.

Garreaud, R.D., Vuille, M., and Clement, A., 2003. The climate of the Altiplano: Observed current conditions and mechanisms of past changes. Palaeogeography, Palaeoclimatology, Palaeoecology, 194, 5–22.

Garreaud, R., 2000. Cold air incursions over subtropical and tropical South America: Mean structure and dynamics. Monthly Weather Review, 128, 2544–2559.

Garzione, C.N., Molnar, P., Libarkin, J.C., and MacFadden, B.J., 2006. Rapid late Miocene rise of the Bolivian Altiplano: Evidence for removal of mantle lithosphere. Earth and Planetary Science Letters, 241, 543–556.

Gat, J.R. and Airey, P.L., 2006. Stable water isotopes in the atmosphere/biosphere/lithosphere interface: Scaling-up from the local to continental scale, under humid and dry conditions. Global and Planetary Change, 51, 25–33.

Gay, S.P., 2005. Blowing sand and surface winds in the Pisco to Chala Area, Southern Peru. Journal of Arid Environments, 61, 101–117.

Ghosh, P., Adkins, J., Affek, H., Balta, B., Guo, W., Schauble, E.A., Schrag, D., and Eiler, J.M., 2006. 13C-18O bonds in carbonate minerals: A new kind of paleothermometer. Geochimica et Cosmochimica Acta, 70, 1439–1456.

Giachetti, T., Gonnermann, H.M., Gardner, J.E., Shea, T., and Gouldstone, A., 2015. Discriminating secondary from magmatic water in rhyolitic matrix-glass of volcanic pyroclasts using thermogravimetric analysis. Geochimica et Cosmochimica Acta, 148, 457–476.

Gin, S., Ryan, J.V., Schreiber, D.K., Neeway, J., and Cabié, M., 2013. Contribution of atom-probe tomography to a better understanding of glass alteration mechanisms: Application to a nuclear glass specimen altered 25 years in a granitic environment. Chemical Geology, 349–350, 99–109.

Hesse, R., 2012. Spatial distribution of and topographic controls on Tillandsia fog vegetation in coastal southern Peru: Remote sensing and modelling. Journal of Arid Environments, 78, 33–40.

Jackson, L.J., Horton, B.K., Beate, B.O., Bright, J., and Breecker, D.O., 2019. Testing stable isotope paleoaltimetry with Quaternary volcanic glasses from the Ecuadorian Andes. Geology, 47 (5), 411–414.

Kar, N., Garzione, C.N., Jaramillo C., Shanahan, T., Carlotto, V., Pullen, A., Moreno, F., Anderson, V., Moreno, E., and Eiler, J., 2016. Rapid regional surface uplift of the northern Altiplano plateau revealed by multiproxy paleoclimate reconstruction. Earth and Planetary Science Letters, 447, 33–47.

Merlivat, L., and Nief, G., 1967. Fractionnement isotopique lors des changements d'état solide-vapeur et liquide-vapeur de l'eau Á des températures inférieures Á 0°C. Tellus 19 (1), 122–127.

Minvielle, M., and Garreaud, R., 2011. Projecting rainfall changes over the South American Altiplano. Journal of Climate, 24, 4577–4583.

Moore, G., 2008. Interpreting H2O and CO2 contents in melt inclusions: Constraints from solubility experiments and modeling. Reviews in Minerology and Geochemistry, 69, 333–362.

Noone, D., 2012. Pairing measurements of the water vapor isotope ratio with humidity to deduce atmospheric moistening and dehydration in the tropical midtroposphere, Journal of Climate, 25, 4476–4494.

O'Neil, J.R.., 1986. Theoretical and experimental aspects of isotopic fractionation. Reviews in Mineralogy, 16, 1–40.

Parruzot B., Jollivet P., Re´biscoul D. and Gin S., 2015. Long-term alteration of basaltic glass: Mechanisms and rates. Geochimica et Cosmochimica Acta, 154, 28–48.

Peng, T.R., Liu, K.K., Wang, C.H., and Chuang, K.H., 2011. A water isotope approach to assessing moisture recycling in the island-based precipitation of Taiwan: A case study in the western Pacific, Water Resources Research, 47, W08507.

Picard, D., Sempere, T., and Plantard, O., 2008. Direction and timing of uplift propagation in the Peruvian Andes deduced from molecular phylogenetics of highland biotaxa. Earth and Planetary Science Letters, 271, 326–336.

Pingel, H., Mulch, A., Alonso, R.N., Cottle, J., Hynek, S.A., Poletti, J., Rohrmann, A., Schmitt, A.K., Stockli, D.F., and Strecker, M.R., 2016. Surface uplift and convective rainfall along the southern Central Andes (Angastaco Basin, NW Argentina). Earth and Planetary Science Letters, 440, 33–42.

Saylor, J.E., and Horton, B.K., 2014. Nonuniform surface uplift of the Andean plateau revealed by deuterium isotopes in Miocene volcanic glass from southern Peru. Earth and Planetary Science Letters, 387, 120–131.

Seligman, A.N., Bindeman, I.N., Watkins, J.M., and Ross, A.M., 2016. Water in volcanic glass: From volcanic degassing to secondary hydration. Geochimica et Cosmochimica Acta, 191, 216–238.

Sarna-Wojcicki, A.M., Shipley, S., Waitt, R.B., Dzurisin, D., and Wood, S.H., 1981. Areal distribution, thickness, mass, volume, and grain size of air-fall ash from the six major eruptions of 1980. In: Lipman, P.W., and Mullineaux, D.R., eds, The 1980 eruptions of Mount St. Helens, Washington. US Geological Survey professional paper, 1250, 577–600.

Stewart, M.K., 1975. Stable isotope fractionation due to evaporation and isotopic exchange of falling water drops: Applications to atmospheric processes and evaporation of lakes. Journal of Geophysical Research, 80, 1133–1146.

Sulca, J., Vuille, M., Silva, Y., and Takahashi, K., 2016. Teleconnections between the Peruvian Central Andes and northeast Brazil during extreme rainfall events in austral summer. Journal of Hydrometeorology, 17, 499–515.

Tian, L., Yao, T., MacClune, K., White, J.W.C., Schilla, A., Vaughn, B., Vachon, R., and Ichiyanagi, K., 2007. Stable isotopic variations in west China: A consideration of moisture sources. Journal of Geophysical Research, 112, 10112.

Valle, N., Verney-Carron, A., Sterpenich, J., Libourel, G., Deloule, E., and Jollivet, P., 2010. Elemental and isotopic (^{29}Si and ^{18}O) tracing of glass alteration mechanisms. Geochimica et Cosmochimica Acta, 74, 3412–3431.

Vuille, M., 1999. Atmospheric circulation over the Bolivian Altiplano during dry and wet periods and extreme phases of the Southern Oscillation. International Journal of Climatology, 19, 1579–1600.

Yamada, H. and Uyeda, H., 2006. Transition of the rainfall characteristics related to the moistening of the land surface over the central Tibetan Plateau during the summer of 1998. Monthly Weather Review, 134, 3230–3247.

Yoshimura, K., Oki, T., Ohte, N., and Kanae, S., 2003. A quantitative analysis of short-term 18O variability with a Rayleigh-type isotope circulation model. Journal of Geophysical Research, 108, 4647.

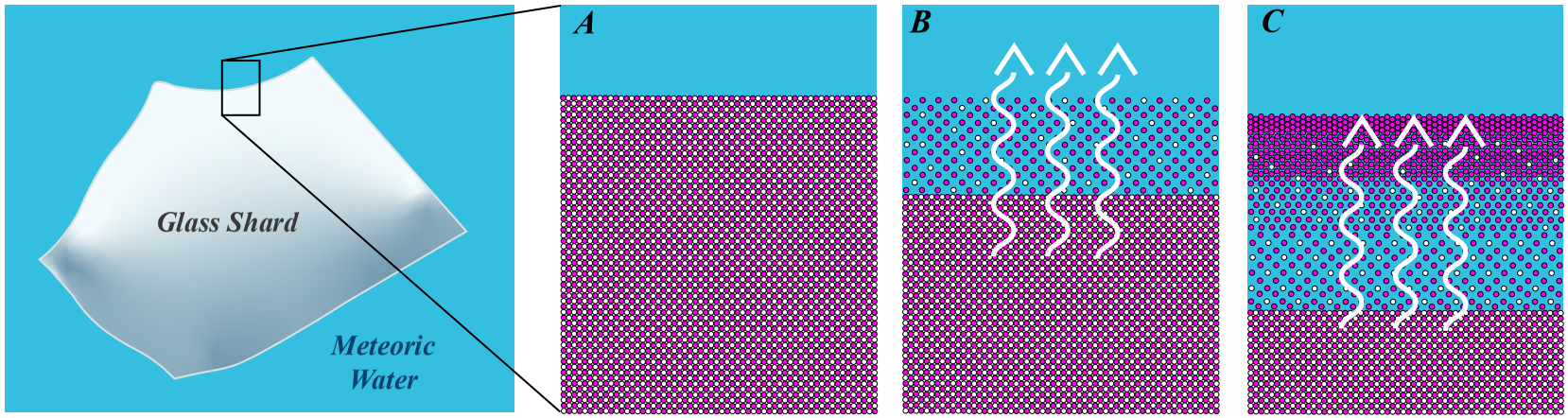

Figure 2.1. Schematic of volcanic glass hydration modified from Casey (2008). A) Pre-hydration phase of volcanic glass (glass structure: silicate structure-pink dots, soluble cations-white dots); B) hydration and exchange of soluble ions; C) formation of nanoporous silicate layer and trapping of meteoric water.

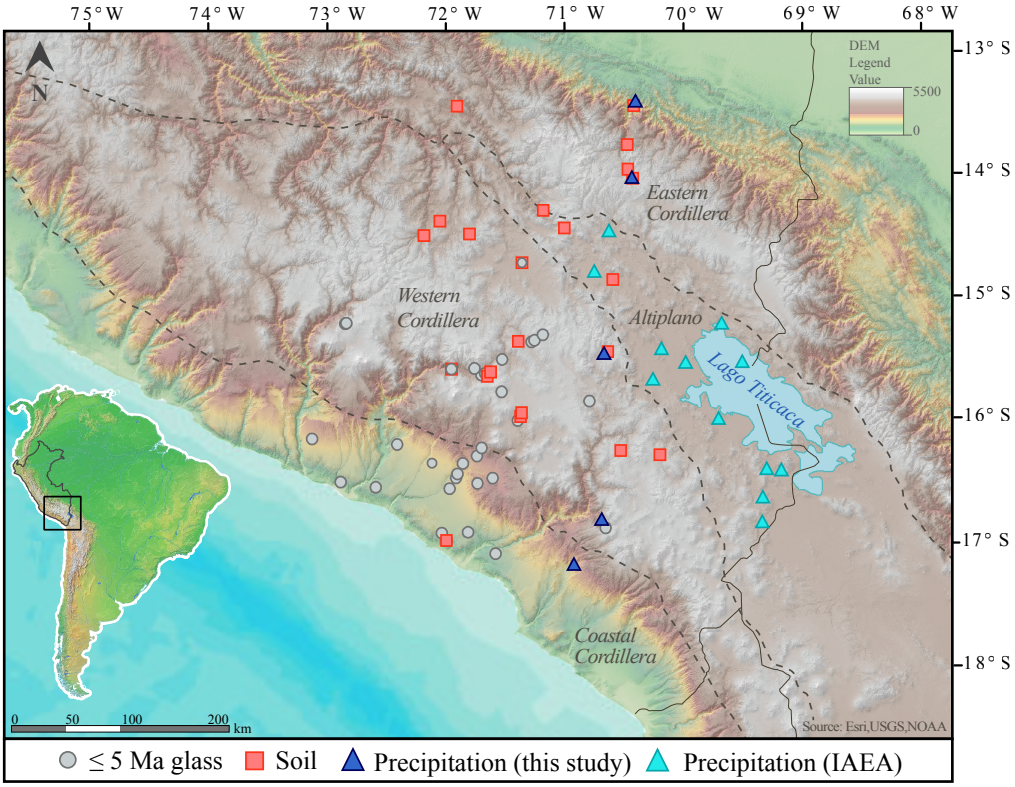

Figure 2.2. DEM of southern Peru displaying sample locations. Locations of analyzed ≤ 5 Ma hydrated volcanic glass samples denoted with grey circles and analyzed soil waters with pink squares. Triangles represent precipitation samples. Dark blue triangles are analyzed precipitation from this study and light blue are precipitation samples from IAEA/WMO (2015). Global Network of Isotopes in Precipitation. The GNIP Database.

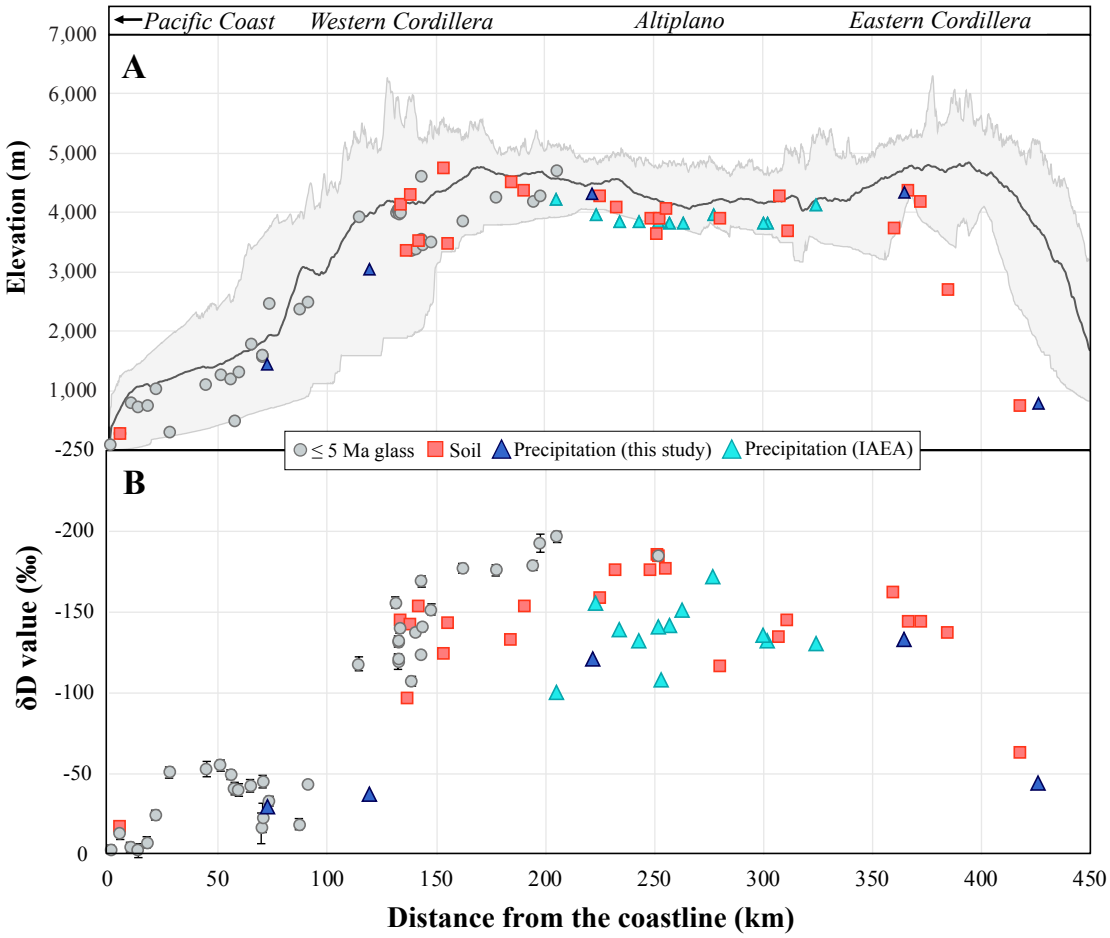

Figure 2.3. A) The distance of the sample location from the Pacific Coast plotted against sample elevations. Plotted with modern swath profile of southern Peru for location reference. Shape and color-coded for different sample types. B) The distance of the sample location from the Pacific Coast plotted against δD values of each sample. Shape and color-coded for different sample types.

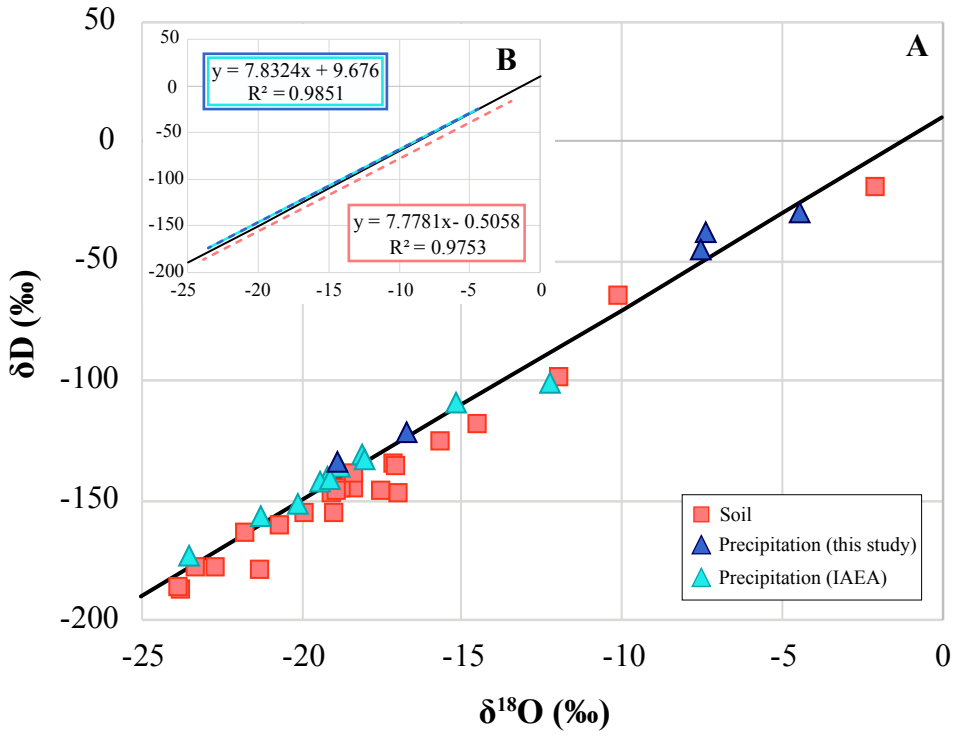

Figure 2.4. A) $\delta^{18}O$ versus δD values, color-coded for sample type. Black line represents the Global Meteoric Water Line (GMWL). B) Local meteoric water lines (LMWL) for soil and precipitation (combined this study and IAEA) plotted for sample points from (A). Color-coded by for sample type and black line represents (GMWL).

TABLE 2.1 MODERN SOIL AND PRECIPITATION SAMPLES

Sample name	Average δD (‰) VSMOW	Average $\delta^{18}O$ (‰) VSMOW	d-excess	±2σ analytical uncertainty (‰)	Distance from Pacific Coast (km)	Sample elevation (m)	Latitude	Longitude
Soil (55-80 cm depth)								
PE17-046 MLL	-18.2	-2.1	-1.5	2.00	4.63	271	-16.981	-72.016
PE18-394 SUM	-145.5	-17.0	-9.3	2.00	133.3	4138	-15.991	-71.387
PE18-315 CHV	-97.5	-12.0	-1.8	2.00	136.34	3370	-15.613	-71.972
PE18-393 CHV	-143.2	-18.4	3.7	2.00	137.79	4312	-15.962	-71.376
PE18-314 CHV	-154.1	-19.0	-2.3	2.00	141.85	3527	-15.670	-71.668
PE17-090 ICH	-124.5	-15.6	0.7	2.00	152.94	4757	-16.263	-70.535
PE17-031 CHV	-144.0	-18.7	6.0	2.00	155.3	3477	-15.636	-71.640
PE16-042 PUN	-132.9	-17.1	4.2	2.00	184.24	4509	-16.296	-70.200
PE17-036 CHV	-153.7	-19.9	5.5	2.00	190.23	4381	-15.389	-71.407
PE18-335 PAR	-159.3	-20.7	6.1	2.00	224.81	4289	-15.473	-70.645
PE18-350 TOM	-176.5	-23.3	9.8	2.00	232.28	4101	-14.539	-72.208
PE18-317 ESP	-176.7	-22.7	5.0	2.00	248.08	3909	-14.758	-71.373
PE18-351 TOM	-185.8	-23.8	4.5	2.00	251.12	3647	-14.423	-72.071
PE18-318 ESP	-184.7	-23.9	6.2	2.00	251.89	3913	-14.758	-71.373
PE18-344 VEL	-177.4	-21.3	-6.8	2.00	255.21	4069	-14.526	-71.819
PE16-037 AYV	-116.7	-14.5	-0.5	2.00	279.99	3898	-14.894	-70.601
PE16-040 SCA	-134.6	-17.1	2.0	2.00	307	4278	-14.478	-71.013
PE16-039 SCA	-145.7	-19.1	7.1	2.00	311.03	3682	-14.335	-71.193
PE16-038 CUZ	-162.3	-21.8	12.1	2.00	359.73	3739	-13.495	-71.927
PE18-332 MAC	-144.6	-17.5	-4.3	2.00	366.5	4374	-14.078	-70.433
PE18-309 MACU	-144.6	-18.9	6.5	2.00	372.05	4192	-14.005	-70.473
PE18-312 OLL	-137.2	-18.4	9.6	2.00	384.64	2697	-13.805	-70.477
PE18-310 SGB	-63.6	-10.1	17.4	2.00	417.51	743	-13.492	-70.422
Precipitation (IAEA)								
UNOCOLLO	-151.2	-20.1	9.5		263	3825	-15.446	-70.188

YANARICO	-139.2	-19.2	14.1		234	3836	-15.692	-70.258
CHICHILLAPI	-100.7	-12.2	-3.2		205	4210	-16.830	-69.330
PIATA	-132.5	-18.0	11.3		302	3810	-15.242	-69.675
PAYLLA CENTRO	-172.5	-23.5	15.6		277	3970	-14.825	-70.758
NUNOA	-130.8	-18.0	13.6		324	4135	-14.500	-70.633
HUACULLANI	-156.2	-21.3	14.0		223	3960	-16.633	-69.325
CARITAMAYA	-141.5	-19.4	13.5		257	3825	-16.006	-69.700
HUAPACA SANTIAGO	-132.6	-18.0	11.1		243	3850	-16.406	-69.292
PARCO	-108.3	-15.2	13.1		253	3850	-16.417	-69.167
ISLA SOTO	-136.0	-18.8	14.1		300	3815	-15.550	-69.500
LLACHAHUI	-140.8	-19.1	11.9		252	3840	-15.556	-69.982
Precipitation (this study)								
MACUSANI	-133.4	-18.8	17.3	2.00	364.58	4351	-14.070	-70.439
CARUMAS	-37.7	-7.4	21.3	2.00	119.29	3035	-16.812	-70.696
SAN GABAN	-44.3	-7.5	15.5	2.00	426.2	790	-13.452	-70.409
MOQUEGUA	-29.7	-4.4	5.8	2.00	72.3	1437	-17.169	-70.932
PAMPAHUTA	-121.2	-16.7	12.3	2.00	221.55	4313	-15.485	-70.676

TABLE 2.2 MODERN (≤ 5 Ma) GLASS SAMPLES

Sample name	Average δD (‰) VSMOW	Shifted δD (‰) VSMOW	2σ uncertainty (‰)	Average water content	Number of aliquots	Latitude	Longitude	Sample Elevation (m)	Distance (km)	Best age (Ma)	Error (Ma)	Reference for age data
PE004ICH-AC	-154.4	-140.7	2.28	3.1	3	-15.65	-71.69	3468	143.5	0.90	0.20	Klinck et al. (1986)
PE009MAD-AC	-137.7	-123.7	1.44	3.5	3	-15.61	-71.78	3544	142.8	0.80	0.40	Klinck et al. (1986)
PE014SCC-AC	-151.0	-137.3	1.44	4.1	3	-15.66	-71.72	3389	140.4	0.90	0.20	Klinck et al. (1986)
PE042VIC-AC	-68.3	-53.2	2.28	3.4	2	-16.57	-71.99	1110	44.3	1.64	0.07	Paquereau et al. (2008)
PE050YUR-AC	-59.2	-43.9	1.44	4.5	3	-16.24	-71.72	2497	90.9	1.77	0.15	Paquereau et al. (2008)
PE16-007COT	-146.1	-132.2	3.00	3.8	3	-15.25	-72.88	4073	132.7	2.04	0.14	Thouret et al. (2007)
PE16-009COT	-145.7	-131.9	3.00	2.7	2	-15.25	-72.88	4047	132.6	2.04	0.14	Thouret et al. (2007)
PE16-010COT	-133.6	-119.5	3.00	4.6	4	-15.25	-72.87	4043	132.6	2.04	0.14	Thouret et al. (2007)
PE16-011COT	-153.8	-140.1	3.00	2.5	3	-15.24	-72.87	4003	133.2	2.04	0.14	Thouret et al. (2007)
PE16-013COT	-135.7	-121.7	3.00	2.7	3	-15.25	-72.86	3970	132.7	2.04	0.14	Thouret et al. (2007)
PE17-020LUC	-189.3	-176.1	3.29	3.8	3	-15.87	-70.80	4253	177.3	1.90	0.40	Klinck et al. (1986)
PE17-029LAJ	-64.9	-49.7	3.29	2.1	3	-16.48	-71.93	1207	55.5	4.77	0.20	Paquereau et al. (2008)
PE17-030CHV	-182.6	-169.3	3.29	3.2	3	-15.79	-71.55	4603	143.1	2.20	0.15	Thouret et al. (2007)
PE17-032CHV	-165.2	-151.7	3.29	5.3	3	-15.64	-71.64	3513	147.5	0.23	0.05	Kaneoka & Guevara (1984)
PE17-034CHV B	-190.4	-177.2	3.29	3.3	3	-15.53	-71.54	3860	161.8	0.40	0.10	Olade (1980)
PE17-042SUM	-169.6	-156.1	3.20	3.7	6	-16.02	-71.41	3991	131.3	4.97	0.03	Paquereau et al. (2008)
PE17-043VIC	-38.8	-23.2	3.20	2.6	6	-16.37	-71.88	1570	70.3	4.95	0.03	Schildgen et al. (2009)
PE17-044VIC	-32.5	-16.8	3.20	2.8	5	-16.37	-71.88	1594	69.9	4.95	0.03	Schildgen et al. (2009)
PE17-045VIC	-60.4	-45.2	3.29	1.8	4	-16.37	-71.88	1600	70.3	4.95	0.03	Schildgen et al. (2012)
PE17-047MLL	-28.9	-13.2	3.20	2.6	6	-16.98	-72.02	286	4.8	4.90	0.30	Quang et al. (2005)
PE17-049YUR	-34.7	-19.1	3.29	2.5	3	-16.31	-71.76	2366	87.2	1.77	0.15	Paquereau et al. (2008)
PE17-050MLL	-20.8	-5.0	3.29	3.0	3	-16.92	-72.06	803	9.7	4.90	0.30	Quang et al. (2005)
PE17-055TOR	-132.2	-118.2	4.09	3.0	7	-16.88	-70.66	3933	114.4	0.50	0.10	Martinez & Cervantes (2003)
PE17-101AQP	-48.6	-33.2	3.29	1.7	6	-16.48	-71.62	2459	73.4	4.83	0.03	Paquereau et al. (2008)
PE18-316CHV A	-121.6	-107.4	2.80	3.2	3	-15.61	-71.97	3370	138.5	0.80	0.40	Gerbe & Thouret (2003)
PE18-318ESP A	-198.1	-185.2	2.80	4.1	3	-14.76	-71.37	3913	251.9	4.40	0.10	Noble et al. (2002a)

PE18-356CON	-192.0	-178.9	2.80	5.3	3	-15.39	-71.29	4175	194.4	4.92	0.13	Sundell et al. (2019)
PE18-357CON	-209.6	-196.8	2.80	3.5	2	-15.34	-71.20	4693	205.1	4.92	0.13	Sundell et al. (2019)
PE18-358CON	-205.9	-193.0	2.80	3.9	2	-15.38	-71.27	4290	197.5	4.92	0.13	Sundell et al. (2019)
PE18-361PIC	-66.5	-51.4	3.45	4.0	6	-16.17	-73.16	306	27.6	2.01	0.03	Schildgen et al. (2009)
PE18-362ONC	-19.4	-3.5	2.80	4.4	2	-16.51	-72.92	97	0.6	2.01	0.03	Schildgen et al. (2009)
PE18-363MAJ	-18.7	-2.8	3.45	2.3	3	-16.56	-72.62	735	13.2	4.77	0.20	Paquereau et al. (2008)
PE18-367COR	-56.3	-41.0	4.09	2.9	6	-16.22	-72.43	489	57.1	1.64	0.07	Paquereau et al. (2008)
PE18-374MAJ	-70.5	-55.4	3.45	2.4	4	-16.36	-72.14	1262	50.9	1.64	0.07	Paquereau et al. (2008)
PE18-381VIC	-55.3	-40.0	4.09	2.4	6	-16.45	-71.92	1305	59.3	2.76	0.10	Vatin -Perignon et al. (1996)
PE18-390MOC	-23.5	-7.7	3.45	2.6	5	-17.08	-71.60	751	17.2	5.00	0.30	Quang et al. (2005)
PE18-391JOY	-40.4	-24.9	2.80	2.5	3	-16.92	-71.83	1042	21.0	4.90	0.30	Quang et al. (2005)
PE18-392AQP	-58.0	-42.7	4.09	1.4	3	-16.53	-71.75	1782	64.8	3.05	3.40	Vatin -Perignon et al. (1996)
PE025CHU-AC*	-44.4			0.1	2	-15.88	-72.65	2791	80.6			
PE025CHU-AC*	-68.5			0.1	2	-15.88	-72.65	2791	80.6			
PE037COTA-AC*	-57.3			0.1	3	-15.65	-72.81	4151	95.6			
PE037COTA-AC*	-73.2			0.1	2	-15.65	-72.81	4151	95.6			
PE16-003MAJ A*	-73.3			0.2	2	-16.21	-72.41	616	58.5			

* Samples not considered from too low of water content to get accurate hydrogen value

CHAPTER III

Miocene Uplift History of the Peruvian Central Andes

ABSTRACT

Characterizing the timing and style of orogen-wide surface uplift in the Peruvian Central Andes can inform us about how climate changes with large-scale orogenic events. Paleoelevation estimates can provide spatial and temporal constraints key to understanding the potential geodynamic drivers contributing to ancient surface uplift. Previous studies in the Peruvian Central Andes, however, lack orogen-wide isotopic constraints or calibration with modern isotopic values. As a result, existing models for the uplift history of this region show wide disagreement. Here we reconstruct the timing of surface uplift in the Peruvian Central Andes from 26 to 5 million years ago using hydrogen isotope ratios measured from hydrated volcanic glasses as a proxy for paleo-meteoric water. Samples span the width of the orogen from the Pacific coast to the Eastern Cordillera and are calibrated to modern hydrogen isotope compositions that can account for secular changes in air masses before they move across the orogen. Our results indicate surface uplift was non-uniform and started in the Eastern Cordillera, where similar to modern elevations were reached by at least 17 Ma. The Western Cordillera then underwent uplift between 16 and 11 Ma, indicating near modern elevations were attained by the late Miocene.

INTRODUCTION

The timing and style of orogenic surface uplift directly relates to the tectonic mechanisms that produce large mountains belts. Since large mountain belts act as orographic barriers that affect local and global climate, characterization of the timing/style of uplift is also critical for understanding climate records. In the Central Andean orocline, southern Peru encompasses the northern extent of the Altiplano-Puna plateau, one of the tallest plateaus in the world (with mean elevations of ~4 km) and the archetypal example of oceanic–continental

subduction processes (Allmendinger et al., 1997). The evolution of Central Andean surface uplift has remained enigmatic despite intensive study (e.g., Allmendinger et al., 1997; Saylor and Horton, 2014; Thouret et al., 2017; Garzione et al., 2017). Past elevation estimates in this area are based on a variety of methods, including air-mass-based modeling, climate modeling, and empirical lapse rate linear regressions (Rowley and Garzione, 2007; Poulsen et al., 2010; Insel et al., 2012; Sundell et al, 2019). Current uplift models for the Central Andean orocline include gradual (Ehlers and Poulsen, 2009), rapid (Ghosh et al., 2006; Garzione et al., 2008; Kar et al., 2016), and non-uniform (Saylor and Horton, 2014; Sundell et al., 2019) surface uplift (Fig 3.1 and Fig 3.2). In southern Peru, which comprises the northern extent of the orocline, paleoaltimetric constraints from river incision, genetic diversity, and stable isotope data together suggest uplift was non-uniform across the orogen, but substantial uplift may have occurred anywhere from 25–10 Ma in the Eastern Cordillera and as late as 6 Ma in the Western Cordillera (Schildgen et al., 2007; Thouret et al., 2007, 2017; Picard et al., 2008; Ehlers and Poulsen, 2009; Lease and Ehlers, 2013; Saylor and Horton, 2014; Kar et al., 2016; Sundell et al., 2019)

To determine paleoelevations in the Peruvian Central Andes, paleoisotopic studies commonly 1) compare the magnitude of δD or $\delta^{18}O$ change between low and high elevation samples, 2) use a one dimensional model that applies a modern lapse rate and takes into account the relative humidity and temperature of the starting airmass to model elevations across a transect (Rowley and Garzione, 2007), or 3) use an isotope-tracking general circulation model (GCM) with various modeled elevations of the Andes to estimate lapse rates and then apply them to empirical observed stable isotope values to determine past elevations (Insel et al., 2012). Existing paleoelevation estimates, however, do not compare isotopic values with a measured past low elevation datum. These estimates therefore do not account for δD changes in initial air mass rainout through time and lead to erroneous paleoelevation estimates. Paleoelevation reconstructions must also account for moisture recycling or mixing of air masses in the study region, both of which affect precipitation δD values in the modern Peruvian Andes (Minvielle and Garreaud, 2011). Discrimination between existing uplift models requires a new approach that is grounded to the modern isotopic record, evaluates moisture recycling/evaporation of an air mass, and uses a low

elevation datum for past proxies. Here we compare a modern isotopic profile of the orogen to past profiles with known low elevation constraints for several critical time periods.

METHODS

Hydrogen isotope paleoaltimetry using volcanic glass can provide quantitative paleoelevation estimates across a large area and over multiple time slices (Cassel et al., 2014, 2018). In the Peruvian Central Andes, ignimbrites and ash-fall tuffs of Miocene–Pleistocene age are exposed across a 415 km long and 360 km wide transect, from the Pacific coast to the flank of the Amazon rainforest (Thouret et al., 2007), and provide an ideal proxy material for paleoelevation reconstructions. Stable isotope paleoaltimetry is based on the sustained depletion of ^{2}H and ^{18}O relative to ^{1}H and ^{16}O in an air mass with increasing elevation (Dansgaard, 1964; O'Neil, 1986). As an air mass cools, water condenses with a slightly higher $^{2}H/^{1}H$ and $^{18}O/^{16}O$ ratio than the original vapor, resulting in continued deuterium and oxygen-18 depletion of the vapor source (i.e., as elevation increases δD and $\delta^{18}O$ values decrease) (Dansgaard, 1964; Merlivat and Nief, 1967). This rainout process is controlled by air mass temperature, which is strongly influenced by elevation, but can also be affected by latitudinal variation, precipitation amount, and continentality (Dansgaard 1964; Sharp, 2007). Prior studies demonstrate that elevation change typically affect $\delta^{18}O$ values by -2‰ per 1 km elevation gain (Poage and Chamberlin, 2001), latitudinal variation changes $\delta^{18}O$ values -0.5‰ per degree latitude/111 km (Meehan et al., 2004), precipitation amount effect can change $\delta^{18}O$ values by ca. -2‰ per 200 mm of precipitation (Kendall and Coplen, 2001), and the continentality effect can change $\delta^{18}O$ values -0.75‰ per 1000 km (Salati et al., 1979).

Meteoric waters in the vadose zone derived from air mass depletion with increasing elevation can hydrate volcanic glass in volcanic rocks situated near the surface. Once in contact with surface waters, volcanic glass hydrates with up to ~10 wt.% ambient water through diffusion and exchange of soluble ions within the glass structure (Cerling et al., 1985; Cailleteau et al., 2008; Valle et al., 2010; Vienna et al., 2013). Subsequent silicate bonding near the outside of the glass prevents further dissolution of soluble components and exchange with ambient meteoric waters within the hydration period (< 10,000 years) (Gin et al., 2011). This process ultimately traps the isotopic signature of hydration water in the glass near the

time of deposition (Cailleteau et al., 2008; Gin et al., 2011; Parruzot et al., 2015; Giachetti et al., 2015). Felsic glasses have little water present in their structure upon eruption (0.1–0.5 wt. %) (Giachetti et al., 2015) and hydrate faster than mafic volcanic glass (Seligman et al., 2016). The cumulative low original water content, hydration rate, and storage potential of felsic glass make it an ideal proxy for paleoisotopic studies.

Here we directly compare modern (≤ 5 Ma) hydrated volcanic glass δD values to δD_{glass} values of samples that range in age from 25 Ma to 5 Ma. Samples from the older age groups were collected from ignimbrite and air fall tuff over a span of modern elevations to constrain the Miocene uplift history of the Peruvian Central Andes. Since this study consists of a direct comparison of volcanic glass geochemistry, we do not apply a fractionation correction to back-calculate the composition of meteoric water during hydration. Volcanic glasses were separated using methods described in detail in Cassel and Breecker (2017) and analyzed at the University of Texas-Austin using a TC/EA coupled with a MAT 253 gas source IRMS (outlined in Chapter II, Methods).

RESULTS

Hydrogen isotope ratios (reported in per mil (‰)) of 50 hydrated glass separates (Table 3.1) were sampled from rhyolitic to andesitic ignimbrites and air-fall tuffs exposed across a 370 km southwest to northeast transect in southern Peru (Fig 3.3). δD_{glass} values are split into groups spanning several million years based on common ignimbrite depositional ages in southern Peru. The oldest (23–26 Ma) group of samples (n=6), collected near the Pacific coast in the Coastal Cordillera (38–65 km), have δD_{glass} values ranging from -21.6‰ to -72.68‰ ± 3.3‰ (Fig 3.4). Two samples in the Eastern Cordillera, with ages of either 17 or 23 Ma, have an average δD_{glass} value of -192.6‰ ± 3.8‰. Ignimbrites from these age groups are part of the transition between the Tazca arc (30–24 Ma) and Huaylillas arc (24–10 Ma), reflecting southwest-directed migration of the magmatic front during voluminous ignimbrite deposition ca. 26 to 18 Ma (Mamani, et al. 2010). From the Coastal Cordillera to the Altiplano (7–256 km), 16–19 Ma volcanic glasses, produced by the Huaylillas arc (Mamani et al., 2010), range in δD_{glass} values from -47.0‰ to -174.1‰ ± 3.1‰ (n=16) (Fig 3.4). δD_{glass} values at this time are relatively constant across the Western Cordillera and southwestern

Altiplano with a range in δD_{glass} values from -47.0‰ to -86.6‰ ± 10.0‰ (average value: -69.6‰ ± 2.9‰). 11–15 Ma glasses, deposited across a wide extent of the orogen, from the Coastal Cordillera to the Altiplano (16–250 km), yield δD_{glass} values ranging from -63.3‰ to -197.6‰ ± 3.5‰ (n=14). This range in δD_{glass} values is similar to the 16–19 Ma range in δD_{glass} values, however, in the Western Cordillera values decrease ~70‰ at 100 km inland and ~120‰ at 190 km inland between these two age groups (Fig 3.4).

The Barroso arc, which nearly aligned with the western extent of the present-day magmatic arc but extended further to the east (Trumbull et al., 2006; Mamani et al., 2010) produced volcanic material from 6–10 Ma. Volcanic rocks of this age were sampled between the Coastal Cordillera and the high peaks of the Eastern Cordillera and have δD_{glass} values from -39.1‰ to -206.7‰ ± 4.09 ‰ (n=12). δD_{glass} values from 6–10 Ma are ca. -50‰ ± 3.3‰ in the Coastal Cordillera (27–65 km) and decrease to ca. -195‰ ± 4.0‰ in the Altiplano and the Eastern Cordillera (233–373 km) (Fig 3.4).

DISCUSSION

δD_{glass} values show non-uniform surface uplift across the Peruvian Central Andes through the Miocene. δD_{glass} values from 17 or 23 Ma samples in the Eastern Cordillera overlap within error with δD_{glass} values from 7 Ma glasses in the Eastern Cordillera and modern glasses collected in the Altiplano. Contrary to previous studies in the Peruvian Andes (e.g. Lease and Ehlers, 2013; Saylor and Horton, 2014; Garzione et al., 2017; Sundell et al., 2019), our δD_{glass} values from the 17 or 23 Ma age group in the Eastern Cordillera indicate that the Eastern Cordillera was close to modern elevations by at least 17 Ma, or as early as 23 Ma. Although we do not have a paleo-low-elevation datum for the Amazon Basin, we can infer that these values in the Eastern Cordillera reflect uplift since global temperatures have generally cooled since the early Miocene (Zachos et al., 2001). In addition, cooler climatic conditions could only shift δD_{glass} values of 17 or 23 Ma samples more negative compared to the modern.

Large and regional negative shifts in δD_{glass} values for a distinct time period can correlate to a change in elevation, regional or global climate, or moisture source (Dansgard, 1964; Poulsen et al., 2010). 16–19 Ma δD_{glass} values remain unchanged progressing inland

from the Pacific coast (0–200 km), with an average δD_{glass} value of ca. -60‰. These values show continued moisture recycling further inland than present when compared to modern δD_{glass} values of the Western Cordillera (Fig 3.4). Thus, the Pacific moisture source likely extended to the present Altiplano region at this time since most δD_{glass} values in the Altiplano are ca. -165‰.

δD_{glass} values in the Western Cordillera decrease from ca. -60‰ at 16 Ma to -70‰ to -188‰ at 11 Ma, 90–200 km inland (Fig 3.4). By 11 Ma, δD_{glass} values are similar to modern δD_{glass} values across the Western Cordillera. This significant decrease in δD_{glass} values from 16 to 11 Ma, could reflect large-scale surface uplift or a change in air mass mixing. We do not relate this decrease to a significant climatic change since δD_{glass} values of initial precipitation near the Pacific coast are similar for these age groups and there are no recognized coeval climate events that could produce the large fractionation difference as moisture sources progressed inland (Zachos et al., 2001). In addition, we do not attribute latitudinal and continentality effects to this > 100‰ shift because both effects could together only account for a < 6‰ change in δD_{glass} value. We also anticipate the precipitation amount effect is minor because glasses preserve a long-term average of meteoric water chemistry (over ca. 10,000 years). The air mass mixing clearly documented here within modern δD_{glass} values at ~140 km inland on the western side of the Western Cordillera, demonstrates that air mass mixing also likely existed in the past. We therefore attribute the large-magnitude shift in δD_{glass} values from 16 to 11 Ma to surface uplift of the Western Cordillera. This uplift would have pushed the mixing zone of the Pacific and Amazon moisture sources westward to ca. 140 km from ca. 230 km inland from 16 to 11 Ma. δD_{glass} values of 11–15 and 6–10 Ma samples are similar to the ≤ 5 Ma sample values, indicating an absence of major subsequent climatic or topographic changes in the region.

CONCLUSIONS

This study is the first to compare δD_{glass} values from modern hydrated volcanic glass to ancient glass to characterize past surface uplift. Comparisons of δD_{glass} values from across the Peruvian Central Andes show a westward progression of surface uplift during the Miocene; peaks of the Eastern Cordillera were elevated by at least 17 Ma and the Western

Cordillera uplifted within 5 Myr to reach similar to modern elevations by 11 Ma (Fig. 3.5). Surface uplift in the Eastern Cordillera coincides with observed crustal thickening in the region, after broadening of the arc at ca. 30 Ma as a result of shallowing of the subducting slab (Wörner et al., 2000; Haschke et al., 2002). Constructional topography may have contributed to surface uplift by 17 Ma, when convergence rates increased (Mamani et al., 2010) and the slab began to steepen, producing an influx of hot asthenospheric material and thermal uplift (Roperch et al., 2006). For example, westward arc migration from 24–10 Ma (Mamani et al., 2010) led to continued asthenospheric input and voluminous volcanism that could have triggered thermal and/or isostatic uplift in the Western Cordillera region by 11 Ma. A shift in provenance from Eastern Cordillera-derived sediment to Western Cordillera-derived sediment in the forearc from 14–12 Ma (Alvan et al., 2015) also supports uplift of the Western Cordillera at this time.

REFERENCES

Allmendinger, R.W., Jordan, T.E., Kay, S.M., and Isacks, B.L., 1997. The evolution of the Altiplano-Puna Plateau of the central Andes. Annual Review of Earth and Planetary Sciences, 25, 139–174.

Alván, A., Von Eynatten, H., Dunkl, I., and Gerdes, A., 2015. Zircon U–Pb geochronology and heavy mineral composition of the Camaná Formation, southern Peru: Constraints on sediment provenance and uplift of the Coastal and Western Cordilleras. Journal of South American Earth Sciences, 61, 14–32.

Cailleteau C., Angeli F., Devreux F., Gin S., Jestin, J., Jollivet, P., and Spalla, O., 2008. Insight into silicate-glass corrosion mechanisms. Nature Medicine, 7, 978–983.

Cassel, E.J., and Breecker, D.O., Henry, C.D., Larson, T.E., and Stockli, D.F., 2014. Profile of a paleo-orogen: High topography across the present-day Basin and Range from 40 to 23 Ma. Geology, 42, 1007–1010.

Cassel, E.J., Smith, M.E., and Jicha, B., 2018. The impact of slab rollback on Earth's surface: Uplift and extension in the hinterland of the North American Cordillera. Geophysical Research Letters, 45, 10,996–11,004.

Cerling, T.E., Brown, F.H., and Bowman J.R., 1985. Low-temperature alteration of volcanic glass: Hydration, Na, K, 18O and Ar mobility. Chemical Geology: Isotope Geoscience section, 52, 281–293.

Dansgaard, W., 1964. Stable isotopes in precipitation. Tellus, XVI, 436–468.

Ehlers, T.A., and Poulsen, C.J., 2009. Influence of Andean uplift on climate and paleoaltimetry estimates. Earth and Planetary Science Letters, 281, 238–248.

Friedman, I., Gleason, J., Sheppard, R.A., and Gude, A.J., 1993a. Deuterium fractionation as water diffuses into silicic volcanic ash. Geophysical Monograph Series, 78, 321–323.

Friedman, I., Gleason, J., and Warden A., 1993b. Ancient climate from deuterium content of water in volcanic glass. Geophysical Monograph Series, 78, 309–319.

Garreaud, R.D., Molina, A. and Farias, M., 2010. Andean uplift, ocean cooling and Atacama hyperaridity: A climate modeling perspective. Earth and Planetary Science Letters, 292, 39–50.

Garzione, C.N., Gregory, H., Libarkin, J., Withers, S., MacFadden, B., Eiler, J., Ghosh, P., Mulch, A., 2008. The Rise of the Andes. Science, 320, 1304–7.

Garzione, C.N., McQuarrie, N., Perez, N.D., Ehlers, T.A., Beck, S.L., Kar, N., Eichelberger, N., Chapman, A.D., Ward, K.M., Ducea, M.N., Lease, R.O., Poulsen, C.J., Wagner, L.S., Saylor, J.E., Zandt, G., and Horton, B.K., 2017. Tectonic Evolution of the Central Andean Plateau and implications for the growth of plateaus. Annual Review of Earth and Planetary Sciences, 45, 529–559.

Ghosh, P., Garzione, C.N., and Eiler, J.M., 2006. Rapid uplift of the Altiplano revealed through 13C–18O bonds in paleosol carbonates. Science, 311, 511–515.

Giachetti, T., Gonnermann, H.M., Gardner, J.E., Shea, T., and Gouldstone, A., 2015. Discriminating secondary from magmatic water in rhyolitic matrix-glass of volcanic pyroclasts using thermogravimetric analysis. Geochimica et Cosmochimica Acta, 148, 457–476.

Gin, S., Guittonneau, C., Godon, N., Neff, D., Rebiscoul, D., Cabie, M., and Mostefaoui S., 2011. Nuclear glass durability: New insight into alteration layer properties. Journal of Physical Chemistry, 115, 18,696–18,706.

Haschke, M.R., Siebel, W., Günther, A., and Scheuber, E., 2002. Repeated crustal thickening and recycling during the Andean orogeny in north Chile (21º–26ºS). Journal of Geophysical Research, 107, 1–18.

Insel, N., Poulsen, C.J., Ehlers, T.A. and Sturm, C., 2012. Response of meteoric $\delta^{18}O$ to surface uplift—Implications for Cenozoic Andean Plateau growth. Earth and Planetary Science Letters, 317, 262–272.

Jeffery, M.L., Ehlers, T.A., Yanites, B.J. and Poulsen, C.J., 2013. Quantifying the role of paleoclimate and Andean Plateau uplift on river incision. Journal of Geophysical Research. Earth Surface, 118, 852–871.

Kar, N., Garzione, C.N., Jaramillo C., Shanahan, T., Carlotto, V., Pullen, A., Moreno, F., Anderson, V., Moreno, E., and Eiler, J., 2016. Rapid regional surface uplift of the northern Altiplano plateau revealed by multiproxy paleoclimate reconstruction. Earth and Planetary Science Letters, 447, 33–47.

Kendall, C., and Coplen, T.B., 2001. Distribution of oxygen-18 and deuterium in river waters across the United States. Hydrological Processes, 15, 1363–1393.

Lease, R,O., and Ehlers, T.A., 2013. Incision into the eastern Andean Plateau during Pliocene cooling. Science, 341, 774–776.

Mamani, M., Worner, G., and Sempere, T., 2009. Geochemical variations in igneous rocks of the Central Andean orocline (13ºS to 18ºS): Tracing crustal thickening and magma generation through time and space. Geological Society of America Bulletin, 122, 162–182.

Meehan, T.D., Giermakowski, J.T., and Cryan, P.M., 2004. GIS-based model of stable hydrogen isotope ratios in North American growing-season precipitation for use in animal movement studies. Isotopes in Environmental and Health Studies, 40, 291–300.

Merlivat, L., and Nief, G., 1967. Fractionnement isotopique lors des changements d'état solide-vapeur et liquide-vapeur de l'eau Á des températures inférieures Á 0°C. Tellus 19 (1), 122–127.

Minvielle, M., and Garreaud, R., 2011. Projecting rainfall changes over the South American Altiplano. Journal of Climate, 24, 4577–4583.

O'Neil, J.R.., 1986. Theoretical and experimental aspects of isotopic fractionation. Reviews in Mineralogy, 16, 1–40.

Parruzot, B., Jollivet, P., Re´biscoul, D., and Gin, S., 2015. Long-term alteration of basaltic glass: Mechanisms and rates. Geochimica et Cosmochimica Acta, 154, 28–48.

Poage, M.A., and Chamberlin, P.C., 2001. Empirical relationships between elevation and the stable isotope composition of precipitation and surface waters: Considerations for studies of paleoelevation change. American Journal of Science, 301, 1–15.

Picard, D., Sempere, T., and Plantard, O., 2008. Direction and timing of uplift propagation in the Peruvian Andes deduced from molecular phylogenetics of highland biotaxa. Earth and Planetary Science Letters, 271, 326–336.

Poulsen, C.J., Ehlers, T.A., and Insel, N., 2010. Onset of convective rainfall during gradual Late Miocene rise of the Central Andes. Science, 328, 490–493.

Rech, J.A., Currie, B.S., Shullenberger, E.D., Dunagan, S.P., Jordan, T.E., Blanco, N., Tomlinson, A.J., Rowe, H.D., and Houston, J., 2010. Evidence for the development of the Andean rain shadow from a Neogene isotopic record in the Atacama Desert, Chile. Earth and Planetary Science Letters, 292, 371–382.

Roperch, P., Sempere, T., Macedo, O., Arriagada, C., Fornari, M., Tapia, C., García, M., and Laj, C., 2006. Counterclockwise rotation of late Eocene-Oligocene fore-arc deposits in southern Peru and its significance for oroclinal bending in the central Andes. Tectonics, 25, TC3010.

Rowley, D.B., Garzione, C.N., 2007. Stable isotope-based paleoaltimetry. Annual Review of Earth and Planetary Sciences, 35, 463–508.

Salati, E., Dall'Olio, A., Matsui, E., and Gat, J.R., 1979. Recycling of water in the Amazon Basin. Water Resources Research, 15, 1250–1258.

Saylor, J.E., and Horton, B.K., 2014. Nonuniform surface uplift of the Andean plateau revealed by deuterium isotopes in Miocene volcanic glass from southern Peru. Earth and Planetary Science Letters, 387, 120–131.

Seligman, A.N., Bindeman, I.N., Watkins, J.M., and Ross, A.M., 2016. Water in volcanic glass: From volcanic degassing to secondary hydration. Geochimica et Cosmochimica Acta, 191, 216–238.

Schildgen, T.F., Hodges, K.V., Whipple, K.X., Reiners, P.W., and Pringle, M.S., 2007. Uplift of the western margin of the Andean plateau revealed from canyon incision history, southern Peru. Geology, 35, 523–526.

Sharp, Z., 2017. Principles of Stable Isotope Geochemistry, 2nd Edition.

Sundell, K.E., Saylor, J.E., Lapen, T.J., and Horton, B.K., 2019. Implications of variable late Cenozoic surface uplift across the Peruvian central Andes. Scientific Reports, 9, 4877.

Thouret, J.C., Wörner, G., Gunnell, Y., Singer, B., Zhang, X., and Souriot, T., 2007. Geochronologic and stratigraphic constraints on canyon incision and Miocene uplift of the Central Andes in Peru. Earth and Planetary Science Letters, 263, 151–166.

Thouret, J.C., Gunnell, Y., Jicha, B.R., Paquette, J.-L., and Braucher, R., 2017. Canyon incision chronology based on ignimbrite stratigraphy and cut-and-fill sediment sequences in SW Peru documents intermittent uplift of the western Central Andes. Geomorphology, 298, 1–19.

Trumbull, R.B., Wittenbrink, R., Hahne, K., Emmermann, R., Büsch, W., Gerstenberger, H., and Siebel, W., 1999. Evidence for late Miocene to recent contamination of arc andesites by crustal melts in the Chilean Andes (25º–26ºS) and its geodynamic implications. Journal of South American Earth Sciences, 12, 135–155.

Valle, N., Verney-Carron, A., Sterpenich, J., Libourel, G., Deloule, E., and Jollivet, P., 2010. Elemental and isotopic (^{29}Si and ^{18}O) tracing of glass alteration mechanisms. Geochimica et Cosmochimica Acta, 74, 3412–3431.

Vienna, J.D., Ryan, J.V., Gin, S., and Inagaki, Y., 2013. Current understanding and remaining challenges in modeling long-term degradation of borosilicate nuclear waste glasses. International Journal of Applied Glass Science, 4, 283–294.

Wörner, G., Hammerschmidt, K., Henjes-Kunst, F., Lezaun, J., and Wilke, H., 2000. Geochronology (40Ar-39Ar-, K-Ar-, and He-exposure-) ages of Cenozoic magmatic rocks from northern Chile (18º–22ºS). Implications for magmatism and tectonic evolution of the Central Andes. Revista Geológica de Chile, 27, 205–240.

Zachos, J., Pagani, M., Sloan, L., Thomas, E., and Billups, K., 2001. Trends, rhythms, and aberrations in global climate 65 Ma to present. Science, 292, 686–693.

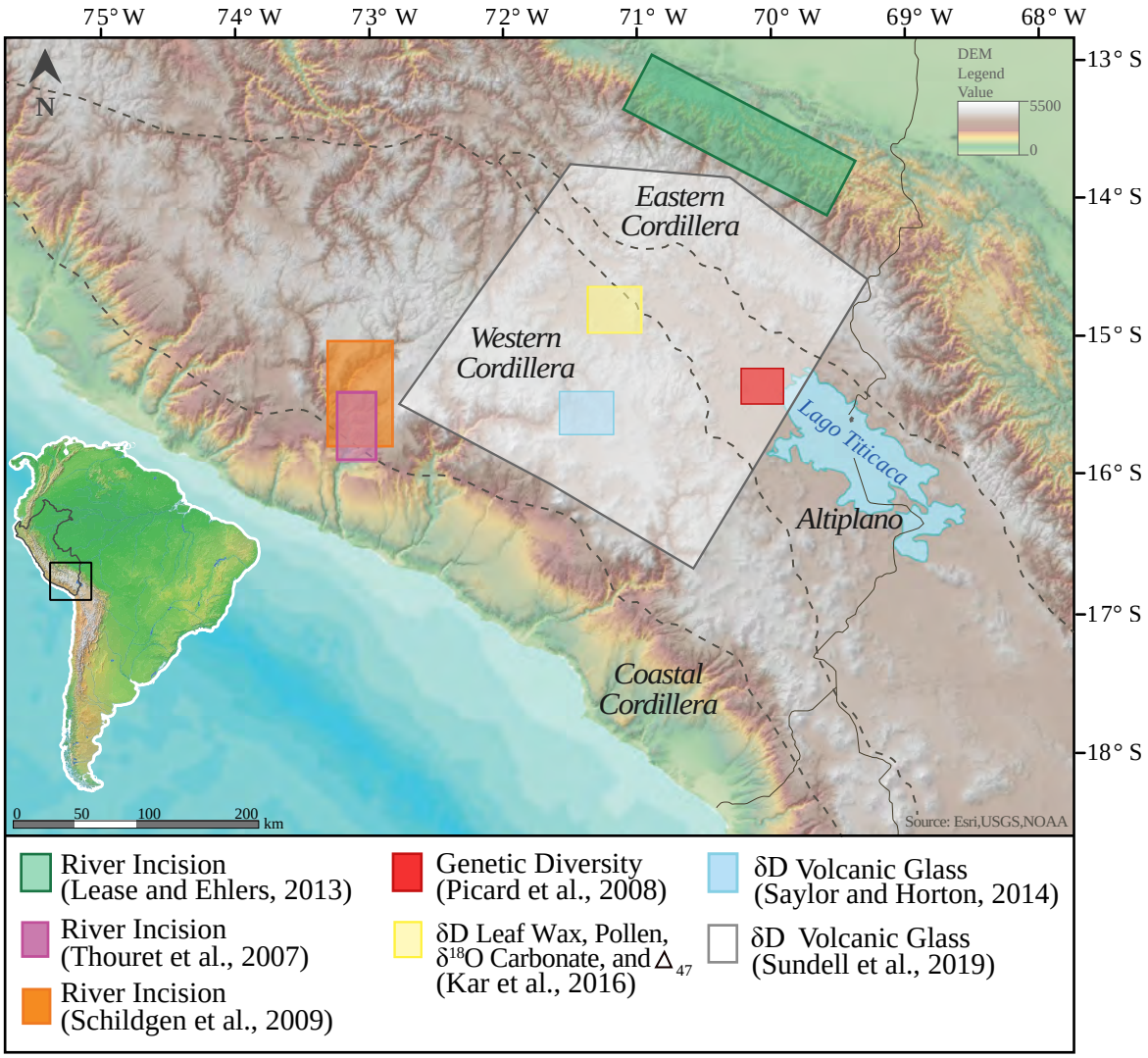

Figure 3.1. Locations of previous paleoalitmetric studies in the Peruvian Central Andes.

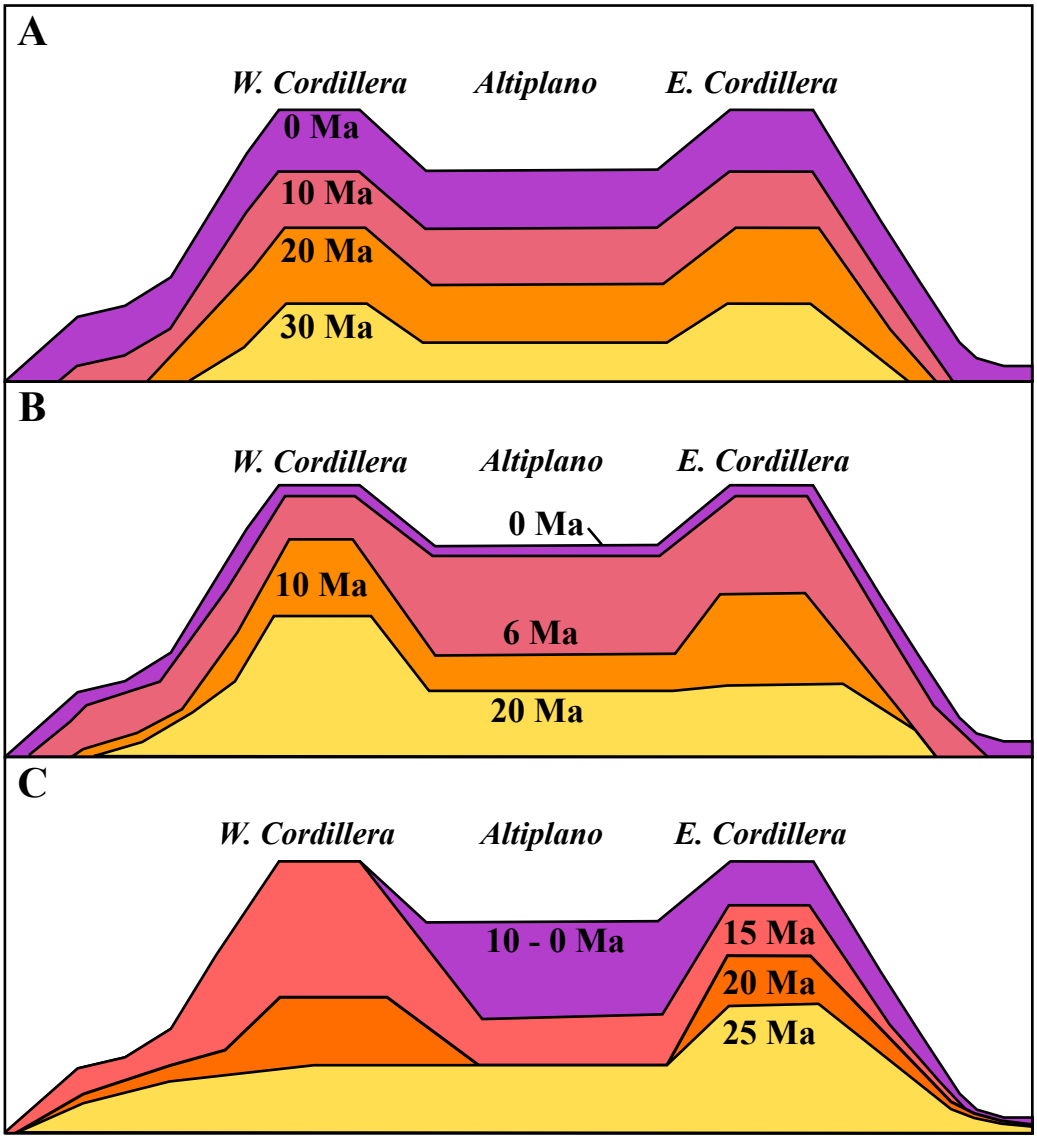

Figure 3.2. Uplift models based on previous research in southern Peru: A) Gradual surface uplift; B) Rapid surface uplift; C) Non-Uniform surface uplift.

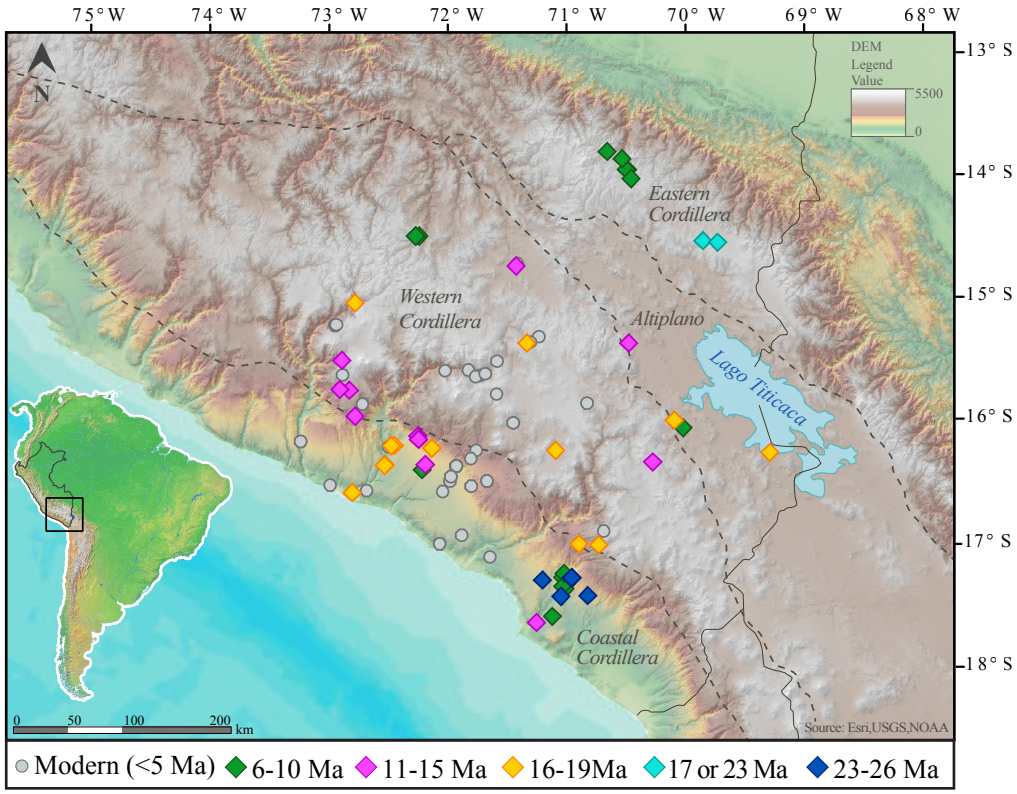

Figure 3.3. DEM of southern Peru displaying sample locations of volcanic glass. Location of modern (≤ 5 Ma) hydrated volcanic glass samples denoted with grey circles. Diamonds represent ancient glass colored by age. Grouped in ages from 6-10, 11-15, 16-19, 17 or 23, and 23-26.

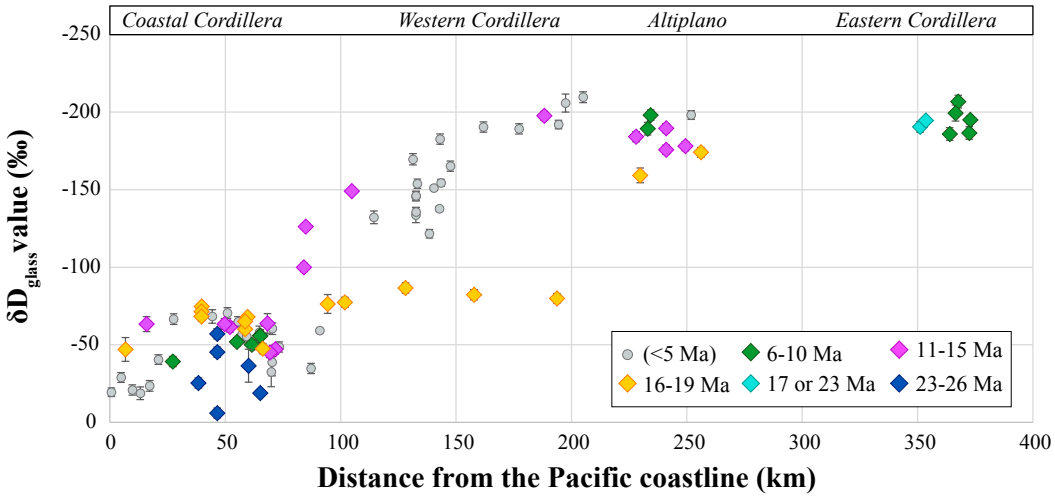

Figure 3.4. Sample location along a transect from the Pacific Coast across the Eastern Cordillera plotted against δD_{glass} values. Modern (≤ 5 Ma) δD_{glass} values denoted by grey circles. Ancient δD_{glass} values are denoted by diamonds and colored by grouped age (6-10, 11-15, 16-19, 17 or 23, and 23-26). The δD_{glass} values are grouped by age based on prominent wide-spread ignimbrite events.

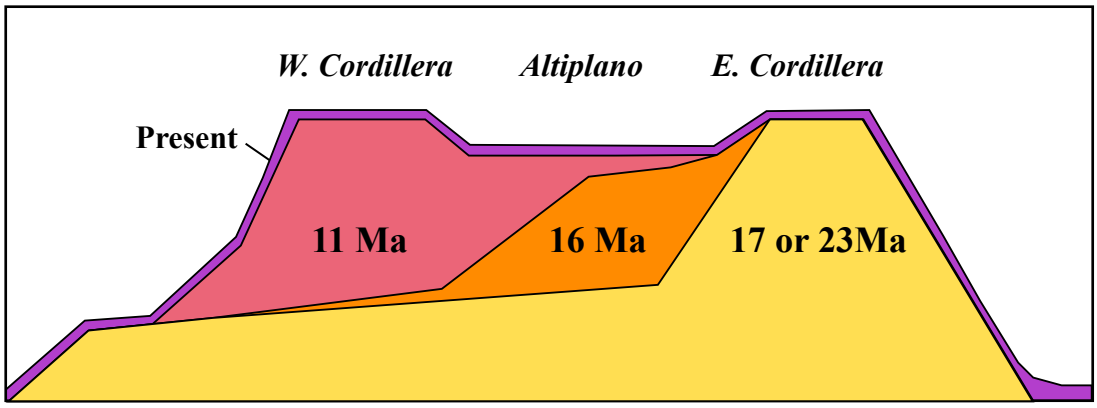

Figure 3.5. Schematic surface uplift model for the Peruvian Central Andes based on new volcanic glass paleoaltimetry (this study).

TABLE 3.1. ANCIENT GLASS SAMPLES

Sample name	Average δD (‰) VSMOW	2σ uncertainty	Average water content	Number of aliquots	Latitude (°S)	Longitude (°W)	Sample elevation (m)	Distance (km)	Best age (Ma)	Error (Ma)	Reference for age data
6–10 Ma											
PE17-056MOC	-49.98	3.29	2.3	3	-17.246	-71.000	1270	61.5	9.60	0.50	Quang et al. (2005)
PE17-057MOC	-39.14	3.29	4.5	3	-17.554	-71.084	911	27.2	9.77	0.12	Roperch et al. (2006)
PE17-088MOC	-55.96	3.20	2.9	6	-17.340	-70.981	1109	65.0	9.60	0.50	Quang et al. (2005)
PE18-303MACU	-206.74	4.09	3.0	6	-14.013	-70.465	4204	367.6	7.18	0.70	Pichavant et al. (1988)
PE18-306MACU	-199.41	5.14	2.9	2	-14.006	-70.475	4256	366.5	7.18	0.70	Pichavant et al. (1988)
PE18-308MACU	-186.61	4.09	3.1	3	-13.919	-70.509	4045	372.4	7.68	0.07	Cheilletz et al. (1992)
PE18-329MAC	-195.00	2.80	3.3	5	-13.865	-70.633	4070	372.8	7.80	0.20	Cheilletz et al. (1992)
PE18-331MAC	-185.92	4.09	5.4	3	-14.078	-70.433	4352	363.9	7.30	0.30	Cheilletz et al. (1990)
PE18-347TOM	-198.04	3.45	4.8	4	-14.540	-72.184	3928	234.3	6.10	0.20	Candiotti et al. (1990)
PE18-349TOM	-189.36	4.16	2.7	6	-14.540	-72.212	4149	233.0	6.10	0.20	Candiotti et al. (1990)
PE18-386MOC	-51.90	2.80	2.7	3	-17.313	-70.999	1031	55.0	9.60	0.50	Quang et al. (2005)
PE18-388MOC	-55.68	4.09	2.7	3	-17.216	-70.988	1267	65.1	9.60	0.50	Quang et al. (2005)
11–15 Ma											
PE028COT-AC	-63.74	6.29	0.5	2	-15.971	-72.712	3117	68.3	14.29	0.04	Schildgen et al. (2009)
PE028COT-AC*	-60.40		0.5	2	-15.971	-72.712	3117	68.3	14.29	0.04	Schildgen et al. (2009)
PE033COT-AC	-126.29	1.36	2.8	3	-15.769	-72.761	3920	84.8	14.10	0.30	Swanson (1998)
PE034COTUP-AC	-99.92	2.79	3.9	4	-15.763	-72.838	3473	84.1	14.29	0.04	Schildgen et al. (2009)
PE039COTB-AC	-149.11	1.44	4.6	3	-15.528	-72.819	4503	104.8	14.29	0.04	Schildgen et al. (2009)
PE16-032ESP	-178.10	3.00	2.6	2	-14.777	-71.380	3903	249.4	11.99	0.27	Rousse et al. (2005)
PE16-041LAM A	-175.74	3.00	5.0	2	-15.391	-70.457	3948	241.0	11.20	1.00	Klinck et al. (1986)
PE16-041LAM B	-189.67	3.00	5.0	3	-15.391	-70.457	3948	241.0	11.20	1.00	Klinck et al. (1986)
PE16-043PUN	-197.64	3.00	2.7	3	-16.337	-70.256	4461	188.2	11.27	0.35	Rousse et al. (2005)
PE17-058ILO	-63.32	4.82	4.9	6	-17.601	-71.215	256	15.9	14.20	0.40	Tosdal et al. (1981)
PE17-063MAJ	-47.10	3.20	2.3	6	-16.133	-72.191	1973	71.6	14.11	0.05	Schildgen et al. (2009)
PE17-065MAJ	-45.02	3.26	2.8	6	-16.155	-72.187	1917	69.3	14.11	0.05	Schildgen et al. (2009)
PE18-377MAJ	-61.49	3.45	2.8	6	-16.357	-72.133	1256	52.0	14.25	0.08	Thouret et al. (2007)
PE17-011PUN	-184.25	3.29	3.9	3	-16.068	-70.004	3963	228.0	10.97	0.47	Hennig (2005)
PE18-378MAJ	-63.38	3.45	2.9	6	-16.376	-72.146	1315	49.7	10.70	0.30	Noble et al. (2009b)
16–19 Ma											
PE016MADA-AC	-74.71	1.44	3.6	3	-16.357	-72.465	948	39.8	16.26	0.08	Schildgen et al. (2009)
PE020MAJ-AC	-68.04	1.44	3.3	3	-16.203	-72.391	885	59.7	16.40	0.40	Noble et al. (2009b)
PE16-002MAJ	-46.98	7.64	2.3	6	-16.580	-72.733	111	6.7	16.11	0.13	Roperch et al. (2006)
PE16-003MAJ B	-60.02	3.00	2.7	3	-16.209	-72.414	616	58.5	16.40	0.40	Noble et al. (2009b)
PE16-003MAJ C	-65.13	3.00	2.6	2	-16.209	-72.414	616	58.5	16.40	0.40	Noble et al. (2009b)
PE17-002LAG A	-86.58	3.29	9.8	3	-16.240	-71.056	4276	128.1	16.20	0.40	Bellon & Lefevre (1976)

PE17-008POM	-174.14	3.11	4.7	3	-16.262	-69.292	3830	256.1	16.90	0.90	Klinck et al. (1986)
PE17-012PUN	-159.29	4.75	4.3	3	-16.005	-70.081	4052	229.8	18.90	0.12	Boudesseul et al. (2000)
PE17-041CHV	-79.91	3.11	6.3	6	-15.392	-71.296	4173	193.7	18.82	0.06	Boudesseul et al. (2000)
PE17-053TOR	-77.36	3.29	0.5	3	-16.987	-70.702	3933	101.8	18.90	0.30	Quang et al. (2005)
PE17-053TOR*	-90.36	3.11	0.5	3	-16.987	-70.702	3933	101.8	18.90	0.30	Quang et al. (2005)
PE17-060MAJ	-47.52	3.29	4.4	3	-16.228	-72.079	1895	66.2	16.12	0.04	Schildgen et al. (2009)
PE17-069COT	-82.19	3.29	7.6	3	-15.071	-72.711	3641	157.8	18.90	0.40	Noble et al. (1984)
PE17-094MOC	-76.31	6.03	2.4	6	-16.985	-70.866	3176	94.3	18.90	0.50	Thouret et al. (2007)
PE18-369COR	-71.44	3.45	3.5	4	-16.359	-72.468	843	39.6	16.26	0.08	Schildgen et al. (2009)
PE18-371COR	-68.19	2.80	3.6	3	-16.358	-72.466	858	39.7	16.26	0.08	Schildgen et al. (2009)
23–26 Ma											
PE043MAD-AC	-34.52	2.28	5.7	3	-17.267	-71.165	1411	38.3	25.53	1.30	Roperch et al. (2006)
PE16-046MOC**	-43.43		3.5	3	-17.254	-70.925	1808	54.7	23.92	0.49	Thouret et al. (2007)
PE16-046MOC**	-53.87		3.6	3	-17.254	-70.925	1808	54.7	23.92	0.49	Thouret et al. (2007)
PE16-048MOC A**	-55.95		2.8	2	-17.251	-70.928	1742	64.7	23.92	0.49	Thouret et al. (2007)
PE16-048MOC A**	-58.36		3.6	2	-17.251	-70.928	1742	64.7	23.92	0.49	Thouret et al. (2007)
PE16-050MOC	-21.60	3.25	3.5	6	-17.250	-70.922	1709	65.1	23.92	0.49	Thouret et al. (2007)
PE17-080MOC	-72.68	3.29	5.7	3	-17.393	-71.013	1265	46.5	24.19	0.10	Roperch et al. (2006)
PE17-084MOC	-60.94	3.29	4.9	3	-17.395	-71.013	1361	46.5	24.19	0.10	Roperch et al. (2006)
PE17-087MOC	-52.14	10.64	5.7	5	-17.393	-71.013	1308	46.5	24.19	0.10	Roperch et al. (2006)
PE17-098TOQ	-40.98	3.29	3.3	3	-17.391	-70.794	1486	60.1	23.30	0.80	Tosdal et al. (1981)
17 or 23 Ma											
PE18-340PIC	-190.52	3.45	3.4	4	-14.577	-69.842	4641	351.1	23.50	0.40	Bonhomme et al. (1985b)
									16.81	0.25	Sandeman et al. (1997)
PE18-343PIC	-194.64	4.09	2.2	6	-14.591	-69.723	4536	353.5	23.89	0.93	Sandeman et al. (1997)
									17.90	0.60	Pichavant et al. (1988)

* Samples not included due to low peak area

** Samples not included due to low glass separate purity (<98% glass)

APPENDIX A

Supplemental Materials for Chapter II

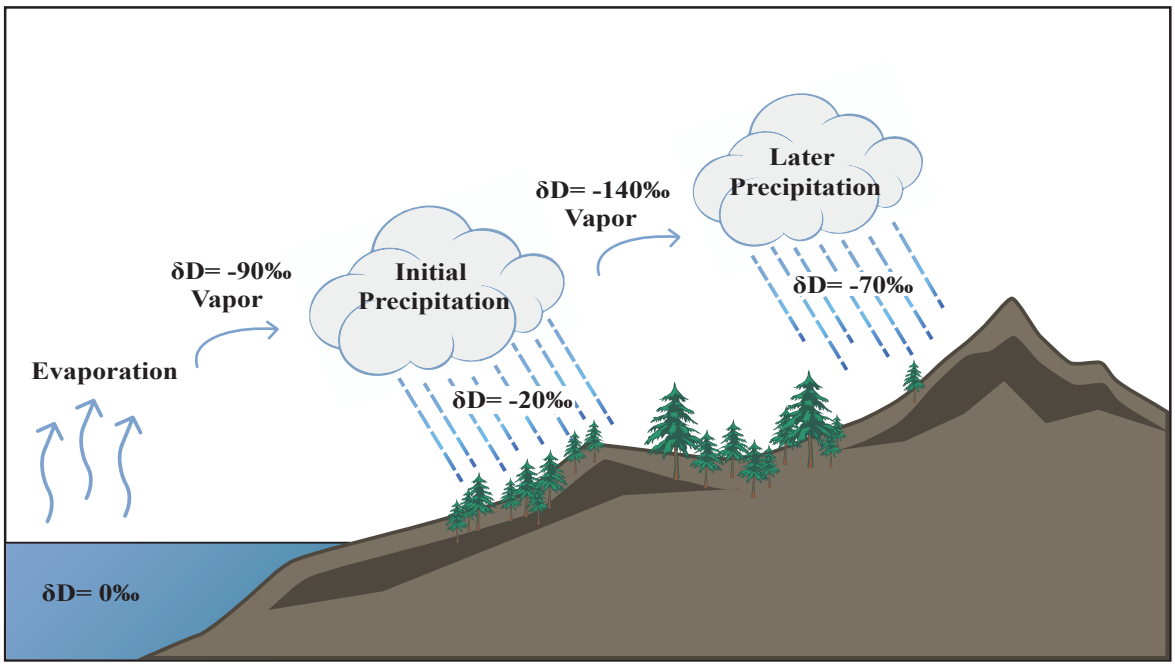

Figure A.1. Schematic depiction of rainout process used for hydrogen isotope paleoaltimetry modified from Hoefs (1997).

TABLE A.1. ≤ 5 Ma GLASS AGE DATA

Sample name	Best age (Ma)	Error (Ma)	Method	Material	Reference for age data
PE004ICH-AC	0.90	0.20	K-Ar	Total rock	Klinck et al. (1986)
PE009MAD-AC	0.80	0.40	K-Ar	Total rock	Klinck et al. (1986)
PE014SCC-AC	0.90	0.20	K-Ar	Total rock	Klinck et al. (1986)
PE042VIC-AC	1.64	0.07	Ar-Ar	Biotite	Paquereau et al. (2008)
PE050YUR-AC	1.77	0.15	Ar-Ar	Biotite	Paquereau et al. (2008)
PE16-007COT	2.04	0.14	Ar-Ar	Feldspar	Thouret et al. (2007)
PE16-009COT	2.04	0.14	Ar-Ar	Feldspar	Thouret et al. (2007)
PE16-010COT	2.04	0.14	Ar-Ar	Feldspar	Thouret et al. (2007)
PE16-011COT	2.04	0.14	Ar-Ar	Feldspar	Thouret et al. (2007)
PE16-013COT	2.04	0.14	Ar-Ar	Feldspar	Thouret et al. (2007)
PE17-020LUC	1.90	0.40	K-Ar	Total rock	Klinck et al. (1986)
PE17-029LAJ	4.77	0.20	Ar-Ar	Sanidine	Paquereau et al. (2008)
PE17-030CHV	2.20	0.15	Ar-Ar	Feldspar	Thouret et al. (2007)
PE17-032CHV	0.23	0.05	K-Ar	Total rock	Kaneoka & Guevara (1984)
PE17-034CHV B	0.40	0.10	K-Ar	Total rock	Olade (1980)
PE17-042SUM	4.97	0.03	Ar-Ar	Sanidine	Paquereau et al. (2008)
PE17-043VIC	4.95	0.03	Ar-Ar	Sanidine	Schildgen et al. (2009)
PE17-044VIC	4.95	0.03	Ar-Ar	Sanidine	Schildgen et al. (2009)
PE17-045VIC	4.95	0.03	Ar-Ar	Sanidine	Schildgen et al. (2012)
PE17-047MLL	4.90	0.30	Ar-Ar	Biotite	Quang et al. (2005)
PE17-049YUR	1.77	0.15	Ar-Ar	Biotite	Paquereau et al. (2008)
PE17-050MLL	4.90	0.30	Ar-Ar	Biotite	Quang et al. (2005)
PE17-055TOR	0.50	0.10	K-Ar	Total rock	Martinez & Cervantes (2003)
PE17-101AQP	4.83	0.03	Ar-Ar	Sanidine	Paquereau et al. (2008)
PE18-316CHV A	0.80	0.40	K-Ar	Total rock	Gerbe & Thouret (2003)
PE18-318ESP A	4.40	0.10	K-Ar	Sanidine	Noble et al. (2002a)
PE18-356CON	4.92	0.13	U-Pb	Volcanic rock	Sundell et al. (2019)
PE18-357CON	4.92	0.13	U-Pb	Volcanic rock	Sundell et al. (2019)
PE18-358CON	4.92	0.13	U-Pb	Volcanic rock	Sundell et al. (2019)
PE18-361PIC	2.01	0.03	Ar-Ar	Feldspar	Schildgen et al. (2009)
PE18-362ONC	2.01	0.03	Ar-Ar	Feldspar	Schildgen et al. (2009)
PE18-363MAJ	4.77	0.20	Ar-Ar	Sanidine	Paquereau et al. (2008)
PE18-367COR	1.64	0.07	Ar-Ar	Biotite	Paquereau et al. (2008)
PE18-374MAJ	1.64	0.07	Ar-Ar	Biotite	Paquereau et al. (2008)
PE18-381VIC	2.76	0.10	K-Ar	Pumice	Vatin -Perignon et al. (1996)
PE18-390MOC	5.00	0.30	Ar-Ar	Biotite	Quang et al. (2005)
PE18-391JOY	4.90	0.30	Ar-Ar	Biotite	Quang et al. (2005)
PE18-392AQP	3.05	3.40	K-Ar	Ignimbrite	Vatin -Perignon et al. (1996)

TABLE A.2. LIST OF STANDARDS USED IN ALL GLASS ANALYSES

Standard	Material	Known Reference Value (VSMOW)	Standard uncertainty (1 sigma)	Calculated average value	Calculated uncertainty (1 sigma)	Difference between reference and measured value	Year used in analysis	TCEA reactor number
International Atomic Energy Agency								
IAEA-CH-7	Polyethylene foil	-100.3	2	-104.7	0.62	4.39	2014	1
IAEA-CH-7	Polyethylene foil	-100.3	2	-103.3	0.96	3.00	2014	2
IAEA-CH-7	Polyethylene foil	-100.3	2	-100.3	4.09	0.03	2016	1
NBS 22	Oil, liquid	-119.6	0.6	-119.0	0.80	0.59	2014	1
NBS 22	Oil, liquid	-119.6	0.6	-116.8	1.19	2.75	2014	2
NBS 22	Oil, liquid	-119.6	0.6	-117.4	3.15	2.15	2016	1
NBS 22	Oil, liquid	-119.6	0.6	-117.9	3.29	1.73	2/2018	1
NBS 22	Oil, liquid	-119.6	0.6	-118.6	3.20	1.04	2/2018	2
NBS 22	Oil, liquid	-119.6	0.6	-117.0	2.99	2.56	12/2018	1
NBS 22	Oil, liquid	-119.6	0.6	-114.1	4.34	5.45	12/2018	2
IAEA-CH-3	Cellulose	-35.5	2.1	-31.0	4.10	4.47	2016	1
IAEA-CH-3	Cellulose	-35.5	2.1	-32.3	3.64	3.23	2/2018	1
NBS 30	Biotite	-65.7	0.3	-64.2	2.05	1.54	2014	1
NBS 30	Biotite	-65.7	0.3	-64.7	2.37	0.98	2014	2
NBS 30	Biotite	-65.7	0.3	-70.7	2.35	5.01	2016	1
United States Geological Survey								
USGS 57	Biotite	-91.5	2.4	-94.6	2.92	3.09	2/2018	1
USGS 57	Biotite	-91.5	2.4	-91.6	3.40	0.12	2/2018	2
USGS 57	Biotite	-91.5	2.4	-93.0	4.00	1.49	12/2018	1
USGS 57	Biotite	-91.5	2.4	-95.5	2.28	4.03	12/2018	2
USGS 58	Muscovite	-28.4	1.6	-32.6	1.98	4.23	2/2018	1
USGS 58	Muscovite	-28.4	1.6	-28.8	2.07	0.38	2/2018	2
USGS 58	Muscovite	-28.4	1.6	-28.3	4.78	0.08	12/2018	1
USGS 58	Muscovite	-28.4	1.6	-27.8	2.44	0.58	12/2018	2

Light Stable Isotope Lab UT-Austin

SN09057SH	Glass (In house)	-155	3.0	-149.5	0.13	5.48	2014	1
SN09057SH	Glass (In house)	-155	3.0	-154.1	3.08	0.92	2/2018	1
SN09057SH	Glass (In house)	-155	3.0	-154.9	2.55	0.15	2/2018	2
SN09052RW	Glass (In house)	-165	3.1	-164.4	2.83	0.61	2016	1
SN09052RW	Glass (In house)	-165	3.1	-164.6	4.79	0.44	12/2018	1
SN09052RW	Glass (In house)	-165	3.1	-165.1	2.20	0.09	12/2018	2

APPENDIX B

Supplemental Materials for Chapter III

PE16-003MAJ (B)

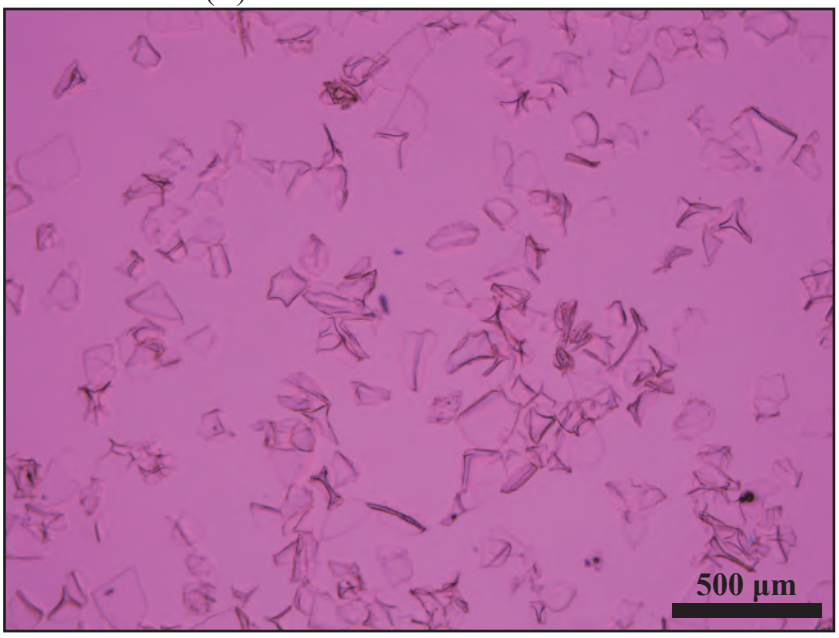

PE16-009COT

PE16-032ESP

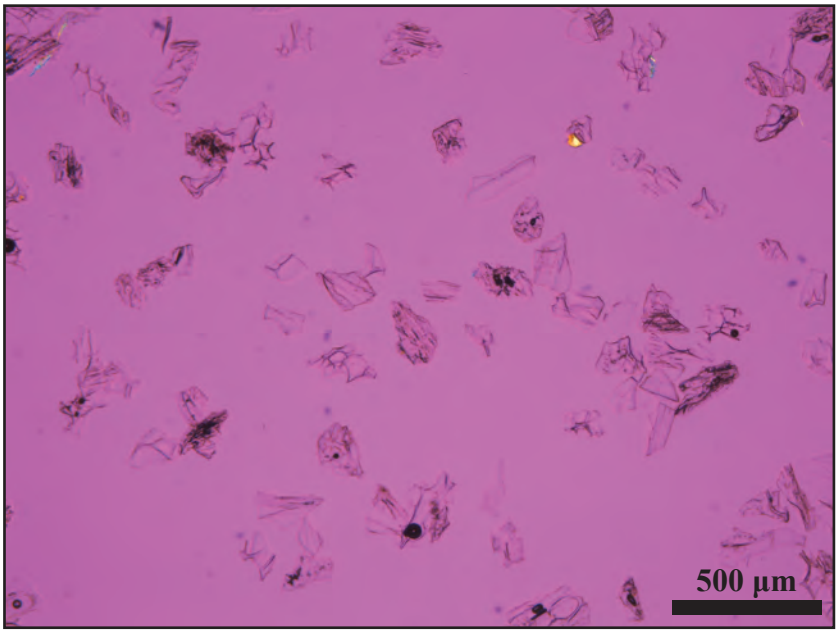

PE16-041LAM(A)

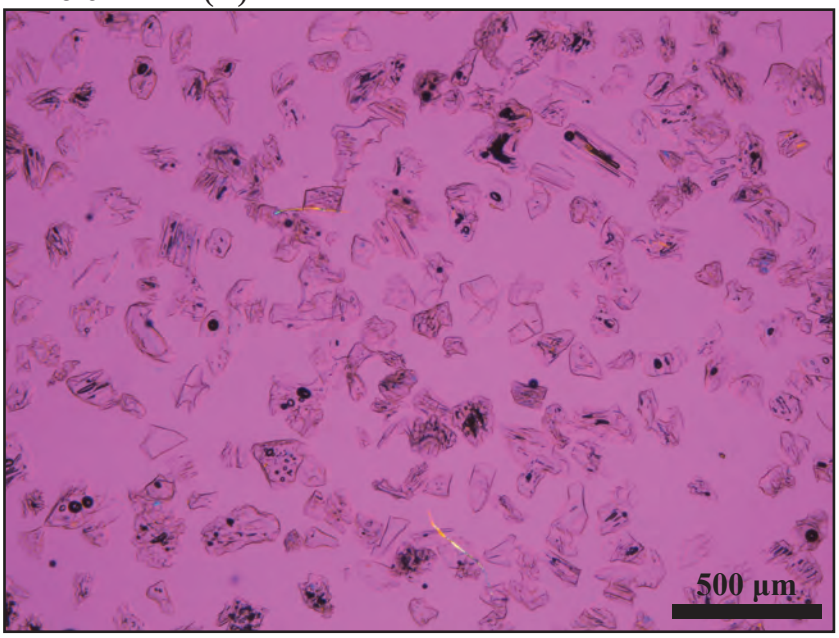

PE16-043PUN

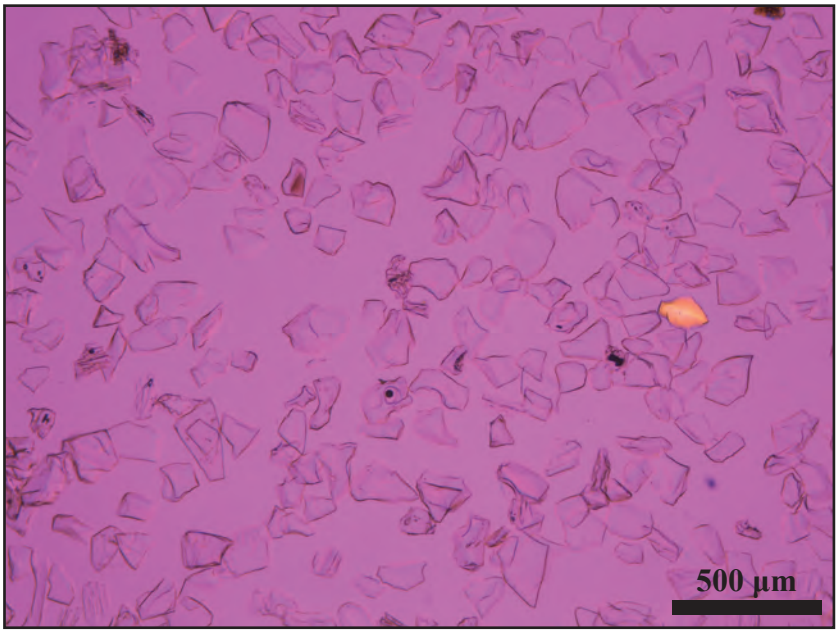

PE16-050MOC

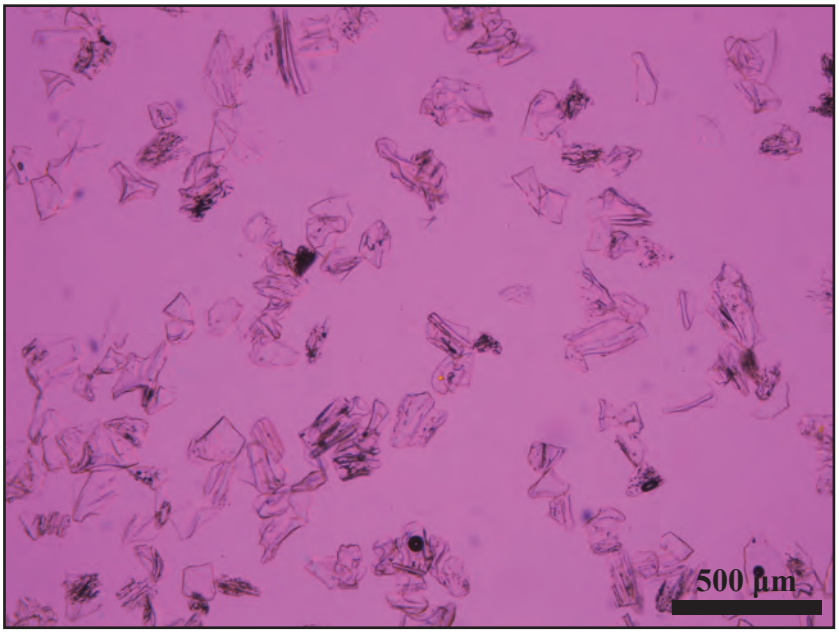

PE17-042SUM (PPL)

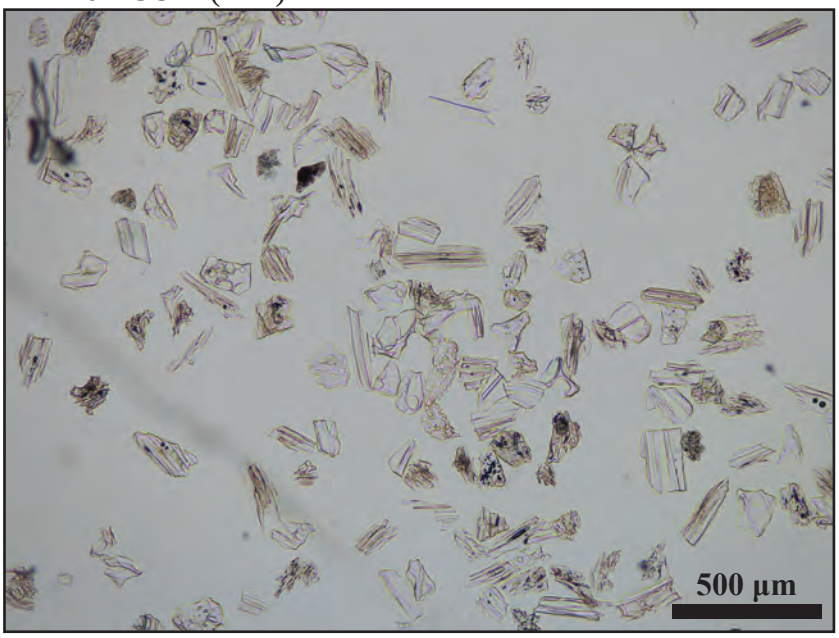

PE17-042SUM (XPL)

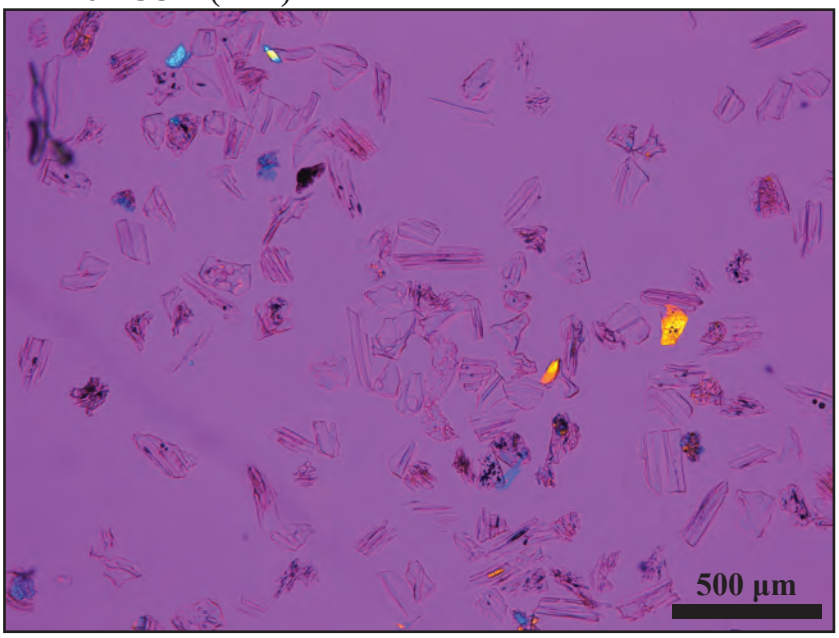

PE17-060MAJ

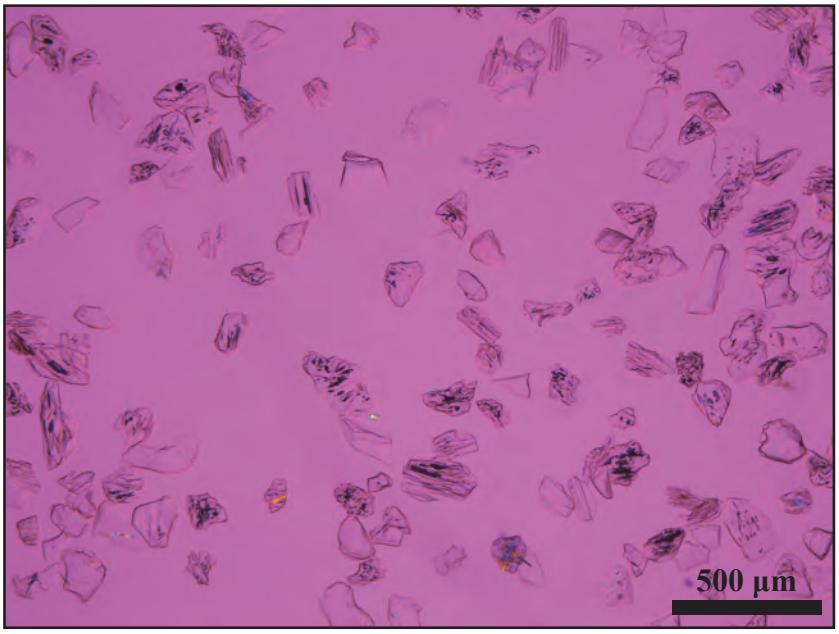

PE17-058ILO

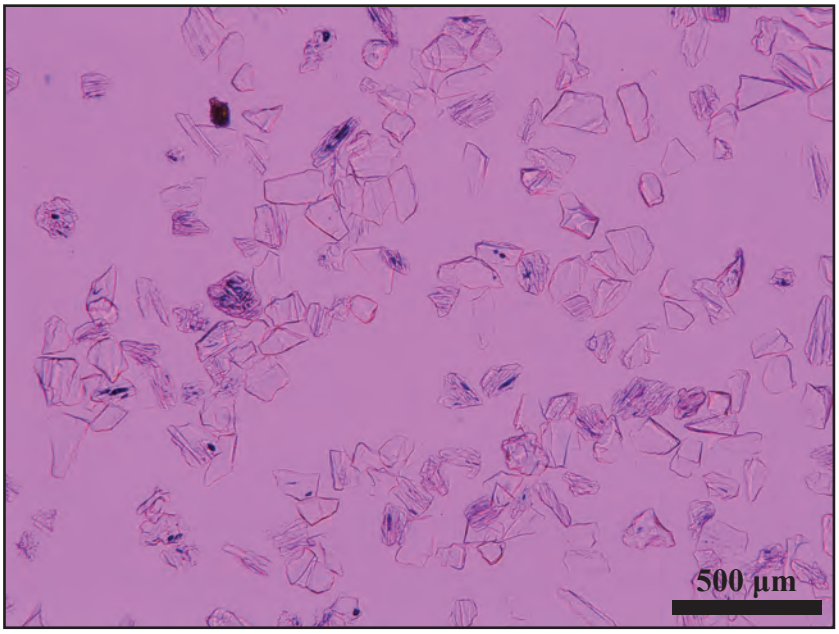

PE17-098TOQ

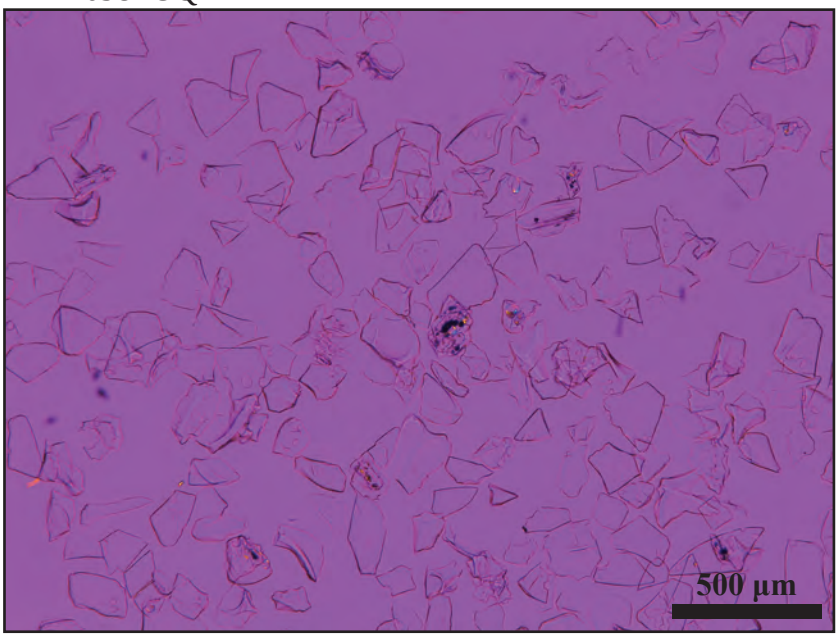

PE18-318ESP

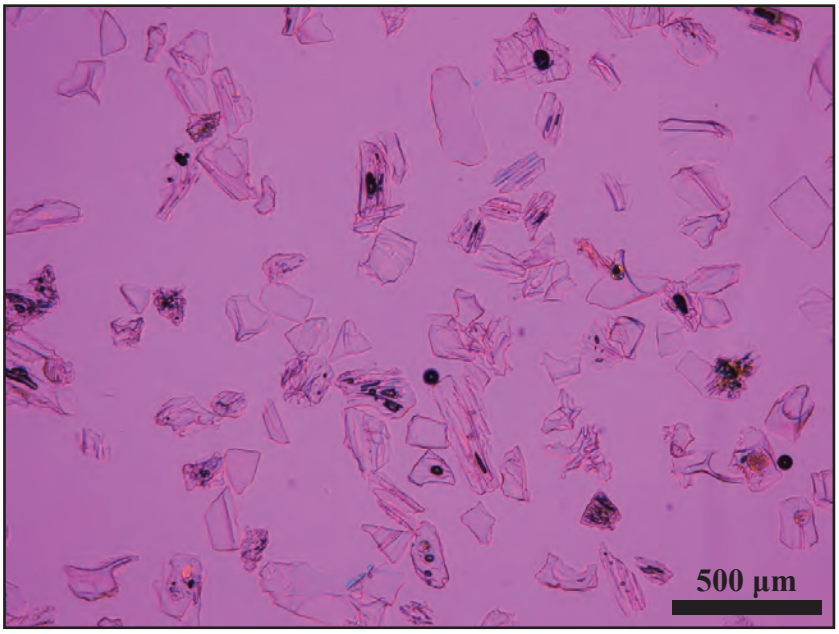

PE18-347TOM

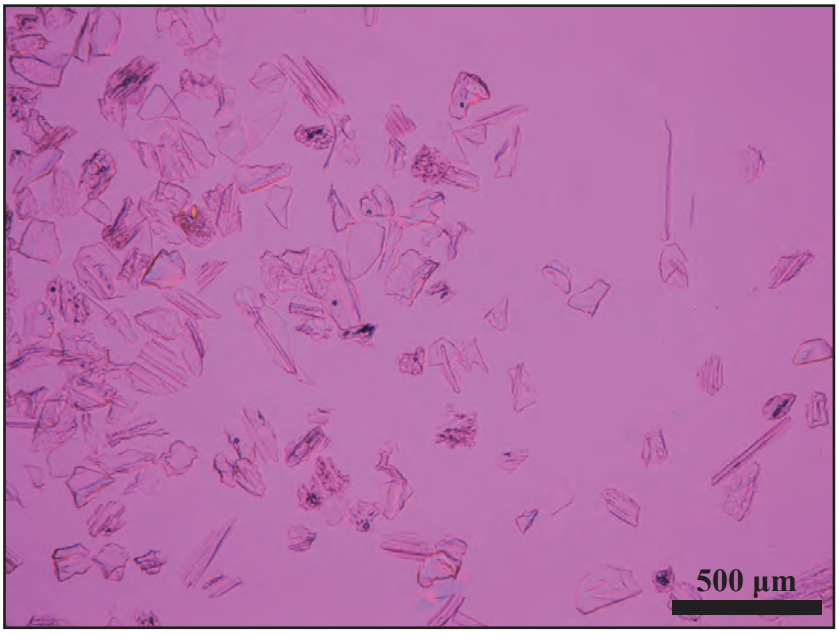

PE18-356CON

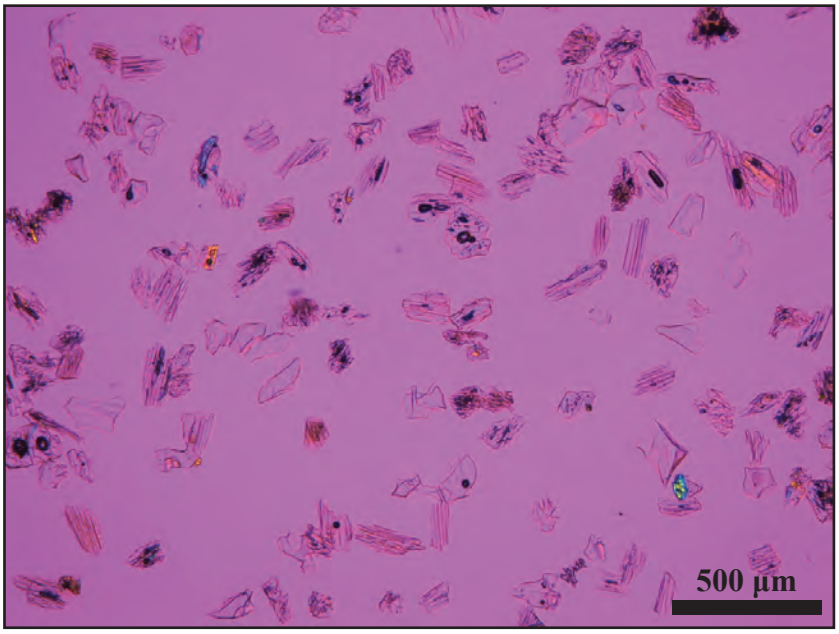

PE18-357CON

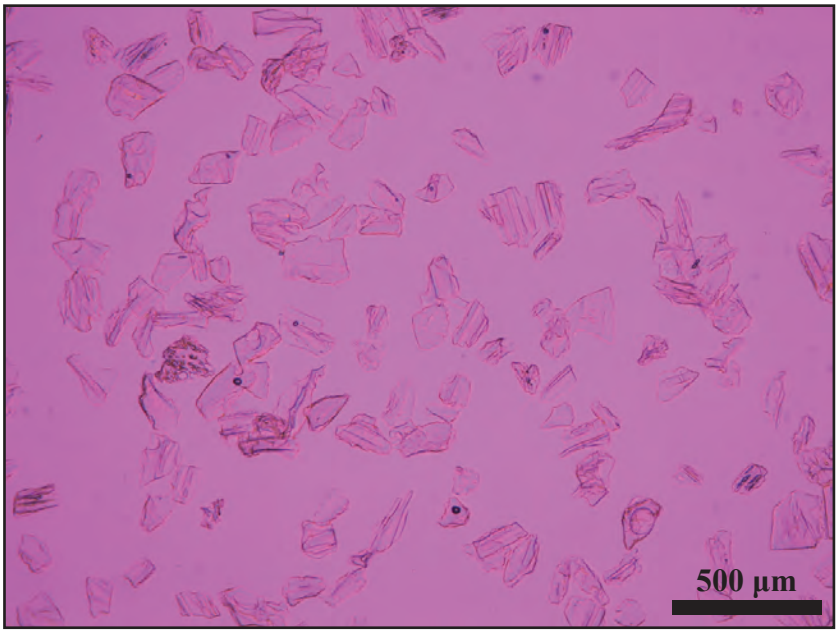

PE18-361PIC

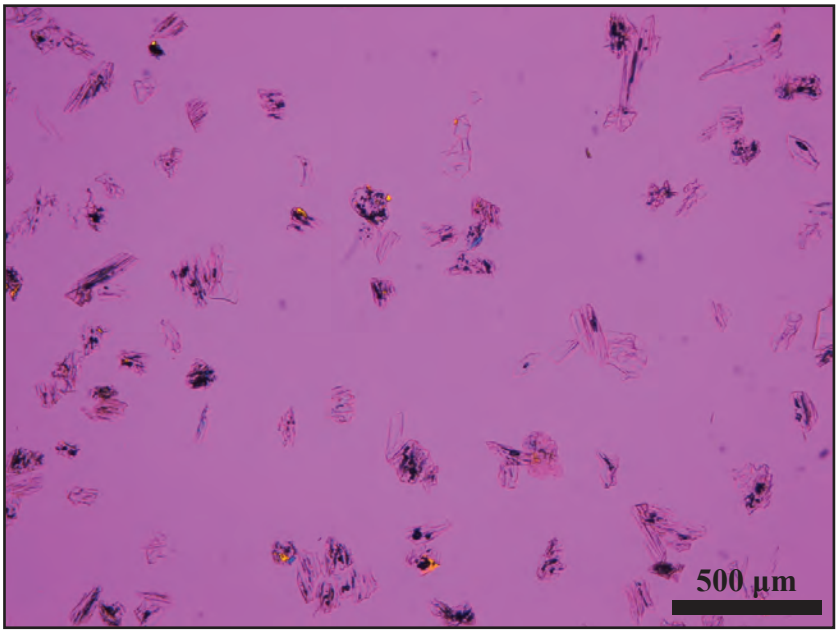

PE18-362ONC

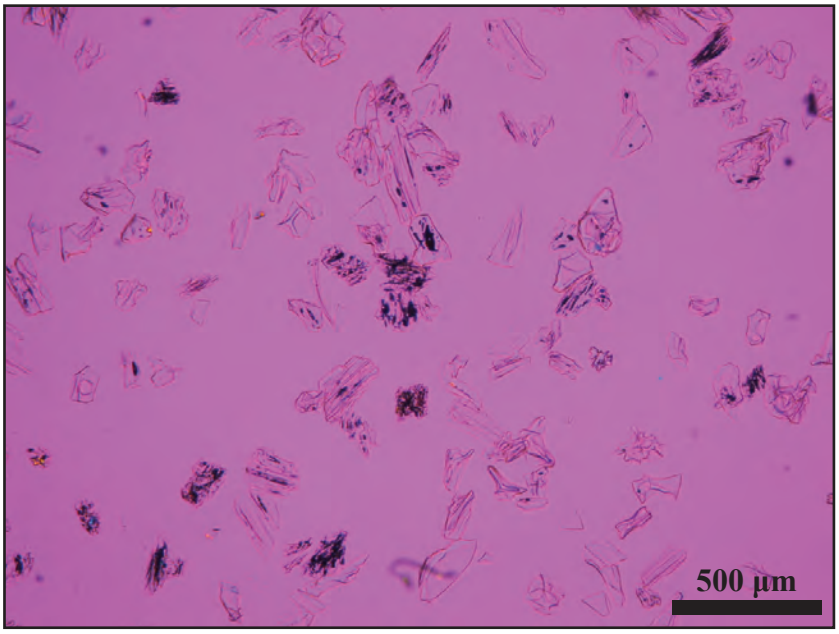

PE18-369COR

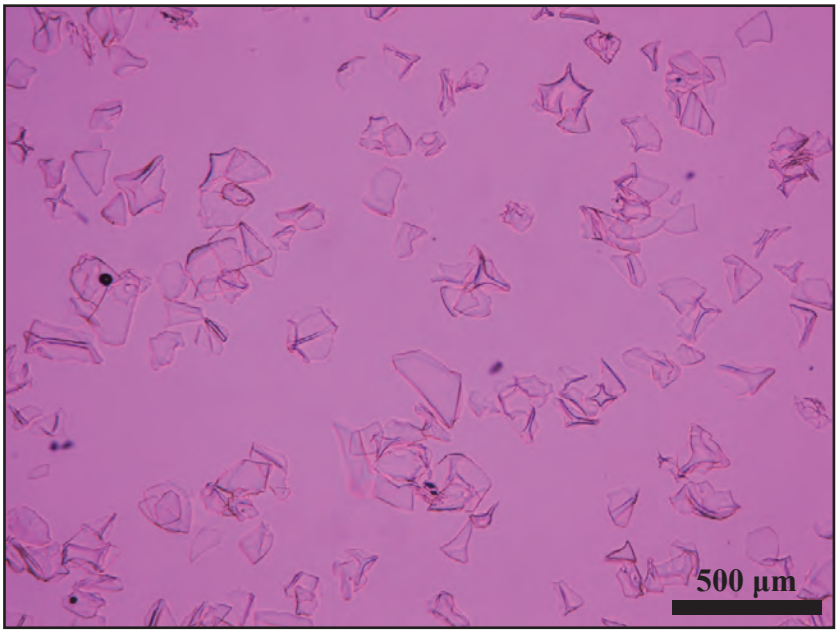

PE18-371COR

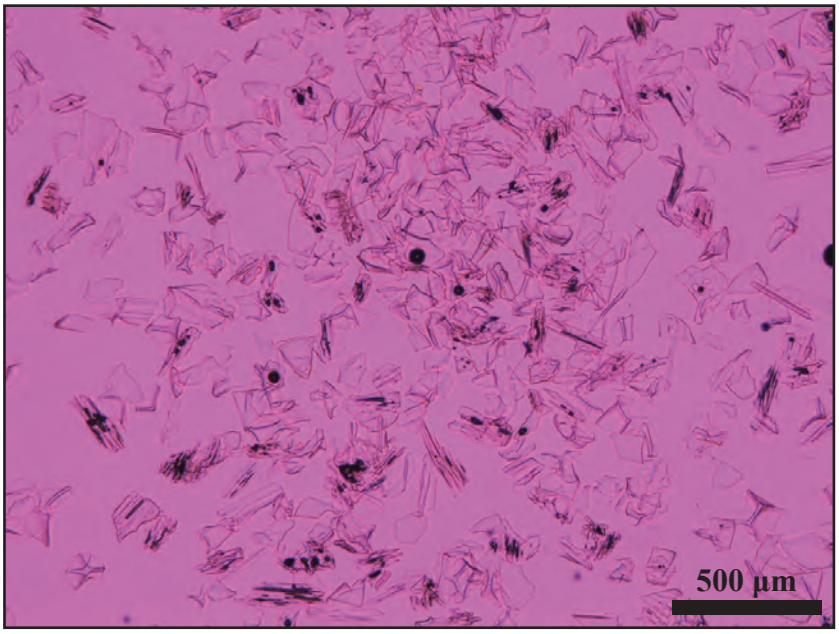

PE16-007COT

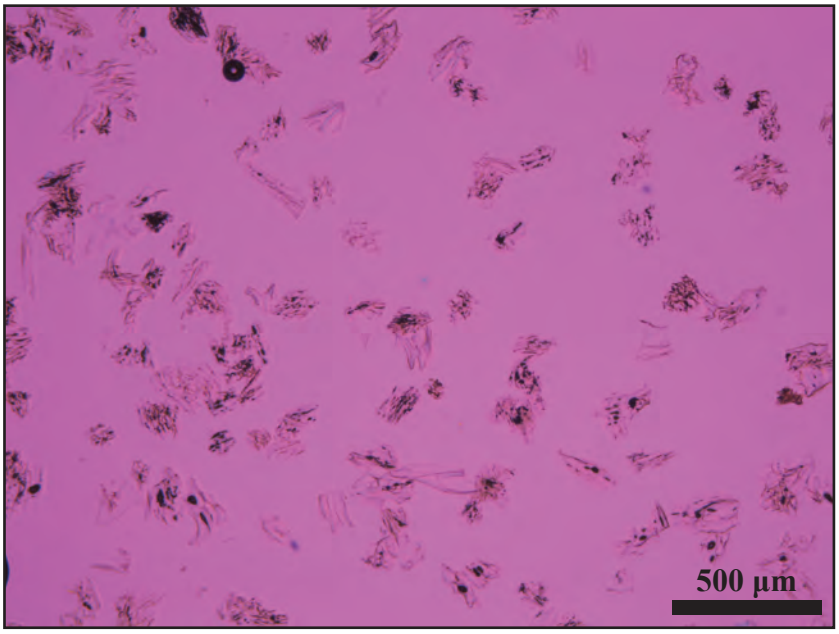

Volcanic Glass Morphology

Pumice shards

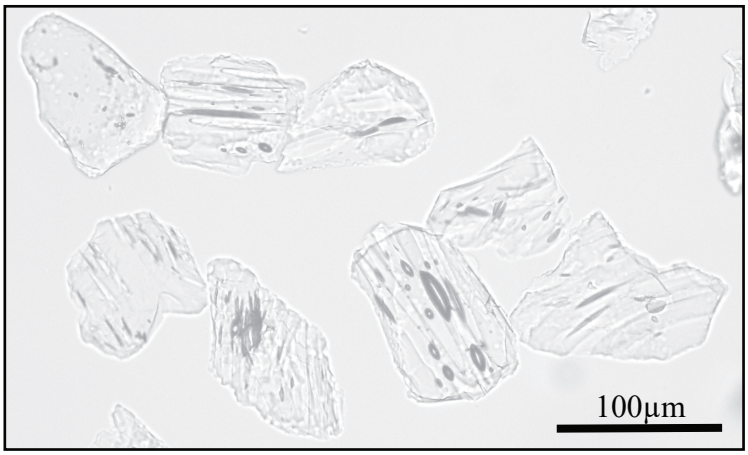

Bubble wall and pumice shards

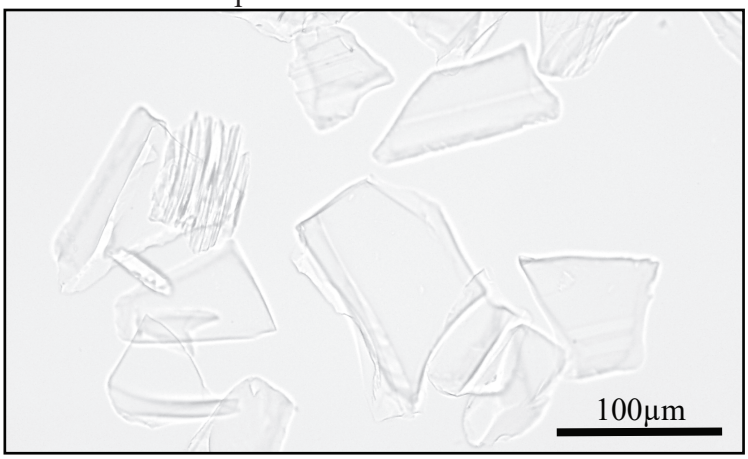

Adjoining bubble wall shards

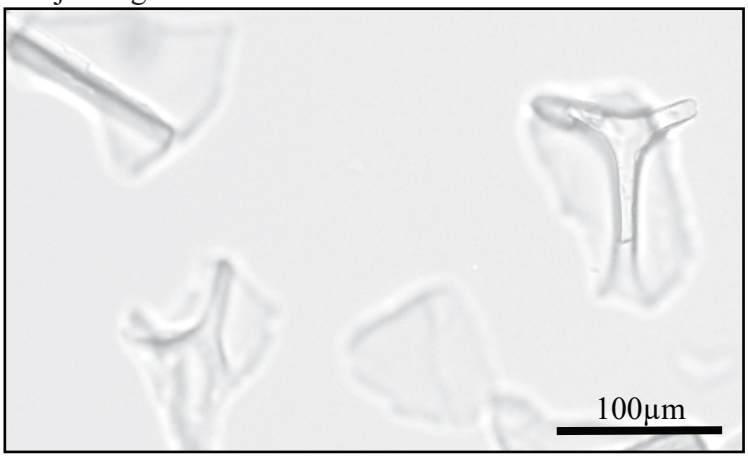

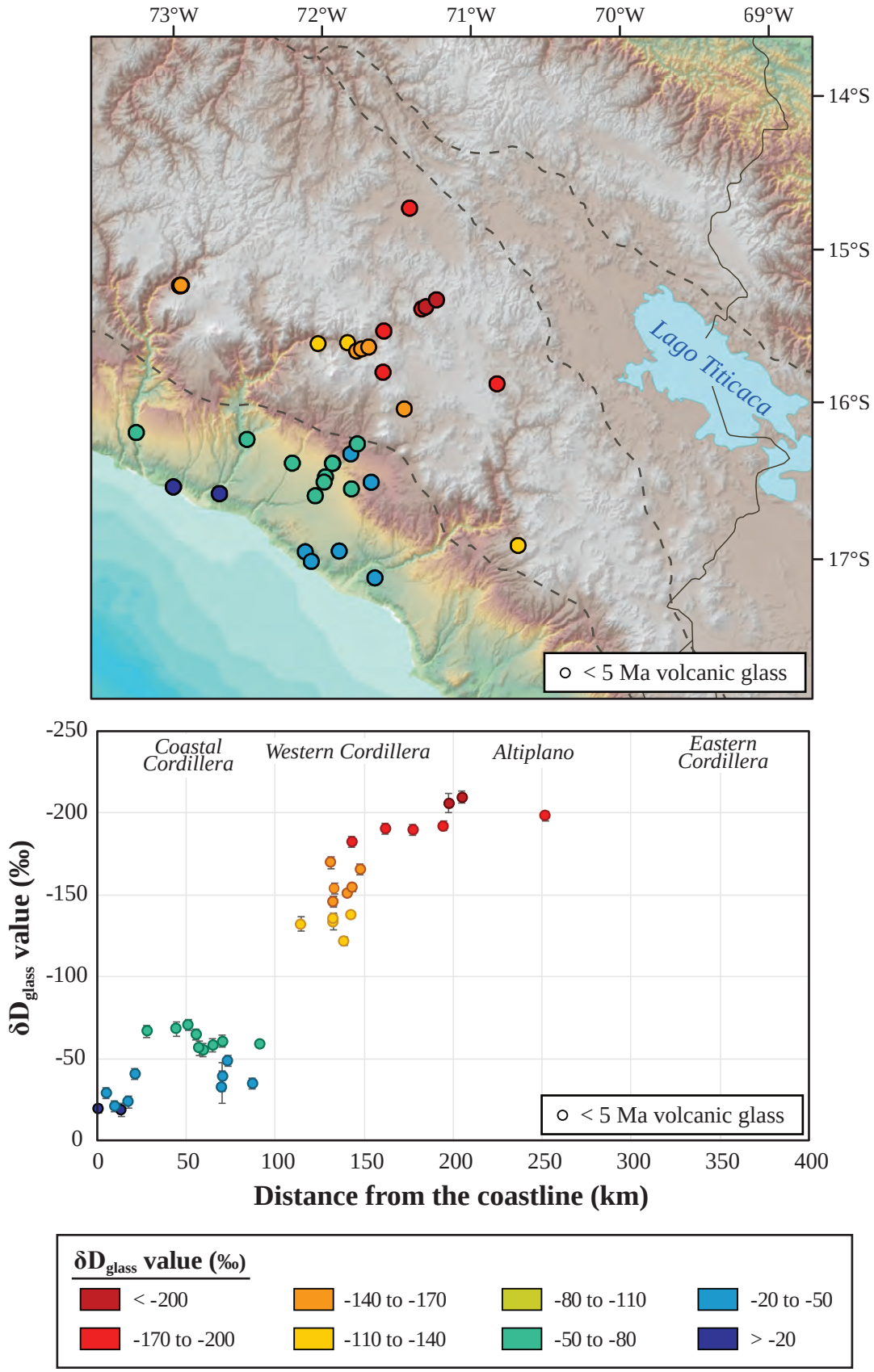
73°W
72°W
71°W
70°W
69°W
14°S
15°S
16°S
17°S
Lago Titicaca
< 5 Ma volcanic glass
Coastal Cordillera
Western Cordillera
Altiplano
Eastern Cordillera
δD glass value (‰)
-250
-200
-150
-100
-50
0
0
50
100
150
200
250
300
350
400
Distance from the coastline (km)
< 5 Ma volcanic glass
δD glass value (‰)
< -200
-170 to -200
-140 to -170
-110 to -140
-80 to -110
-50 to -80
-20 to -50
> -20

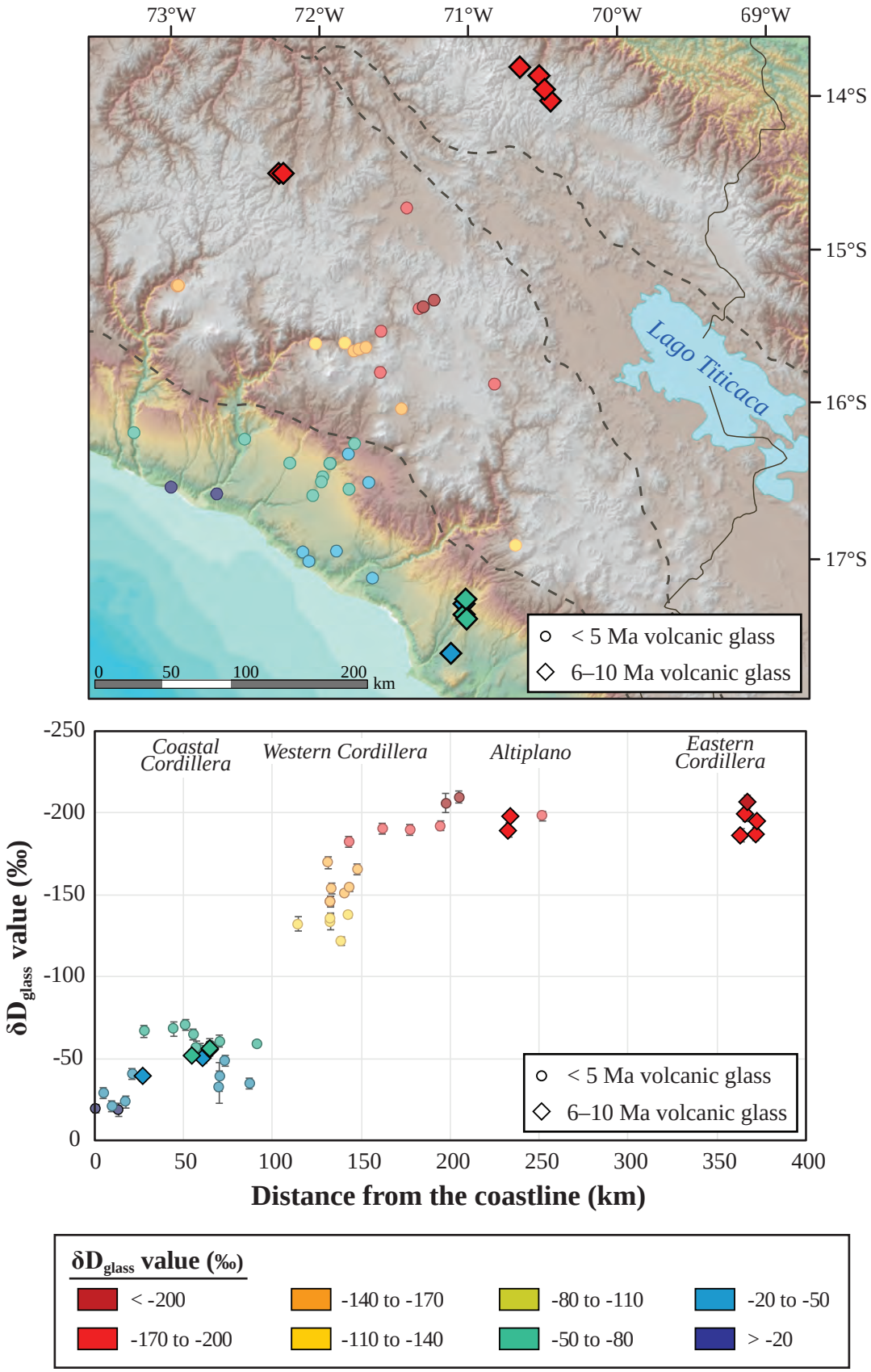
73°W
72°W
71°W
70°W
69°W
14°S
15°S
16°S
17°S
Lago Titicaca
0
50
100
200
km
< 5 Ma volcanic glass
6–10 Ma volcanic glass
Coastal Cordillera
Western Cordillera
Altiplano
Eastern Cordillera
δD glass value (‰)
-250
-200
-150
-100
-50
0
0
50
100
150
200
250
300
350
400
Distance from the coastline (km)
< 5 Ma volcanic glass
6–10 Ma volcanic glass
δD glass value (‰)
< -200
-170 to -200
-140 to -170
-110 to -140
-80 to -110
-50 to -80
-20 to -50
> -20

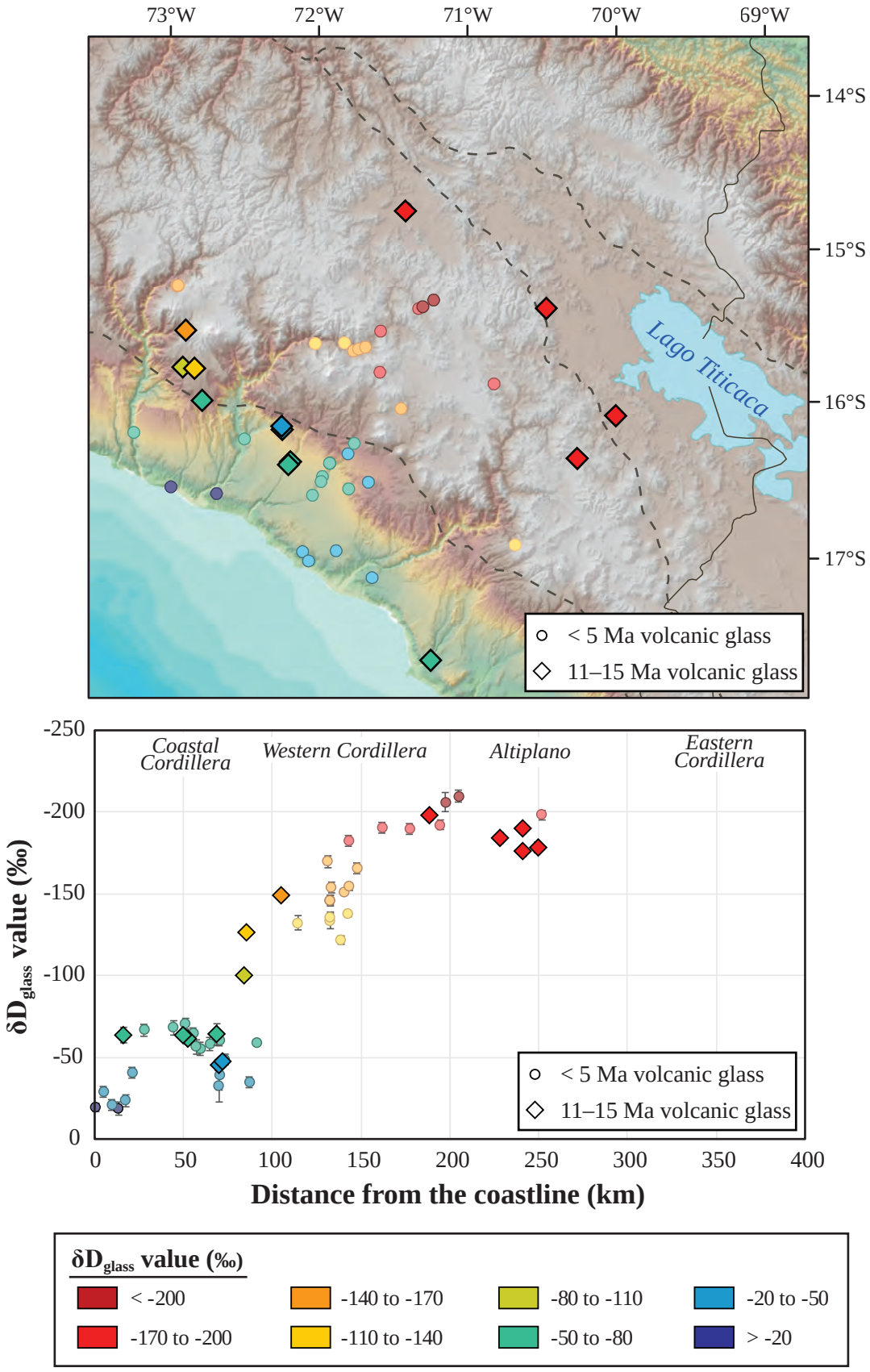
73°W
72°W
71°W
70°W
69°W
14°S
15°S
16°S
17°S
Lago Titicaca
< 5 Ma volcanic glass
11–15 Ma volcanic glass
Coastal Cordillera
Western Cordillera
Altiplano
Eastern Cordillera
δD glass value (‰)
-250
-200
-150
-100
-50
0
0
50
100
150
200
250
300
350
400
Distance from the coastline (km)
< 5 Ma volcanic glass
11–15 Ma volcanic glass
δD glass value (‰)
< -200
-170 to -200
-140 to -170
-110 to -140
-80 to -110
-50 to -80
-20 to -50
> -20

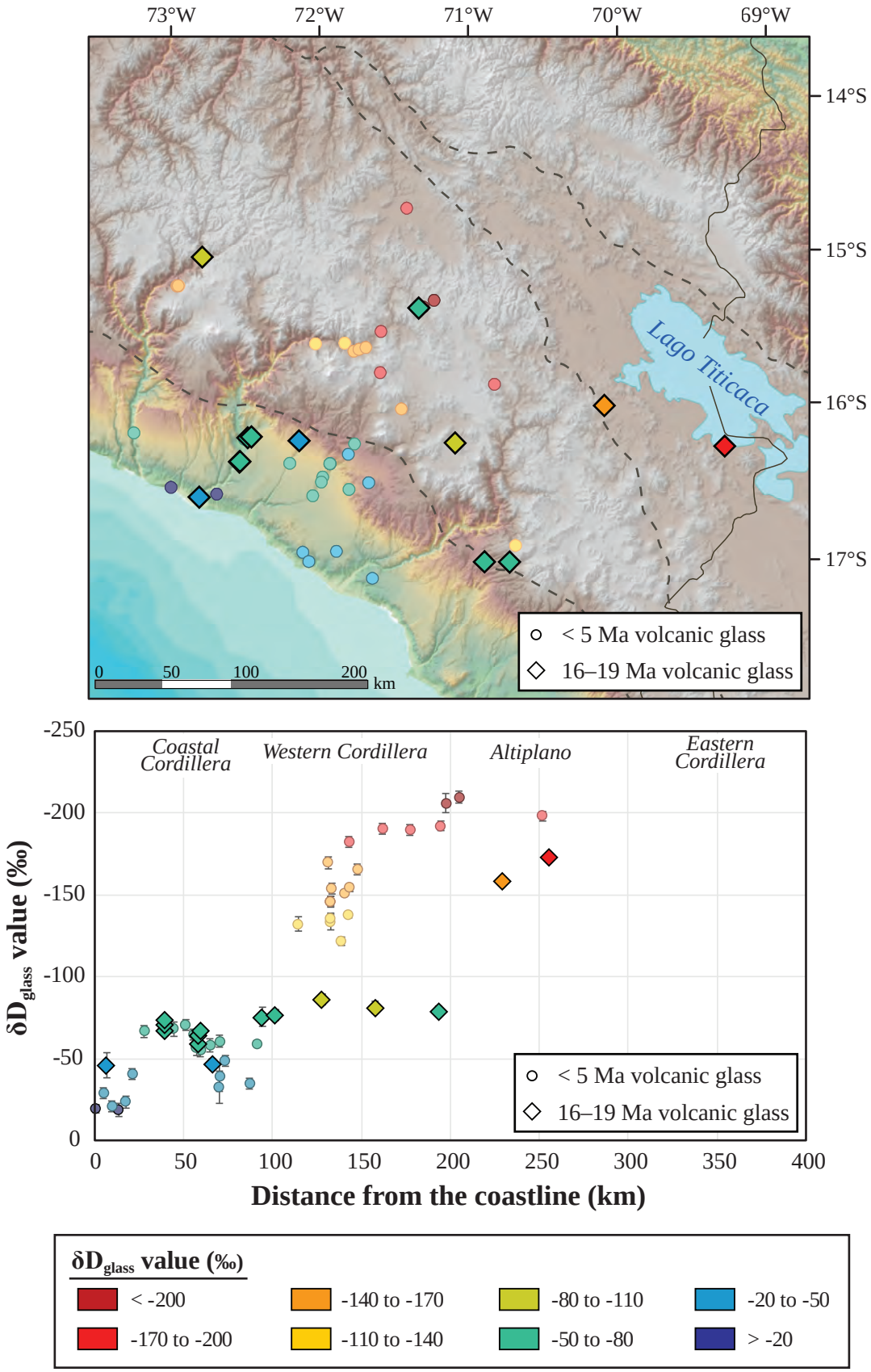
73°W
72°W
71°W
70°W
69°W
14°S
15°S
16°S
17°S
Lago Titicaca
0
50
100
200
km
< 5 Ma volcanic glass
16–19 Ma volcanic glass
Coastal Cordillera
Western Cordillera
Altiplano
Eastern Cordillera
δD glass value (‰)
-250
-200
-150
-100
-50
0
0
50
100
150
200
250
300
350
400
Distance from the coastline (km)
< 5 Ma volcanic glass
16–19 Ma volcanic glass
δD glass value (‰)
< -200
-170 to -200
-140 to -170
-110 to -140
-80 to -110
-50 to -80
-20 to -50
> -20

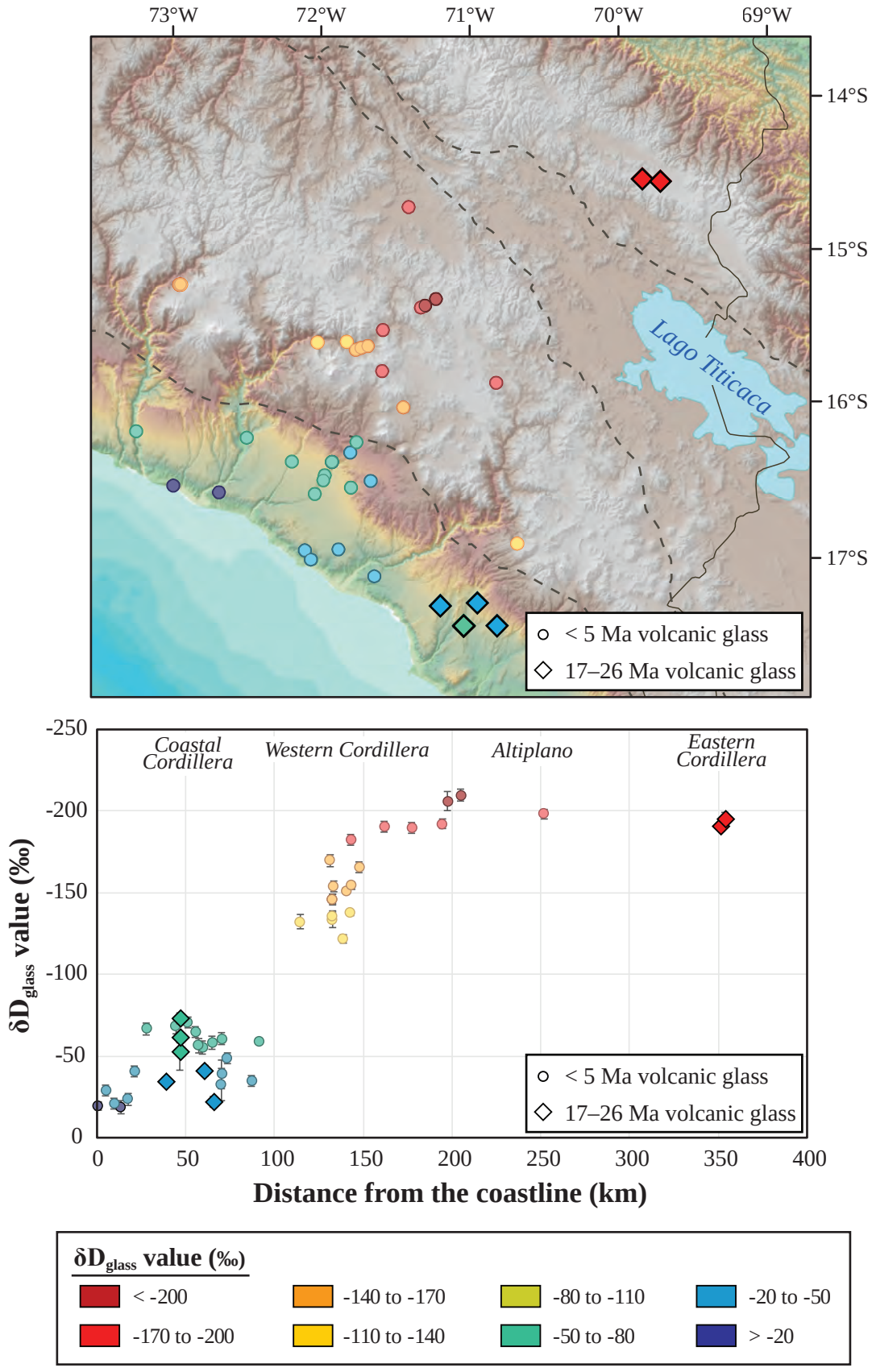
73°W
72°W
71°W
70°W
69°W
14°S
15°S
16°S
17°S
Lago Titicaca
< 5 Ma volcanic glass
17–26 Ma volcanic glass
Coastal Cordillera
Western Cordillera
Altiplano
Eastern Cordillera
δD glass value (‰)
-250
-200
-150
-100
-50
0
0
50
100
150
200
250
300
350
400
Distance from the coastline (km)
< 5 Ma volcanic glass
17–26 Ma volcanic glass
δD glass value (‰)
< -200
-170 to -200
-140 to -170
-110 to -140
-80 to -110
-50 to -80
-20 to -50
> -20

TABLE B.1. ANCIENT GLASS AGE DATA

Sample name	Best age (Ma)	Error (Ma)	Method	Material	Reference for age data
6-10 Ma					
PE17-056MOC	9.60	0.50	Ar-Ar	Biotite	Quang et al. (2005)
PE17-057MOC	9.77	0.12	Ar-Ar	Biotite	Roperch et al. (2006)
PE17-088MOC	9.60	0.50	Ar-Ar	Biotite	Quang et al. (2005)
PE18-303MACU	7.18	0.70	K-Ar	Biotite	Pichavant et al. (1988)
PE18-306MACU	7.18	0.70	K-Ar	Biotite	Pichavant et al. (1988)
PE18-308MACU	7.68	0.07	Ar-Ar	Sanidine	Cheilletz et al. (1992)
PE18-329MAC	7.80	0.20	Ar-Ar	Sanidine	Cheilletz et al. (1992)
PE18-331MAC	7.30	0.30	Ar-Ar	Muscovite	Cheilletz et al. (1990)
PE18-347TOM	6.10	0.20	K-Ar	Biotite	Candiotti et al. (1990)
PE18-349TOM	6.10	0.20	K-Ar	Biotite	Candiotti et al. (1990)
PE18-386MOC	9.60	0.50	Ar-Ar	Biotite	Quang et al. (2005)
PE18-388MOC	9.60	0.50	Ar-Ar	Biotite	Quang et al. (2005)
11-15 Ma					
PE028COT-AC	14.29	0.04	Ar-Ar	Sanidine	Schildgen et al. (2009)
PE033COT-AC	14.10	0.30	K-Ar	Biotite	Swanson (1998)
PE034COTUP-AC	14.29	0.04	Ar-Ar	Sanidine	Schildgen et al. (2009)
PE039COTB-AC	14.29	0.04	Ar-Ar	Sanidine	Schildgen et al. (2009)
PE16-032ESP	11.99	0.27	Ar-Ar	Sanidine	Rousse et al. (2005)
PE16-041LAM A	11.20	1.00	K-Ar	Biotite	Klinck et al. (1986)
PE16-041LAM B	11.20	1.00	K-Ar	Biotite	Klinck et al. (1986)
PE16-043PUN	11.27	0.35	Ar-Ar	Biotite	Rousse et al. (2005)
PE17-058ILO	14.20	0.40	K-Ar	Biotite	Tosdal et al. (1981)
PE17-063MAJ	14.11	0.05	Ar-Ar	Sanidine	Schildgen et al. (2009)
PE17-065MAJ	14.11	0.05	Ar-Ar	Sanidine	Schildgen et al. (2009)
PE18-377MAJ	14.25	0.08	Ar-Ar	Sanidine	Thouret et al. (2007)
PE17-011PUN	10.97	0.47	Ar-Ar	Biotite	Hennig (2005)
PE18-378MAJ	10.70	0.30	K-Ar	Sanidine	Noble et al. (2009b)
16-19 Ma					
PE016MADA-AC	16.26	0.08	Ar-Ar	Sanidine	Schildgen et al. (2009)
PE020MAJ-AC	16.40	0.40	K-Ar	Biotite	Noble et al. (2009b)
PE16-002MAJ	16.11	0.13	Ar-Ar	Biotite	Roperch et al. (2006)
PE16-003MAJ B	16.40	0.40	K-Ar	Biotite	Noble et al. (2009b)
PE16-003MAJ C	16.40	0.40	K-Ar	Biotite	Noble et al. (2009b)
PE17-002LAG A	16.20	0.40	K-Ar	Pumice	Bellon & Lefevre (1976)
PE17-008POM	16.90	0.90	K-Ar	Hornblende	Klinck et al. (1986)
PE17-012PUN	18.90	0.12	Ar-Ar	Biotite	Boudesseul et al. (2000)

PE17-041CHV	18.82	0.06	Ar-Ar	Biotite	Boudesseul et al. (2000)
PE17-053TOR	18.90	0.30	Ar-Ar	Biotite	Quang et al. (2005)
PE17-060MAJ	16.12	0.04	Ar-Ar	Sanidine	Schildgen et al. (2009)
PE17-069COT	18.90	0.40	K-Ar	Biotite	Noble et al. (1984)
PE17-094MOC	18.90	0.50	Ar-Ar	Sanidine	Thouret et al. (2007)
PE18-369COR	16.26	0.08	Ar-Ar	Sanidine	Schildgen et al. (2009)
PE18-371COR	16.26	0.08	Ar-Ar	Sanidine	Schildgen et al. (2009)
23-26 Ma					
PE043MAD-AC	25.53	1.30	Ar-Ar	Feldspar	Roperch et al. (2006)
PE16-050MOC	23.92	0.49	Ar-Ar	Sanidine	Thouret et al. (2007)
PE17-080MOC	24.19	0.10	Ar-Ar	Biotite	Roperch et al. (2006)
PE17-084MOC	24.19	0.10	Ar-Ar	Biotite	Roperch et al. (2006)
PE17-087MOC	24.19	0.10	Ar-Ar	Biotite	Roperch et al. (2006)
PE17-098TOQ	23.30	0.80	K-Ar	Biotite	Tosdal et al. (1981)
17 or 23 Ma					
PE18-340PIC	23.50	0.40	K-Ar	Biotite	Bonhomme et al. (1985b)
	16.81	0.25	Ar-Ar	Sanidine	Sandeman et al. (1997)
PE18-343PIC	23.89	0.93	Ar-Ar	Biotite	Sandeman et al. (1997)
	17.90	0.60	K-Ar	Muscovite	Pichavant et al. (1988)

APPENDIX C

Detrital Zircon U-Pb Geochronology and Detailed Stratigraphy

DETRITAL ZIRCON U-Pb ANALYSES

Analysis	U (ppm)	U/Th	207Pb/ 235U	±	206Pb/ 238U	±	err. corr.	207Pb/ 235U Age (Ma)	± (Ma)	206Pb/ 238U Age (Ma)	± (Ma)	207Pb/ 206Pb Age (Ma)	± (Ma)	Best age (Ma)	± (Ma)	Disc (%)
PE17-074MOC: 17°23.94'S, 071°00.71'W																
PE17-074MOC_1	95.2	9.2	0.2200	0.0220	0.0274	0.0010	0.0274	198.0	18.0	173.8	6.0	410	200	173.8	6.0	12.2
PE17-074MOC_2	547.0	5.6	0.0333	0.0028	0.0050	0.0001	0.1795	33.1	2.8	32.0	0.9	80	150	32.0	0.9	3.2
PE17-074MOC_3	909.0	6.4	0.1808	0.0045	0.0264	0.0003	0.1397	168.4	3.8	167.7	1.8	174	53	167.7	1.8	0.4
PE17-074MOC_4	1226.0	4.5	0.0326	0.0016	0.0051	0.0001	0.1427	32.6	1.6	32.5	0.6	59	90	32.5	0.6	0.4
PE17-074MOC_5	214.0	17.2	0.1810	0.0120	0.0275	0.0006	0.1671	169.0	10.0	174.6	3.8	80	110	174.6	3.8	3.3
PE17-074MOC_6	135.3	6.8	0.1150	0.0090	0.0168	0.0005	0.0258	109.3	8.1	107.5	2.9	130	150	107.5	2.9	1.6
PE17-074MOC_7	522.0	6.3	0.0306	0.0024	0.0049	0.0001	0.1181	30.5	2.4	31.2	0.8	20	140	31.2	0.8	2.2
PE17-074MOC_8	439.0	7.9	1.7080	0.0320	0.1690	0.0025	0.6146	1009.0	12.0	1006.0	14.0	1011	32	1011.0	32.0	0.5
PE17-074MOC_10	764.0	4.4	0.1737	0.0043	0.0258	0.0003	0.0340	162.3	3.7	164.4	2.1	137	55	164.4	2.1	1.3
PE17-074MOC_11	535.0	24.0	0.0323	0.0023	0.0049	0.0001	0.0634	32.2	2.3	31.5	0.8	80	140	31.5	0.8	2.1
PE17-074MOC_12	286.0	7.0	0.3700	0.0140	0.0499	0.0009	0.1891	320.0	10.0	313.8	5.8	343	80	313.8	5.8	1.9
PE17-074MOC_13	316.9	15.1	1.4510	0.0460	0.1486	0.0030	0.1595	909.0	19.0	893.0	17.0	946	72	946.0	72.0	5.6
PE17-074MOC_14	508.0	3.7	0.2012	0.0088	0.0265	0.0006	0.3356	185.5	7.4	168.6	4.0	384	86	168.6	4.0	9.1
PE17-074MOC_15	140.2	4.6	0.0785	0.0082	0.0120	0.0004	0.0747	75.8	7.6	77.0	2.7	80	170	77.0	2.7	1.6
PE17-074MOC_16	309.0	4.9	0.0332	0.0053	0.0048	0.0003	0.0521	33.1	5.2	30.6	1.8	220	320	30.6	1.8	7.6
PE17-074MOC_17	169.5	15.2	0.0460	0.0110	0.0052	0.0005	0.2051	45.0	11.0	33.7	3.2	510	500	33.7	3.2	25.1
PE17-074MOC_18	257.0	4.6	0.0311	0.0033	0.0045	0.0002	0.0184	30.9	3.3	28.8	1.0	150	200	28.8	1.0	6.8
PE17-074MOC_19	241.0	9.2	0.1211	0.0068	0.0188	0.0004	0.1012	115.3	6.2	119.8	2.3	50	100	119.8	2.3	3.9
PE17-074MOC_21	767.0	4.0	0.1702	0.0048	0.0246	0.0005	0.1160	159.3	4.2	156.5	2.9	239	66	156.5	2.9	1.8
PE17-074MOC_23	357.0	7.9	0.0376	0.0030	0.0053	0.0002	0.2014	37.3	2.9	34.0	1.0	200	140	34.0	1.0	8.8
PE17-074MOC_24	716.0	10.5	0.1685	0.0051	0.0240	0.0004	0.3381	157.8	4.4	152.8	2.7	237	62	152.8	2.7	3.2
PE17-074MOC_25	680.0	6.4	0.0332	0.0021	0.0049	0.0001	0.0329	33.1	2.0	31.4	0.8	190	130	31.4	0.8	5.2
PE17-074MOC_26	2210.0	2.4	0.2084	0.0045	0.0286	0.0005	0.4346	192.0	3.7	181.4	3.0	323	46	181.4	3.0	5.5

PE17-074MOC_27	236.0	20.2	0.0349	0.0054	0.0048	0.0003	0.0379	34.6	5.3	30.7	1.8	210	280	30.7	1.8	11.3
PE17-074MOC_28	310.0	6.0	0.0327	0.0035	0.0051	0.0002	0.0362	32.5	3.4	32.9	1.1	70	190	32.9	1.1	1.2
PE17-074MOC_30	184.0	8.6	1.9210	0.0440	0.1851	0.0031	0.5321	1084.0	15.0	1094.0	17.0	1069	39	1069.0	39.0	2.3
PE17-074MOC_31	488.0	6.3	0.5500	0.0160	0.0683	0.0014	0.3251	444.0	11.0	425.9	8.2	524	65	425.9	8.2	4.1
PE17-074MOC_32	447.0	7.7	0.0980	0.0110	0.0112	0.0006	0.4105	95.0	10.0	72.0	3.7	640	210	72.0	3.7	24.2
PE17-074MOC_33	79.5	12.1	2.3180	0.0650	0.2026	0.0042	0.5032	1211.0	20.0	1188.0	22.0	1247	49	1247.0	49.0	4.7
PE17-074MOC_34	392.0	5.5	0.0315	0.0030	0.0049	0.0002	0.1111	31.3	2.9	31.2	1.1	70	170	31.2	1.1	0.3
PE17-074MOC_35	621.0	7.8	0.1128	0.0052	0.0167	0.0003	0.0768	108.1	4.7	106.7	1.8	136	89	106.7	1.8	1.3
PE17-074MOC_36	406.0	4.5	0.5050	0.0140	0.0641	0.0009	0.2085	415.0	9.3	400.3	5.7	479	60	400.3	5.7	3.5
PE17-074MOC_37	375.7	10.8	0.0851	0.0089	0.0118	0.0005	0.1678	82.5	8.3	75.3	3.0	260	190	75.3	3.0	8.7
PE17-074MOC_37	409.9	4.9	0.2120	0.0100	0.0293	0.0007	0.2426	195.0	8.5	186.4	4.4	310	100	186.4	4.4	4.4
PE17-074MOC_38	508.0	15.9	0.0311	0.0050	0.0048	0.0003	0.0797	31.0	5.0	31.0	2.1	60	330	31.0	2.1	0.0
PE17-074MOC_38	407.0	5.9	0.3500	0.0140	0.0482	0.0011	0.0495	304.0	11.0	303.6	6.7	310	100	303.6	6.7	0.1
PE17-074MOC_39	561.0	5.0	2.7500	0.0420	0.2297	0.0033	0.5120	1340.0	11.0	1332.0	17.0	1351	28	1351.0	28.0	1.4
PE17-074MOC_40	141.7	3.3	0.6070	0.0220	0.0743	0.0011	0.1373	480.0	14.0	461.9	6.4	521	81	461.9	6.4	3.8
PE17-074MOC_41	501.0	4.0	0.0279	0.0034	0.0049	0.0002	0.0752	28.2	3.5	31.5	1.2	150	190	31.5	1.2	11.7
PE17-074MOC_42	250.2	14.0	0.0310	0.0035	0.0049	0.0002	0.0401	30.8	3.5	31.7	1.1	30	190	31.7	1.1	2.9
PE17-074MOC_44	273.0	30.1	0.5620	0.0120	0.0736	0.0009	0.1558	451.6	8.1	457.9	5.6	407	51	457.9	5.6	1.4
PE17-074MOC_45	225.0	4.1	12.2200	0.2600	0.4850	0.0100	0.7489	2616.0	20.0	2544.0	45.0	2675	25	2675.0	25.0	4.9
PE17-074MOC_46	189.4	39.2	0.0402	0.0050	0.0050	0.0002	0.0299	39.6	4.9	31.9	1.2	350	230	31.9	1.2	19.4
PE17-074MOC_47	581.0	6.3	0.0350	0.0100	0.0047	0.0005	0.4962	34.8	9.8	30.4	2.9	260	510	30.4	2.9	12.6
PE17-074MOC_47	1257.0	7.9	0.3038	0.0067	0.0428	0.0007	0.6888	269.0	5.2	270.1	4.1	305	51	270.1	4.1	0.4
PE17-074MOC_48	173.0	25.4	0.0361	0.0060	0.0048	0.0002	0.0935	35.4	5.8	31.0	1.3	40	260	31.0	1.3	12.4
PE17-074MOC_49	189.0	11.3	0.0605	0.0071	0.0085	0.0003	0.2038	58.9	6.7	54.6	2.0	150	200	54.6	2.0	7.3
PE17-074MOC_50	370.0	5.3	0.0312	0.0028	0.0048	0.0001	0.0163	31.1	2.8	31.1	0.9	80	160	31.1	0.9	0.1
PE17-074MOC_51	535.0	6.4	0.0351	0.0028	0.0050	0.0001	0.1479	34.9	2.7	32.2	0.8	170	140	32.2	0.8	7.7
PE17-074MOC_52	600.0	11.6	0.0566	0.0065	0.0085	0.0003	0.0191	55.7	6.3	54.6	2.0	160	240	54.6	2.0	2.0
PE17-074MOC_53	728.0	5.0	0.0308	0.0025	0.0050	0.0001	0.0891	30.7	2.4	31.8	0.9	30	150	31.8	0.9	3.7
PE17-074MOC_54	122.0	6.7	0.2730	0.0160	0.0371	0.0008	0.2531	244.0	13.0	235.0	5.1	310	110	235.0	5.1	3.7
PE17-074MOC_55	234.0	9.0	0.0312	0.0042	0.0047	0.0002	0.0013	30.9	4.1	30.3	1.2	30	220	30.3	1.2	1.9
PE17-074MOC_56	580.0	51.5	0.1829	0.0068	0.0260	0.0005	0.2279	170.0	5.8	165.6	2.8	220	74	165.6	2.8	2.6
PE17-074MOC_57	1469.0	2.4	0.0323	0.0016	0.0050	0.0001	0.0172	32.2	1.6	32.4	0.6	51	96	32.4	0.6	0.5
PE17-074MOC_58	208.1	5.5	0.0325	0.0036	0.0048	0.0002	0.1012	32.2	3.6	30.5	1.2	110	210	30.5	1.2	5.3
PE17-074MOC_59	99.0	12.1	0.1640	0.0130	0.0250	0.0012	0.2986	151.0	11.0	159.2	7.4	80	140	159.2	7.4	5.4
PE17-074MOC_60	199.0	7.1	5.2000	0.1400	0.3269	0.0074	0.5664	1849.0	23.0	1820.0	36.0	1875	42	1875.0	42.0	2.9
PE17-074MOC_61	339.0	5.6	0.2004	0.0094	0.0279	0.0006	0.1365	184.5	7.9	177.4	3.8	253	97	177.4	3.8	3.8
PE17-074MOC_62	68.0	7.0	0.8660	0.0830	0.1021	0.0082	0.2388	627.0	46.0	625.0	48.0	690	260	625.0	48.0	0.3
PE17-074MOC_63	650.0	135.0	0.7990	0.0130	0.0975	0.0009	0.0734	595.3	7.1	599.5	5.4	566	39	599.5	5.4	0.7
PE17-074MOC_64	180.4	6.6	0.0395	0.0048	0.0051	0.0002	0.0632	38.9	4.7	32.7	1.3	260	230	32.7	1.3	15.9
PE17-074MOC_65	1470.0	4.8	0.0725	0.0031	0.0105	0.0002	0.1001	71.0	2.9	67.1	1.1	199	84	67.1	1.1	5.5

PE17-074MOC_66	373.0	12.0	0.3090	0.0130	0.0428	0.0010	0.3022	272.5	9.8	270.1	5.9	284	84	270.1	5.9	0.9
PE17-074MOC_67	102.5	6.2	0.3030	0.0170	0.0417	0.0008	0.0840	266.0	13.0	263.0	5.2	260	110	263.0	5.2	1.1
PE17-074MOC_68	400.0	9.9	1.4590	0.0270	0.1512	0.0020	0.3995	911.0	11.0	907.0	11.0	919	37	919.0	37.0	1.3
PE17-074MOC_69	1680.0	4.4	0.0726	0.0026	0.0110	0.0002	0.3351	71.1	2.5	70.3	1.4	106	68	70.3	1.4	1.1
PE17-074MOC_70	1361.0	3.7	0.0869	0.0045	0.0116	0.0003	0.1397	84.4	4.2	74.6	1.8	350	110	74.6	1.8	11.6
PE17-074MOC_72	242.1	3.1	0.0715	0.0053	0.0100	0.0003	0.0993	70.2	5.1	63.8	1.6	240	140	63.8	1.6	9.1
PE17-074MOC_73	1250.0	3.8	0.4155	0.0092	0.0431	0.0009	0.3558	352.4	6.6	271.6	5.6	926	53	271.6	5.6	22.9
PE17-074MOC_75	376.0	6.8	0.2310	0.0093	0.0311	0.0004	0.1497	210.0	7.6	197.7	2.8	322	80	197.7	2.8	5.9
PE17-074MOC_77	463.0	15.2	0.0305	0.0050	0.0047	0.0003	0.1065	30.4	5.0	30.4	1.9	40	310	30.4	1.9	0.0
PE17-074MOC_77	218.3	18.9	0.1810	0.0130	0.0248	0.0008	0.1907	168.0	11.0	158.2	4.8	300	150	158.2	4.8	5.8
PE17-074MOC_78	706.0	21.1	2.3440	0.0420	0.2071	0.0034	0.5545	1224.0	13.0	1213.0	18.0	1242	32	1242.0	32.0	2.3
PE17-074MOC_80	564.4	6.2	0.0306	0.0024	0.0049	0.0001	0.1210	30.5	2.3	31.8	0.8	20	130	31.8	0.8	4.2
PE17-074MOC_81	643.0	5.1	0.0318	0.0027	0.0048	0.0001	0.0070	31.9	2.7	31.0	0.9	70	150	31.0	0.9	2.7
PE17-074MOC_82	593.0	7.7	0.0308	0.0041	0.0050	0.0002	0.2053	30.7	4.0	31.9	1.6	30	220	31.9	1.6	3.9
PE17-074MOC_83	286.0	8.3	0.1160	0.0075	0.0170	0.0004	0.0821	111.6	7.0	108.9	2.5	160	120	108.9	2.5	2.4
PE17-074MOC_84	741.0	3.9	0.0291	0.0020	0.0047	0.0001	0.0749	29.0	2.0	30.2	0.7	20	130	30.2	0.7	4.1
PE17-074MOC_85	115.6	10.0	1.6360	0.0400	0.1634	0.0024	0.3758	982.0	16.0	975.0	14.0	985	49	985.0	49.0	1.0
PE17-074MOC_86	153.3	10.5	1.5360	0.0410	0.1564	0.0034	0.4564	940.0	16.0	936.0	19.0	939	53	939.0	53.0	0.3
PE17-074MOC_87	175.3	3.7	0.0666	0.0066	0.0094	0.0003	0.1132	64.8	6.3	60.1	2.2	180	170	60.1	2.2	7.3
PE17-074MOC_88	184.1	5.9	1.7500	0.0380	0.1666	0.0028	0.4387	1024.0	14.0	993.0	15.0	1086	42	1086.0	42.0	8.6
PE17-074MOC_89	76.1	18.2	0.6410	0.0400	0.0801	0.0023	0.3056	496.0	24.0	496.0	14.0	470	120	496.0	14.0	0.0
PE17-074MOC_90	339.9	6.4	0.0346	0.0034	0.0052	0.0002	0.0555	34.3	3.3	33.2	1.0	110	170	33.2	1.0	3.2
PE17-074MOC_91	129.7	11.2	0.1880	0.0130	0.0262	0.0009	0.1697	173.0	11.0	166.4	5.4	240	130	166.4	5.4	3.8
PE17-074MOC_92	727.0	35.3	1.1830	0.0240	0.1328	0.0026	0.5964	791.0	11.0	804.0	15.0	752	38	804.0	15.0	1.6
PE17-074MOC_93	323.0	5.5	0.0324	0.0034	0.0047	0.0002	0.1606	32.2	3.4	30.1	1.0	110	180	30.1	1.0	6.6
PE17-074MOC_94	259.4	8.4	0.7610	0.0190	0.0900	0.0013	0.3471	572.0	11.0	555.5	7.8	620	53	555.5	7.8	2.9
PE17-074MOC_95	422.0	16.9	0.9240	0.0180	0.1095	0.0015	0.4209	662.7	9.4	669.4	9.0	631	41	669.4	9.0	1.0
PE17-074MOC_96	155.7	8.0	0.0285	0.0047	0.0044	0.0002	0.0006	28.3	4.6	28.4	1.3	50	260	28.4	1.3	0.4
PE17-074MOC_97	436.0	5.4	0.0761	0.0043	0.0113	0.0002	0.0897	74.7	4.2	72.5	1.5	150	110	72.5	1.5	2.9
PE17-074MOC_98	511.0	4.3	0.1835	0.0088	0.0264	0.0010	0.3989	170.4	7.5	168.2	6.3	208	95	168.2	6.3	1.3
PE17-074MOC_99	212.0	7.1	1.9260	0.0410	0.1808	0.0035	0.5170	1087.0	14.0	1070.0	19.0	1108	40	1108.0	40.0	3.4
PE17-074MOC_100	540.0	11.1	1.1400	0.0290	0.1271	0.0032	0.4733	771.0	14.0	771.0	18.0	775	51	771.0	18.0	0.0
PE17-074MOC_101	403.0	22.5	5.1800	0.1100	0.3405	0.0062	0.7466	1844.0	18.0	1887.0	30.0	1797	27	1797.0	27.0	5.0
PE17-074MOC_102	671.0	4.6	0.0324	0.0023	0.0050	0.0001	0.1549	32.3	2.3	32.3	0.8	50	130	32.3	0.8	0.1
PE17-074MOC_103	33.5	6.0	4.1400	0.2100	0.2650	0.0100	0.6848	1643.0	42.0	1520.0	53.0	1800	74	1800.0	74.0	15.6
PE17-074MOC_104	290.1	10.5	0.0820	0.0054	0.0124	0.0003	0.0146	79.5	5.1	79.3	1.6	80	120	79.3	1.6	0.3
PE17-074MOC_105	231.0	15.6	0.1740	0.0250	0.0240	0.0016	0.4238	168.0	25.0	153.0	10.0	330	280	153.0	10.0	8.9
PE17-074MOC_105	571.0	6.5	0.3710	0.0140	0.0511	0.0008	0.1823	320.0	10.0	321.2	5.1	300	80	321.2	5.1	0.4
PE17-074MOC_106	227.0	9.9	0.1083	0.0068	0.0165	0.0004	0.1795	103.7	6.1	105.4	2.4	90	110	105.4	2.4	1.6
PE17-074MOC_107	179.7	7.8	0.7400	0.0220	0.0919	0.0018	0.3202	561.0	13.0	566.0	11.0	516	64	566.0	11.0	0.9

PE17-074MOC_109	422.7	8.2	0.0341	0.0028	0.0048	0.0001	0.1183	33.9	2.7	30.9	0.9	200	150	30.9	0.9	8.8
PE17-074MOC_110	508.0	9.5	0.0292	0.0024	0.0050	0.0002	0.0509	29.4	2.4	32.2	1.4	70	140	32.2	1.4	9.5
PE17-074MOC_111	121.5	15.0	0.0295	0.0057	0.0050	0.0002	0.0511	29.7	5.7	31.9	1.6	250	260	31.9	1.6	7.4
PE17-074MOC_112	365.0	9.0	0.0507	0.0043	0.0073	0.0002	0.1968	49.9	4.1	46.7	1.4	160	140	46.7	1.4	6.4
PE17-074MOC_113	267.0	8.2	0.0330	0.0038	0.0050	0.0002	0.1806	32.7	3.7	32.0	1.3	60	190	32.0	1.3	2.1
PE17-074MOC_114	520.0	6.3	0.0308	0.0023	0.0049	0.0001	0.0747	30.7	2.3	31.6	0.9	50	140	31.6	0.9	2.9
PE17-074MOC_115	753.0	6.0	0.0336	0.0023	0.0051	0.0001	0.2607	33.4	2.3	32.7	0.9	90	120	32.7	0.9	2.0
PE17-074MOC_116	356.0	17.7	0.8960	0.0200	0.1049	0.0016	0.3151	647.0	11.0	642.7	9.3	651	50	642.7	9.3	0.7
PE17-074MOC_117	571.0	13.5	2.1500	0.0380	0.1972	0.0028	0.6932	1164.0	12.0	1159.0	15.0	1169	26	1169.0	26.0	0.9
PE17-074MOC_118	445.0	5.9	0.0314	0.0027	0.0049	0.0001	0.0544	31.3	2.7	31.2	0.9	70	160	31.2	0.9	0.2
PE17-074MOC_119	97.1	7.4	0.0364	0.0088	0.0047	0.0004	0.1215	35.6	8.6	30.3	2.4	140	420	30.3	2.4	14.9
PE17-074MOC_120	260.0	54.0	1.7690	0.0580	0.1609	0.0046	0.5410	1027.0	21.0	960.0	26.0	1173	62	1173.0	62.0	18.2
PE17-074MOC_121	418.0	3.8	0.0581	0.0041	0.0085	0.0002	0.1329	57.0	3.9	54.7	1.5	150	130	54.7	1.5	4.0
PE17-074MOC_122	1256.0	2.9	0.0856	0.0043	0.0123	0.0004	0.0780	83.3	4.0	78.8	2.3	210	110	78.8	2.3	5.4
PE17-074MOC_123	620.0	10.4	0.1176	0.0076	0.0178	0.0003	0.0782	112.0	6.8	113.6	2.0	80	120	113.6	2.0	1.4
PE17-074MOC_124	244.0	4.6	0.0796	0.0075	0.0101	0.0008	0.2537	77.0	7.0	64.5	4.8	500	190	64.5	4.8	16.2
PE17-074MOC_125	176.8	8.6	6.1800	0.1100	0.3655	0.0059	0.7274	1999.0	15.0	2006.0	28.0	1989	23	1989.0	23.0	0.9
PE17-074MOC_126	504.0	6.0	0.9480	0.0230	0.1018	0.0015	0.5049	675.0	12.0	624.6	8.8	840	43	624.6	8.8	7.5
PE17-074MOC_127	199.6	28.4	0.0327	0.0044	0.0049	0.0002	0.1246	32.3	4.3	31.7	1.2	30	220	31.7	1.2	1.9
PE17-074MOC_129	415.0	9.5	0.0323	0.0027	0.0048	0.0001	0.0351	32.1	2.6	31.0	0.9	100	150	31.0	0.9	3.6
PE17-074MOC_130	90.0	6.2	0.7920	0.0400	0.0912	0.0029	0.4741	590.0	23.0	562.0	17.0	640	110	562.0	17.0	4.7
PE17-074MOC_131	118.7	6.2	1.9160	0.0930	0.1816	0.0079	0.3965	1068.0	31.0	1070.0	43.0	1102	95	1102.0	95.0	2.9
PE17-074MOC_132	306.0	9.3	0.5140	0.0390	0.0674	0.0042	0.4401	417.0	26.0	420.0	25.0	410	150	420.0	25.0	0.7
PE17-074MOC_133	1340.0	7.7	0.1807	0.0043	0.0264	0.0004	0.2807	168.4	3.7	168.0	2.2	181	53	168.0	2.2	0.2
PE17-074MOC_134	946.0	4.9	0.0717	0.0031	0.0107	0.0003	0.4187	70.2	2.9	68.7	2.2	173	84	68.7	2.2	2.1
PE17-074MOC_135	201.3	13.5	7.3100	0.1000	0.3730	0.0045	0.5222	2147.0	13.0	2042.0	21.0	2241	23	2241.0	23.0	8.9

Analysis	U (ppm)	U/Th	207Pb/ 235U	±	206Pb/ 238U	±	err. corr.	207Pb/ 235U Age (Ma)	± (Ma)	206Pb/ 238U Age (Ma)	± (Ma)	207Pb/ 206Pb Age (Ma)	± (Ma)	Best age (Ma)	± (Ma)	Disc (%)
PE17-081MOC: 17°23.71'S, 071°00.71'W																
PE17-081MOC_1	561.0	2.63	0.0243	0.0023	0.0036	0.0001	0.0221	24.3	2.3	23.4	0.7	60	150	23.4	0.7	3.9
PE17-081MOC_2	299.3	3.04	0.0214	0.0029	0.0038	0.0002	0.1058	21.3	2.9	24.2	1.0	190	200	24.2	1.0	13.5
PE17-081MOC_4	242.0	16.04	14.2000	0.1300	0.5423	0.0049	0.6086	2761.6	8.7	2792.0	20.0	2738	13	2738.0	13.0	2.0
PE17-081MOC_5	225.8	1.84	0.0280	0.0063	0.0036	0.0003	0.1859	27.8	6.2	23.0	1.7	300	420	23.0	1.7	17.3
PE17-081MOC_6	168.0	2.89	0.0279	0.0053	0.0036	0.0002	0.1215	27.4	5.1	23.2	1.1	10	300	23.2	1.1	15.3
PE17-081MOC_7	163.2	1.50	0.0253	0.0042	0.0034	0.0002	0.1021	25.2	4.1	21.7	1.1	140	290	21.7	1.1	13.9
PE17-081MOC_8	195.2	2.89	0.0281	0.0041	0.0038	0.0002	0.0239	28.0	4.0	24.2	1.3	260	260	24.2	1.3	13.6
PE17-081MOC_9	426.0	5.35	0.0771	0.0045	0.0114	0.0002	0.0324	75.1	4.2	72.8	1.2	160	110	72.8	1.2	3.1
PE17-081MOC_10	164.0	3.36	0.0274	0.0045	0.0039	0.0002	0.1419	27.1	4.4	25.0	1.2	30	260	25.0	1.2	7.7
PE17-081MOC_11	436.0	2.48	0.0869	0.0059	0.0125	0.0004	0.0641	84.3	5.5	80.2	2.2	220	140	80.2	2.2	4.9
PE17-081MOC_13	302.0	23.00	0.5420	0.0190	0.0699	0.0011	0.0464	438.0	12.0	435.4	6.7	426	81	435.4	6.7	0.6
PE17-081MOC_14	594.0	6.02	0.0330	0.0025	0.0048	0.0001	0.2117	32.9	2.4	30.8	0.6	150	130	30.8	0.6	6.4
PE17-081MOC_15	500.0	7.83	0.0859	0.0041	0.0115	0.0002	0.0597	83.4	3.8	73.8	1.4	330	100	73.8	1.4	11.5
PE17-081MOC_16	1195.0	9.40	0.0769	0.0023	0.0115	0.0001	0.1274	75.2	2.2	73.6	0.9	137	62	73.6	0.9	2.1
PE17-081MOC_17	104.3	4.38	0.1040	0.0140	0.0123	0.0006	0.1044	98.0	13.0	78.5	3.6	510	260	78.5	3.6	19.9
PE17-081MOC_19	276.0	6.30	0.0814	0.0058	0.0116	0.0003	0.0116	79.6	5.5	74.3	1.8	210	130	74.3	1.8	6.7
PE17-081MOC_20	20.9	4.10	1.3500	0.1100	0.1405	0.0096	0.2769	850.0	47.0	844.0	54.0	860	170	844.0	54.0	0.7
PE17-081MOC_21	734.0	6.06	0.0759	0.0033	0.0113	0.0002	0.1760	74.1	3.1	72.6	1.2	176	88	72.6	1.2	2.0
PE17-081MOC_22	151.8	5.79	0.0836	0.0099	0.0130	0.0006	0.0270	81.0	9.4	83.1	3.5	100	230	83.1	3.5	2.6
PE17-081MOC_23	223.2	3.63	0.0318	0.0040	0.0044	0.0002	0.0042	31.6	3.9	28.2	1.1	210	230	28.2	1.1	10.8
PE17-081MOC_24	389.0	5.15	0.8510	0.0210	0.0968	0.0015	0.2687	623.0	12.0	595.5	8.7	726	52	595.5	8.7	4.4
PE17-081MOC_25	101.4	7.37	0.0567	0.0081	0.0085	0.0004	0.2556	54.9	7.6	54.3	2.5	50	220	54.3	2.5	1.1
PE17-081MOC_26	719.0	5.70	0.0806	0.0039	0.0119	0.0002	0.1200	78.6	3.6	76.4	1.5	170	100	76.4	1.5	2.8
PE17-081MOC_27	1017.0	7.58	0.0762	0.0032	0.0110	0.0002	0.1700	74.5	3.0	70.6	1.0	196	82	70.6	1.0	5.2
PE17-081MOC_28	427.0	3.57	0.0236	0.0026	0.0039	0.0001	0.1786	23.6	2.6	24.8	0.9	40	180	24.8	0.9	5.3
PE17-081MOC_29	237.0	4.12	0.0750	0.0100	0.0111	0.0005	0.1553	73.2	9.7	70.9	3.4	180	250	70.9	3.4	3.1
PE17-081MOC_30	353.0	3.10	0.0714	0.0057	0.0106	0.0003	0.0052	69.7	5.4	68.0	2.0	160	160	68.0	2.0	2.4
PE17-081MOC_31	136.7	2.28	0.0274	0.0081	0.0038	0.0004	0.0200	27.1	7.9	24.2	2.2	180	510	24.2	2.2	10.7
PE17-081MOC_32	288.6	1.88	0.0240	0.0037	0.0037	0.0002	0.1940	24.0	3.6	23.8	1.2	10	240	23.8	1.2	0.8
PE17-081MOC_33	174.2	2.79	0.0233	0.0036	0.0034	0.0002	0.0137	23.2	3.5	22.1	1.1	40	240	22.1	1.1	4.7
PE17-081MOC_34	187.5	2.80	0.0315	0.0094	0.0038	0.0003	0.1980	31.1	9.1	24.3	1.9	250	500	24.3	1.9	21.9
PE17-081MOC_35	404.0	2.61	0.0218	0.0024	0.0037	0.0001	0.0420	21.8	2.4	23.6	0.8	110	170	23.6	0.8	8.3
PE17-081MOC_36	94.3	4.64	0.7360	0.0410	0.0902	0.0021	0.1944	555.0	24.0	557.0	13.0	550	120	557.0	13.0	0.4
PE17-081MOC_37	168.0	2.52	0.0258	0.0049	0.0036	0.0002	0.0457	25.5	4.8	22.9	1.3	60	340	22.9	1.3	10.2
PE17-081MOC_38	123.0	4.60	0.0628	0.0072	0.0094	0.0003	0.0080	61.0	6.8	60.4	2.1	70	200	60.4	2.1	1.0

PE17-081MOC_39	1054.0	5.68	0.0771	0.0029	0.0115	0.0002	0.0929	75.3	2.7	73.6	1.1	161	78	73.6	1.1	2.3
PE17-081MOC_40	220.3	1.91	0.0296	0.0052	0.0040	0.0002	0.1375	29.4	5.1	25.9	1.3	150	300	25.9	1.3	11.9
PE17-081MOC_41	539.0	9.08	0.0748	0.0041	0.0114	0.0002	0.2045	73.5	4.0	73.1	1.3	120	110	73.1	1.3	0.5
PE17-081MOC_44	424.0	2.14	0.0260	0.0027	0.0039	0.0001	0.2000	26.0	2.6	24.9	0.9	80	170	24.9	0.9	4.4
PE17-081MOC_46	170.4	1.94	0.0294	0.0071	0.0041	0.0003	0.1492	29.1	6.9	26.3	2.2	110	440	26.3	2.2	9.6
PE17-081MOC_47	201.8	5.33	0.0809	0.0070	0.0116	0.0004	0.1645	78.5	6.6	74.5	2.4	210	180	74.5	2.4	5.1
PE17-081MOC_48	288.0	4.22	0.0332	0.0038	0.0049	0.0002	0.2027	32.9	3.7	31.2	1.0	130	190	31.2	1.0	5.2
PE17-081MOC_49	96.6	1.76	0.0275	0.0056	0.0037	0.0002	0.0134	27.7	5.7	24.0	1.4	20	330	24.0	1.4	13.4
PE17-081MOC_50	648.0	7.51	0.0805	0.0031	0.0121	0.0002	0.1135	78.8	3.0	77.5	1.3	128	78	77.5	1.3	1.6
PE17-081MOC_54	118.5	1.61	0.0208	0.0057	0.0033	0.0002	0.1011	20.5	5.6	21.3	1.4	240	380	21.3	1.4	3.9
PE17-081MOC_56	208.0	6.24	0.0670	0.0085	0.0097	0.0004	0.2139	65.4	8.0	62.0	2.4	210	240	62.0	2.4	5.2
PE17-081MOC_57	534.0	2.82	0.0235	0.0024	0.0035	0.0001	0.0802	23.5	2.4	22.3	0.8	130	190	22.3	0.8	5.2
PE17-081MOC_58	150.5	6.36	0.0799	0.0091	0.0092	0.0004	0.0716	77.3	8.5	59.3	2.5	560	240	59.3	2.5	23.3
PE17-081MOC_59	310.0	2.43	0.0297	0.0068	0.0038	0.0003	0.0457	29.5	6.7	24.4	1.9	300	420	24.4	1.9	17.3
PE17-081MOC_60	257.5	3.17	0.0242	0.0065	0.0039	0.0002	0.0567	24.0	6.4	24.8	1.4	100	390	24.8	1.4	3.3
PE17-081MOC_61	351.0	2.45	0.0265	0.0029	0.0038	0.0002	0.1601	26.4	2.9	24.2	1.0	150	190	24.2	1.0	8.3
PE17-081MOC_62	562.0	4.05	0.0809	0.0039	0.0120	0.0002	0.1595	78.8	3.6	76.9	1.6	132	94	76.9	1.6	2.4
PE17-081MOC_63	420.0	2.26	0.0286	0.0036	0.0040	0.0001	0.0350	27.5	2.9	25.6	0.8	140	190	25.6	0.8	7.1
PE17-081MOC_64	208.0	3.26	0.0260	0.0050	0.0040	0.0002	0.1096	26.8	5.2	26.0	1.4	10	300	26.0	1.4	3.0
PE17-081MOC_65	187.0	2.01	0.0320	0.0110	0.0041	0.0003	0.0405	31.0	10.0	26.3	2.1	50	490	26.3	2.1	15.2
PE17-081MOC_66	206.0	2.04	0.0285	0.0039	0.0040	0.0002	0.0500	28.8	3.9	25.9	1.0	140	220	25.9	1.0	10.1
PE17-081MOC_67	225.0	3.89	0.0236	0.0037	0.0034	0.0001	0.0913	23.4	3.7	21.9	0.9	10	250	21.9	0.9	6.4
PE17-081MOC_69	86.1	4.35	3.6310	0.0720	0.2784	0.0040	0.4142	1552.0	16.0	1582.0	20.0	1501	37	1501.0	37.0	5.4
PE17-081MOC_72	980.0	3.54	0.0751	0.0025	0.0115	0.0002	0.0084	73.4	2.3	74.0	1.0	84	69	74.0	1.0	0.8
PE17-081MOC_73	444.0	1.96	0.0251	0.0020	0.0037	0.0001	0.0766	25.1	2.0	23.5	0.7	180	160	23.5	0.7	6.5
PE17-081MOC_74	330.0	3.09	0.0264	0.0028	0.0038	0.0001	0.0281	26.3	2.7	24.5	0.8	120	190	24.5	0.8	6.9
PE17-081MOC_75	78.3	3.21	2.4340	0.0630	0.2208	0.0033	0.3639	1247.0	19.0	1285.0	18.0	1175	50	1175.0	50.0	9.4
PE17-081MOC_76	178.1	3.11	0.0241	0.0041	0.0035	0.0002	0.0154	23.9	4.0	22.5	1.0	20	260	22.5	1.0	5.9
PE17-081MOC_77	550.0	3.62	0.0828	0.0041	0.0124	0.0002	0.1342	80.6	3.9	79.6	1.5	123	98	79.6	1.5	1.2
PE17-081MOC_78	1400.0	1.52	0.0258	0.0017	0.0039	0.0001	0.1704	25.8	1.7	25.2	0.8	110	120	25.2	0.8	2.4
PE17-081MOC_79	1620.0	1.55	0.0287	0.0013	0.0040	0.0001	0.0757	28.7	1.3	25.7	0.5	281	99	25.7	0.5	10.4
PE17-081MOC_80	166.0	2.09	0.0276	0.0047	0.0035	0.0002	0.1691	27.3	4.5	22.7	1.1	200	270	22.7	1.1	16.8
PE17-081MOC_81	366.0	6.46	0.0867	0.0078	0.0119	0.0003	0.0509	84.1	7.2	76.2	2.1	250	180	76.2	2.1	9.4
PE17-081MOC_82	394.0	2.81	0.0280	0.0027	0.0041	0.0001	0.0017	27.9	2.7	26.1	0.9	140	170	26.1	0.9	6.4
PE17-081MOC_83	476.0	2.07	0.0231	0.0022	0.0036	0.0001	0.0736	23.1	2.2	23.3	0.6	20	160	23.3	0.6	0.7
PE17-081MOC_84	218.0	7.37	1.6040	0.0300	0.1615	0.0022	0.4285	971.0	12.0	965.0	12.0	979	38	979.0	38.0	1.4
PE17-081MOC_85	136.1	2.77	0.0310	0.0053	0.0041	0.0002	0.0274	30.6	5.2	26.1	1.3	140	280	26.1	1.3	14.7
PE17-081MOC_86	595.0	2.76	0.0283	0.0023	0.0037	0.0001	0.1368	28.2	2.2	23.9	0.7	320	150	23.9	0.7	15.2
PE17-081MOC_88	439.0	2.19	0.0239	0.0026	0.0037	0.0001	0.1528	23.9	2.6	24.1	0.8	30	190	24.1	0.8	0.6
PE17-081MOC_89	479.0	5.86	0.0804	0.0048	0.0118	0.0002	0.1016	78.3	4.5	75.8	1.5	180	120	75.8	1.5	3.2

PE17-081MOC_90	405.0	2.77	0.0885	0.0050	0.0124	0.0003	0.2904	85.8	4.7	79.1	1.7	250	110	79.1	1.7	7.8
PE17-081MOC_91	130.5	1.41	0.0251	0.0054	0.0038	0.0002	0.0995	24.8	5.3	24.4	1.5	80	330	24.4	1.5	1.6
PE17-081MOC_92	301.0	5.04	0.0777	0.0053	0.0115	0.0003	0.2214	75.5	5.0	73.8	1.7	120	120	73.8	1.7	2.3
PE17-081MOC_94	103.4	3.14	1.0950	0.0400	0.1138	0.0025	0.2480	746.0	20.0	694.0	15.0	876	80	694.0	15.0	7.0
PE17-081MOC_95	8250.0	6.51	0.0228	0.0006	0.0035	0.0001	0.3119	22.9	0.6	22.5	0.5	104	57	22.5	0.5	1.4
PE17-081MOC_96	344.0	3.72	0.0775	0.0049	0.0118	0.0003	0.0303	75.4	4.6	75.5	1.7	100	120	75.5	1.7	0.1
PE17-081MOC_97	787.0	5.37	0.0812	0.0033	0.0121	0.0002	0.1394	79.1	3.1	77.4	1.5	150	83	77.4	1.5	2.1
PE17-081MOC_99	291.0	2.55	0.0256	0.0030	0.0038	0.0002	0.0538	25.5	2.9	24.7	1.1	110	210	24.7	1.1	3.1
PE17-081MOC_100	651.0	5.36	0.0831	0.0036	0.0119	0.0002	0.1759	80.8	3.4	76.1	1.2	219	95	76.1	1.2	5.8
PE17-081MOC_101	443.0	2.68	0.0244	0.0030	0.0037	0.0002	0.3293	24.4	3.0	24.0	0.9	60	200	24.0	0.9	1.5
PE17-081MOC_102	860.0	3.08	0.0757	0.0030	0.0113	0.0002	0.1715	74.3	2.9	72.6	1.1	142	80	72.6	1.1	2.3
PE17-081MOC_104	820.0	4.72	0.0756	0.0030	0.0115	0.0002	0.1166	73.9	2.8	73.5	1.2	125	80	73.5	1.2	0.5
PE17-081MOC_105	1164.0	4.58	0.0758	0.0025	0.0113	0.0002	0.1325	74.1	2.4	72.7	1.1	131	68	72.7	1.1	1.9
PE17-081MOC_106	268.5	2.22	0.0375	0.0046	0.0041	0.0002	0.0848	37.2	4.5	26.3	1.3	630	240	26.3	1.3	29.3
PE17-081MOC_107	67.7	2.78	0.0197	0.0060	0.0035	0.0003	0.0276	20.0	6.1	22.5	1.8	450	420	22.5	1.8	12.5
PE17-081MOC_108	638.0	2.43	0.0693	0.0041	0.0106	0.0003	0.2142	67.9	3.9	68.0	1.8	100	110	68.0	1.8	0.1
PE17-081MOC_110	537.0	2.96	0.0769	0.0038	0.0111	0.0002	0.0913	75.0	3.6	71.1	1.3	210	100	71.1	1.3	5.2
PE17-081MOC_112	436.0	4.29	0.1142	0.0050	0.0128	0.0003	0.0025	109.4	4.6	81.8	1.6	710	100	81.8	1.6	25.2
PE17-081MOC_113	317.0	2.86	0.0710	0.0048	0.0110	0.0003	0.1604	69.3	4.5	70.6	1.6	40	120	70.6	1.6	1.9
PE17-081MOC_114	291.0	2.72	0.0256	0.0032	0.0033	0.0001	0.0360	25.6	3.2	21.5	0.8	270	230	21.5	0.8	16.0
PE17-081MOC_115	147.0	2.00	0.0280	0.0059	0.0037	0.0002	0.0738	28.3	6.0	23.7	1.4	70	330	23.7	1.4	16.3
PE17-081MOC_116	1461.0	1.81	0.0757	0.0021	0.0113	0.0002	0.2673	74.0	1.9	72.4	0.9	135	55	72.4	0.9	2.2
PE17-081MOC_117	563.0	6.98	0.0970	0.0054	0.0117	0.0004	0.1717	93.7	5.0	74.9	2.2	530	120	74.9	2.2	20.1
PE17-081MOC_118	340.3	2.10	0.0261	0.0027	0.0038	0.0001	0.0778	26.1	2.6	24.6	0.8	120	180	24.6	0.8	5.9
PE17-081MOC_119	863.0	5.21	0.0805	0.0026	0.0120	0.0002	0.1102	78.5	2.4	76.9	1.1	134	66	76.9	1.1	2.0
PE17-081MOC_120	258.0	4.15	0.0768	0.0097	0.0115	0.0005	0.2824	74.7	9.1	73.6	3.1	120	230	73.6	3.1	1.5
PE17-081MOC_121	219.1	2.83	0.0275	0.0033	0.0039	0.0002	0.0929	27.4	3.2	25.3	1.0	180	210	25.3	1.0	7.7
PE17-081MOC_123	381.0	3.47	0.0762	0.0039	0.0112	0.0002	0.1273	74.3	3.6	71.7	1.3	149	96	71.7	1.3	3.5
PE17-081MOC_124	748.0	7.35	0.0235	0.0031	0.0034	0.0001	0.0873	23.5	3.1	22.1	0.8	70	210	22.1	0.8	6.0
PE17-081MOC_125	273.8	3.61	0.0910	0.0077	0.0115	0.0003	0.0755	88.0	7.2	73.7	2.1	420	180	73.7	2.1	16.3
PE17-081MOC_126	173.0	2.56	0.0339	0.0070	0.0038	0.0003	0.0777	33.4	6.8	24.5	1.6	270	350	24.5	1.6	26.6
PE17-081MOC_127	420.0	2.28	0.0227	0.0019	0.0038	0.0001	0.0272	22.8	1.9	24.5	0.7	80	140	24.5	0.7	7.3
PE17-081MOC_129	723.0	3.52	0.0793	0.0031	0.0118	0.0002	0.0288	77.4	2.9	75.7	1.1	132	80	75.7	1.1	2.2
PE17-081MOC_130	1380.0	5.28	0.0809	0.0040	0.0118	0.0002	0.2718	78.7	3.8	75.9	1.5	160	90	75.9	1.5	3.6
PE17-081MOC_131	198.5	1.44	0.0262	0.0058	0.0035	0.0002	0.1492	26.0	5.7	22.8	1.2	130	390	22.8	1.2	12.3
PE17-081MOC_133	372.3	3.71	0.0714	0.0055	0.0107	0.0003	0.0702	69.7	5.2	68.7	2.0	120	150	68.7	2.0	1.4
PE17-081MOC_134	239.0	3.85	0.0750	0.0056	0.0105	0.0003	0.0716	73.6	5.4	67.3	1.8	250	140	67.3	1.8	8.6
PE17-081MOC_135	159.1	3.91	0.0580	0.0089	0.0091	0.0005	0.0195	56.7	8.5	58.7	3.0	30	270	58.7	3.0	3.5

Analysis	U (ppm)	U/Th	207Pb/ 235U	±	206Pb/ 238U	±	err. corr.	207Pb/ 235U Age (Ma)	± (Ma)	206Pb/ 238U Age (Ma)	± (Ma)	207Pb/ 206Pb Age (Ma)	± (Ma)	Best age (Ma)	± (Ma)	Disc (%)
PE17-086MOC: 17°23.68'S, 071°00.75'W																
PE17-086MOC_1	186.4	3.59	0.0317	0.0049	0.0041	0.0002	0.1674	31.4	4.8	26.3	1.2	220	260	26.3	1.2	16.2
PE17-086MOC_2	154.1	2.82	0.0297	0.0057	0.0036	0.0002	0.0233	29.4	5.6	22.9	1.4	240	340	22.9	1.4	22.1
PE17-086MOC_4	255.2	3.63	0.0301	0.0053	0.0039	0.0002	0.1293	29.9	5.1	25.4	1.4	250	310	25.4	1.4	15.1
PE17-086MOC_7	337.0	3.72	0.0263	0.0033	0.0035	0.0002	0.0539	26.2	3.3	22.7	1.0	200	230	22.7	1.0	13.2
PE17-086MOC_8	302.0	3.62	0.0260	0.0028	0.0037	0.0001	0.0164	25.9	2.8	24.1	0.8	160	190	24.1	0.8	7.0
PE17-086MOC_9	183.4	16.08	2.2450	0.0490	0.1956	0.0032	0.3810	1191.0	15.0	1151.0	17.0	1244	45	1244.0	45.0	7.5
PE17-086MOC_10	484.0	3.60	0.0242	0.0020	0.0039	0.0001	0.0739	24.2	2.0	24.8	0.8	0	150	24.8	0.8	2.3
PE17-086MOC_14	949.0	9.13	0.0816	0.0027	0.0122	0.0002	0.0909	79.5	2.5	78.2	1.3	127	68	78.2	1.3	1.6
PE17-086MOC_15	222.1	15.59	1.7280	0.0340	0.1747	0.0022	0.3662	1016.0	13.0	1038.0	12.0	958	38	958.0	38.0	8.4
PE17-086MOC_16	572.0	8.97	0.0812	0.0041	0.0122	0.0003	0.1056	79.1	3.8	78.2	1.6	120	100	78.2	1.6	1.1
PE17-086MOC_17	124.0	2.52	0.0236	0.0064	0.0039	0.0003	0.0385	23.3	6.2	24.9	1.9	150	410	24.9	1.9	6.9
PE17-086MOC_19	363.0	8.09	0.0910	0.0051	0.0112	0.0002	0.0449	88.0	4.8	71.6	1.4	480	120	71.6	1.4	18.6
PE17-086MOC_20	382.0	4.74	0.0248	0.0026	0.0038	0.0001	0.0715	24.7	2.5	24.7	0.9	80	180	24.7	0.9	0.2
PE17-086MOC_21	660.0	2.99	0.0247	0.0018	0.0037	0.0001	0.0380	24.7	1.8	23.9	0.6	100	140	23.9	0.6	3.4
PE17-086MOC_22	124.7	3.29	0.0308	0.0089	0.0038	0.0003	0.1594	30.3	8.7	24.4	2.0	250	490	24.4	2.0	19.5
PE17-086MOC_23	118.1	3.83	0.0256	0.0058	0.0035	0.0002	0.1392	25.2	5.7	22.4	1.4	10	370	22.4	1.4	11.1
PE17-086MOC_24	103.0	12.87	4.9300	0.1300	0.3345	0.0068	0.6440	1802.0	22.0	1862.0	34.0	1731	37	1731.0	37.0	7.6
PE17-086MOC_25	153.0	3.30	0.0277	0.0054	0.0039	0.0002	0.0102	27.4	5.2	24.9	1.5	40	320	24.9	1.5	9.1
PE17-086MOC_26	120.4	3.60	0.0285	0.0057	0.0037	0.0002	0.1011	28.2	5.6	24.0	1.5	70	330	24.0	1.5	14.9
PE17-086MOC_27	71.1	4.49	0.0269	0.0070	0.0040	0.0003	0.0889	26.1	6.8	26.0	1.7	360	400	26.0	1.7	0.4
PE17-086MOC_28	164.0	9.61	0.0809	0.0083	0.0105	0.0004	0.0246	78.1	7.8	67.0	2.7	340	200	67.0	2.7	14.2
PE17-086MOC_29	254.0	2.55	0.0257	0.0038	0.0036	0.0002	0.0845	25.5	3.7	23.0	1.2	140	270	23.0	1.2	9.8
PE17-086MOC_31	249.8	7.29	2.1060	0.0460	0.1961	0.0047	0.5817	1154.0	15.0	1153.0	26.0	1150	40	1150.0	40.0	0.3
PE17-086MOC_32	375.0	13.22	1.8240	0.0310	0.1773	0.0027	0.6240	1052.0	11.0	1052.0	15.0	1055	29	1055.0	29.0	0.3
PE17-086MOC_34	253.0	2.45	0.0267	0.0035	0.0041	0.0002	0.0200	26.5	3.5	26.3	1.0	10	220	26.3	1.0	0.8
PE17-086MOC_35	111.8	5.66	0.0309	0.0075	0.0041	0.0003	0.0428	30.3	7.3	26.1	2.0	30	400	26.1	2.0	13.9
PE17-086MOC_36	534.0	4.48	0.0231	0.0021	0.0038	0.0001	0.0199	23.1	2.1	24.4	0.7	10	160	24.4	0.7	5.5
PE17-086MOC_37	124.8	5.56	4.5600	0.1300	0.2683	0.0062	0.3778	1737.0	24.0	1531.0	32.0	2024	49	2024.0	49.0	24.4
PE17-086MOC_38	382.0	5.29	0.0257	0.0025	0.0040	0.0001	0.0603	25.6	2.5	25.6	0.8	20	170	25.6	0.8	0.1
PE17-086MOC_39	70.2	5.14	0.0555	0.0093	0.0080	0.0004	0.0149	54.7	9.1	51.6	2.7	80	270	51.6	2.7	5.7
PE17-086MOC_40	314.0	7.88	0.0740	0.0056	0.0110	0.0004	0.1902	72.0	5.2	70.3	2.3	120	130	70.3	2.3	2.4
PE17-086MOC_42	188.2	3.43	0.0258	0.0043	0.0036	0.0002	0.1082	26.1	4.3	23.4	1.1	0	260	23.4	1.1	10.3
PE17-086MOC_45	393.0	7.42	0.0738	0.0049	0.0108	0.0004	0.2059	72.0	4.7	69.5	2.4	180	130	69.5	2.4	3.5
PE17-086MOC_46	227.0	4.00	0.0273	0.0034	0.0043	0.0002	0.0664	27.1	3.4	27.8	1.1	10	210	27.8	1.1	2.6
PE17-086MOC_49	248.0	4.63	0.3350	0.0400	0.0462	0.0033	0.2235	293.0	31.0	291.0	20.0	350	310	291.0	20.0	0.7

PE17-086MOC_50	324.0	4.02	0.0269	0.0033	0.0042	0.0001	0.0965	26.7	3.3	26.7	0.9	40	200	26.7	0.9	0.1
PE17-086MOC_51	219.0	3.92	0.0272	0.0065	0.0041	0.0003	0.1496	27.0	6.3	26.3	1.6	30	360	26.3	1.6	2.6
PE17-086MOC_53	436.0	3.74	0.0265	0.0050	0.0036	0.0002	0.0430	26.4	4.9	22.9	1.5	200	330	22.9	1.5	13.3
PE17-086MOC_54	1381.0	3.62	0.0261	0.0013	0.0039	0.0001	0.0934	26.1	1.3	24.9	0.5	150	100	24.9	0.5	4.8
PE17-086MOC_56	434.8	3.88	0.0255	0.0022	0.0037	0.0001	0.0343	25.5	2.2	24.0	0.8	160	170	24.0	0.8	5.9
PE17-086MOC_58	484.0	1.37	0.0300	0.0044	0.0042	0.0002	0.2503	29.9	4.3	27.2	1.5	200	260	27.2	1.5	9.0
PE17-086MOC_60	424.0	6.40	0.3790	0.0360	0.0507	0.0033	0.7203	325.0	27.0	319.0	20.0	330	160	319.0	20.0	1.8
PE17-086MOC_61	419.0	11.10	0.5180	0.0310	0.0687	0.0027	0.0639	423.0	21.0	428.0	16.0	430	150	428.0	16.0	1.2
PE17-086MOC_63	345.0	3.61	0.0238	0.0026	0.0038	0.0001	0.0564	23.8	2.6	24.2	0.8	20	180	24.2	0.8	1.5
PE17-086MOC_64	676.0	3.45	0.0241	0.0025	0.0036	0.0001	0.1122	24.1	2.5	23.4	0.9	100	190	23.4	0.9	3.1
PE17-086MOC_66	430.0	2.80	0.0301	0.0028	0.0040	0.0001	0.1538	30.0	2.8	25.9	0.7	320	180	25.9	0.7	13.7
PE17-086MOC_67	2100.0	4.18	0.0807	0.0043	0.0117	0.0005	0.4257	78.7	4.1	74.8	3.0	230	130	74.8	3.0	5.0
PE17-086MOC_68	293.7	5.94	0.8810	0.0200	0.1038	0.0013	0.3347	640.0	11.0	636.6	7.8	643	51	636.6	7.8	0.5
PE17-086MOC_69	462.0	7.93	0.0747	0.0096	0.0109	0.0003	0.0604	72.9	9.1	69.9	2.0	200	250	69.9	2.0	4.1
PE17-086MOC_70	139.1	6.23	0.0283	0.0067	0.0038	0.0002	0.0012	27.9	6.5	24.4	1.5	60	380	24.4	1.5	12.5
PE17-086MOC_74	47.6	7.73	2.3700	0.1800	0.2090	0.0100	0.1833	1220.0	55.0	1219.0	54.0	1240	170	1240.0	170.0	1.7
PE17-086MOC_76	927.0	2.47	0.0255	0.0024	0.0039	0.0001	0.1266	25.5	2.4	25.2	0.8	90	180	25.2	0.8	1.1
PE17-086MOC_77	390.4	4.62	0.0281	0.0027	0.0042	0.0002	0.0876	28.4	2.7	26.8	1.0	150	170	26.8	1.0	5.6
PE17-086MOC_78	572.0	5.15	0.0259	0.0030	0.0038	0.0002	0.1941	25.8	3.0	24.3	1.1	110	200	24.3	1.1	5.8
PE17-086MOC_79	155.4	15.40	1.8740	0.0710	0.1814	0.0043	0.4145	1068.0	25.0	1074.0	24.0	1058	71	1058.0	71.0	1.5
PE17-086MOC_81	422.0	7.29	1.0770	0.0290	0.1202	0.0029	0.6754	739.0	14.0	731.0	17.0	754	46	731.0	17.0	1.1
PE17-086MOC_82	113.9	3.76	0.0322	0.0076	0.0039	0.0003	0.0059	31.5	7.4	25.3	2.1	230	410	25.3	2.1	19.7
PE17-086MOC_84	132.6	10.06	0.7640	0.0370	0.0933	0.0024	0.1510	574.0	21.0	575.0	14.0	580	110	575.0	14.0	0.2
PE17-086MOC_85	665.0	8.24	0.0761	0.0034	0.0112	0.0002	0.0588	74.3	3.2	72.0	1.2	145	89	72.0	1.2	3.1

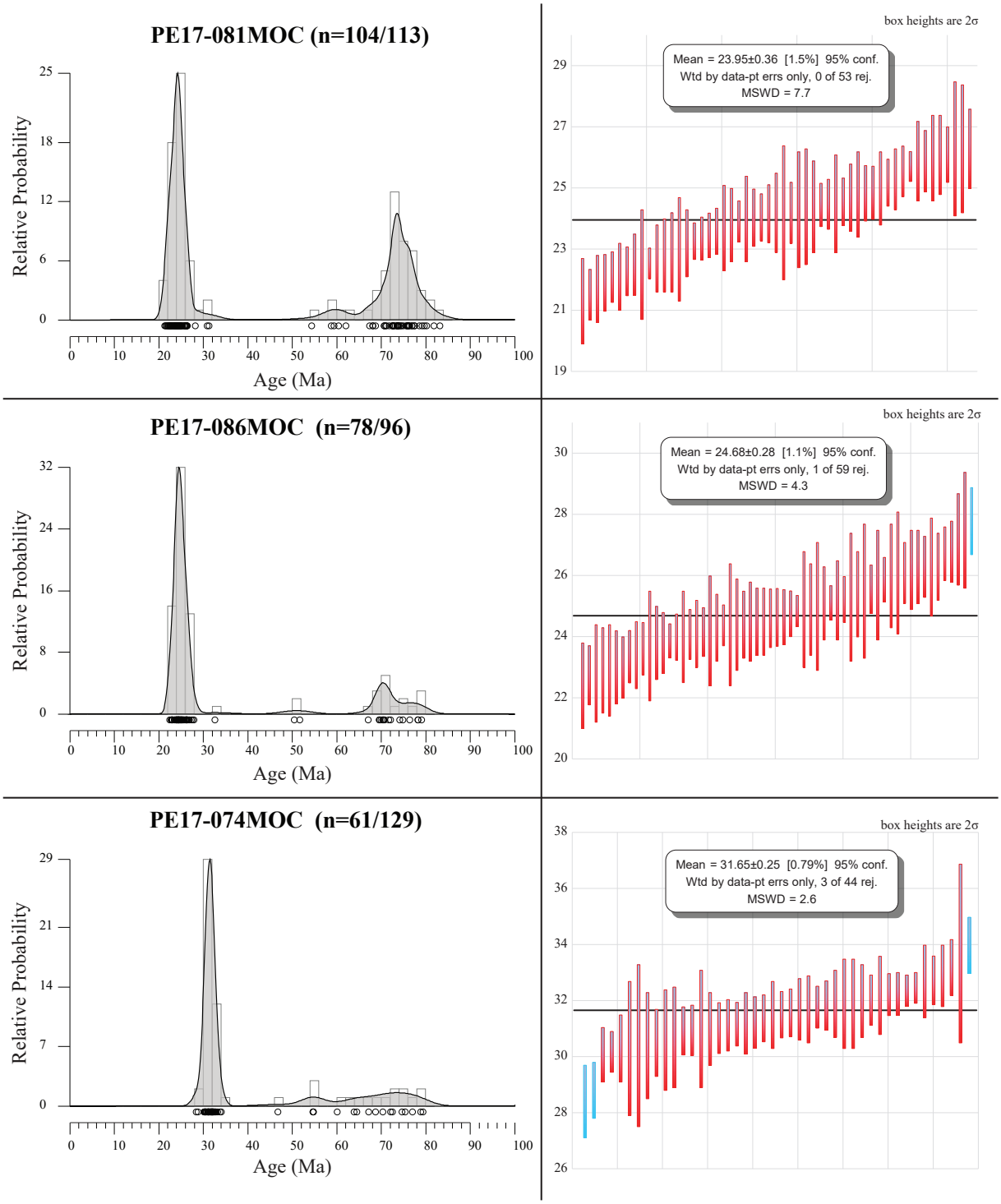
PE17-081MOC (n=104/113)
Relative Probability
Age (Ma)
box heights are 2σ
Mean = 23.95±0.36 [1.5%] 95% conf.
Wtd by data-pt errs only, 0 of 53 rej.
MSWD = 7.7
PE17-086MOC (n=78/96)
Relative Probability
Age (Ma)
box heights are 2σ
Mean = 24.68±0.28 [1.1%] 95% conf.
Wtd by data-pt errs only, 1 of 59 rej.
MSWD = 4.3
PE17-074MOC (n=61/129)
Relative Probability
Age (Ma)
box heights are 2σ
Mean = 31.65±0.25 [0.79%] 95% conf.
Wtd by data-pt errs only, 3 of 44 rej.
MSWD = 2.6

PE17-086MOC

PE17-081MOC

PE17-074MOC

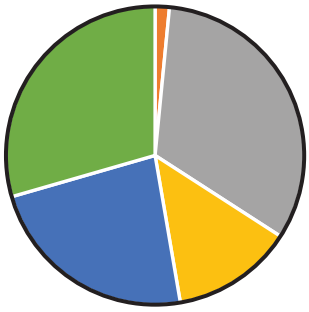

Detrital Zircon U-Pb Age Group

- Huayilillas Arc (24–10 Ma)
- Tacaza Arc (30–24 Ma)
- Andahuaylas-Anta Arc (45–30 Ma)
- Toqupala Arc (91–45 Ma)
- Chocolate Arc (310–91 Ma)
- Accreted terrane and orogenic sediments >310 Ma

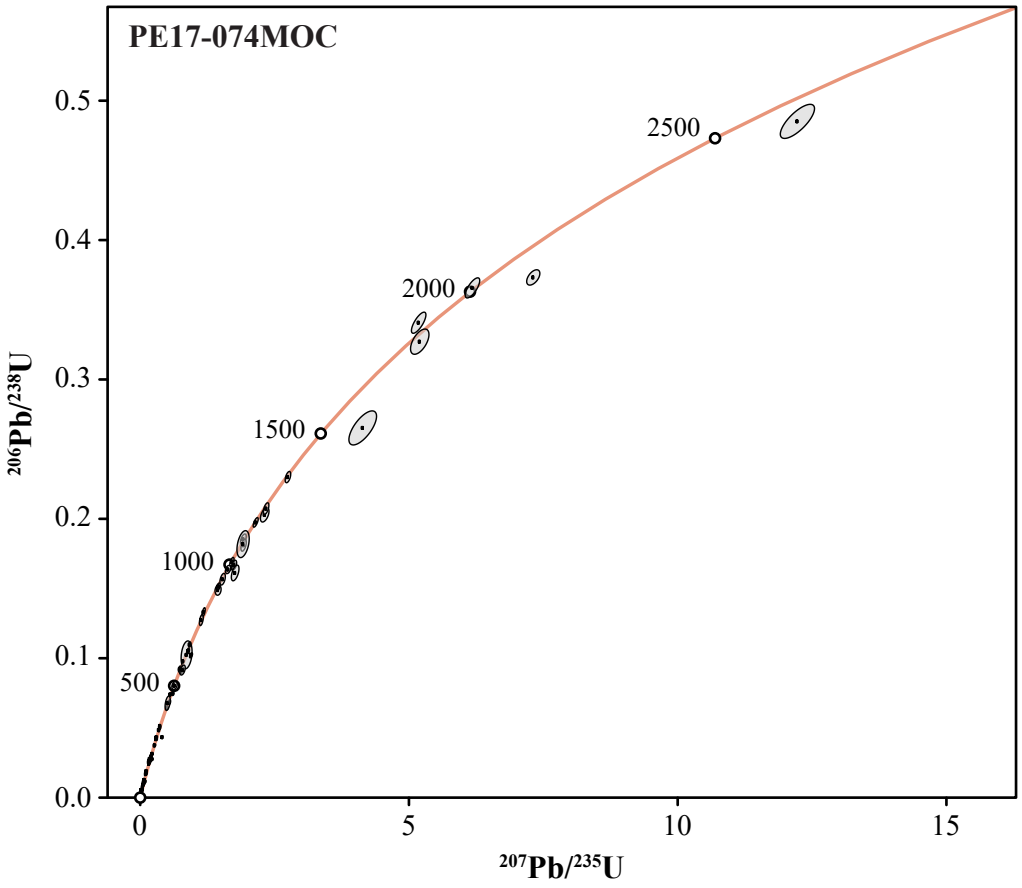
PE17-074MOC
0.5
0.4
0.3
0.2
0.1
0.0
0
5
10
15
2500
2000
1500
1000
500
206Pb/238U
207Pb/235U

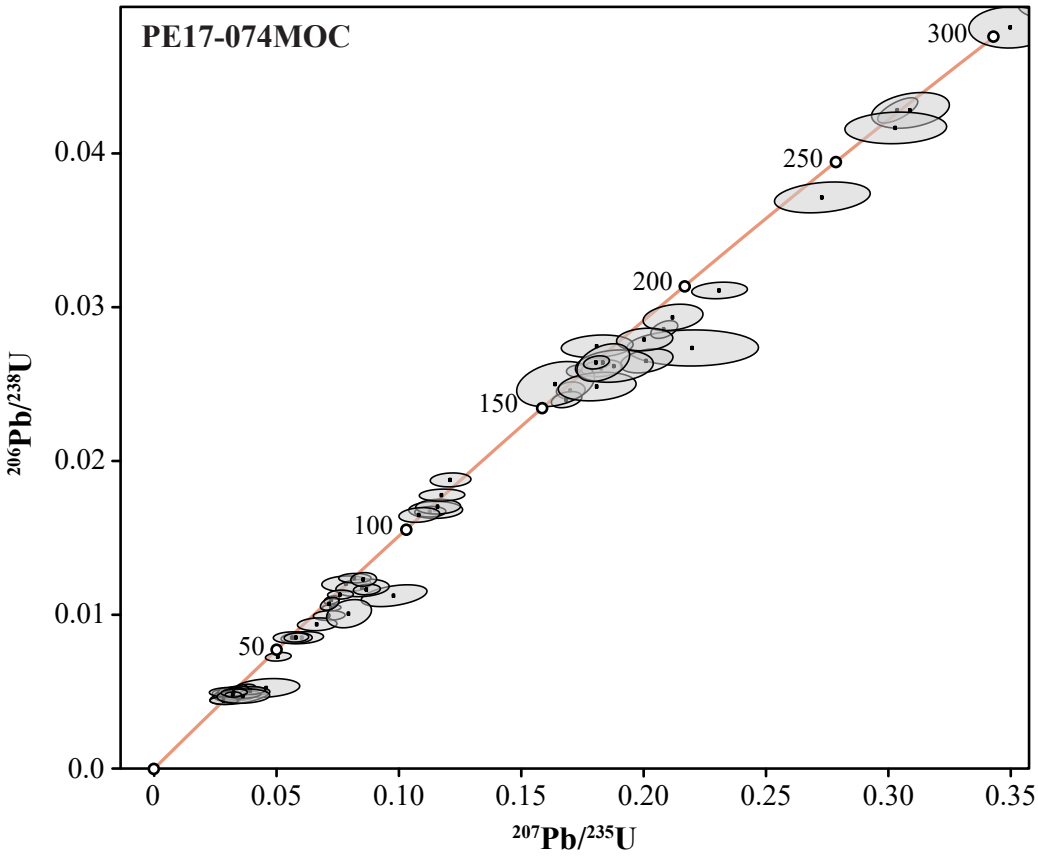
PE17-074MOC
300
250
200
150
100
50
0.04
0.03
0.02
0.01
0.0
0
0.05
0.10
0.15
0.20
0.25
0.30
0.35
206Pb/238U
207Pb/235U

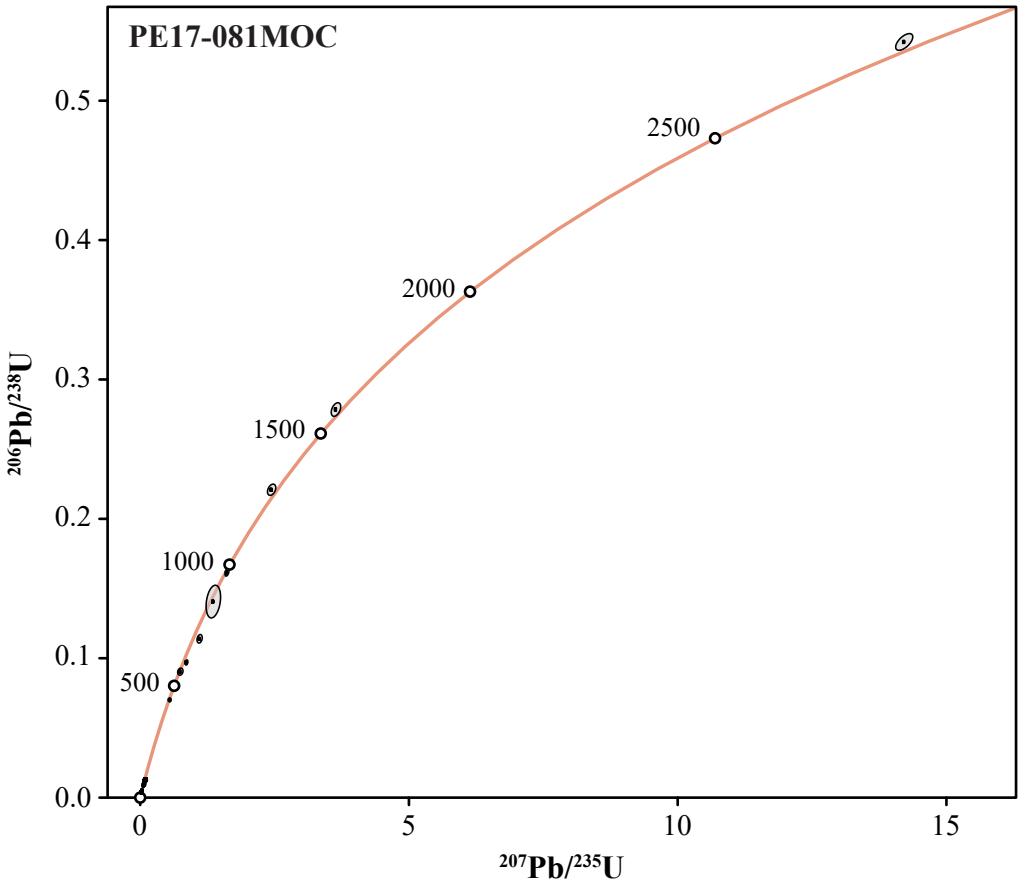
PE17-081MOC
0.5
0.4
0.3
0.2
0.1
0.0
206Pb/238U
2500
2000
1500
1000
500
0
5
10
15
207Pb/235U

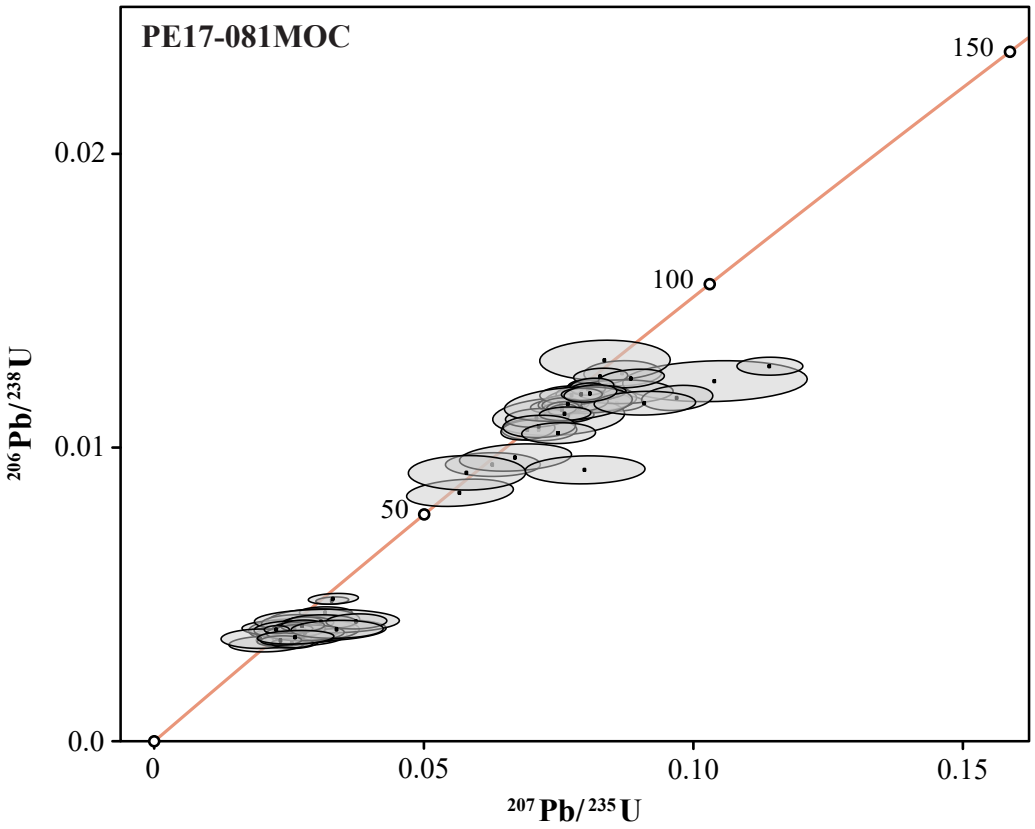
PE17-081MOC
150
100
50
0.02
0.01
0.0
0
0.05
0.10
0.15
$^{206}Pb/^{238}U$
$^{207}Pb/^{235}U$

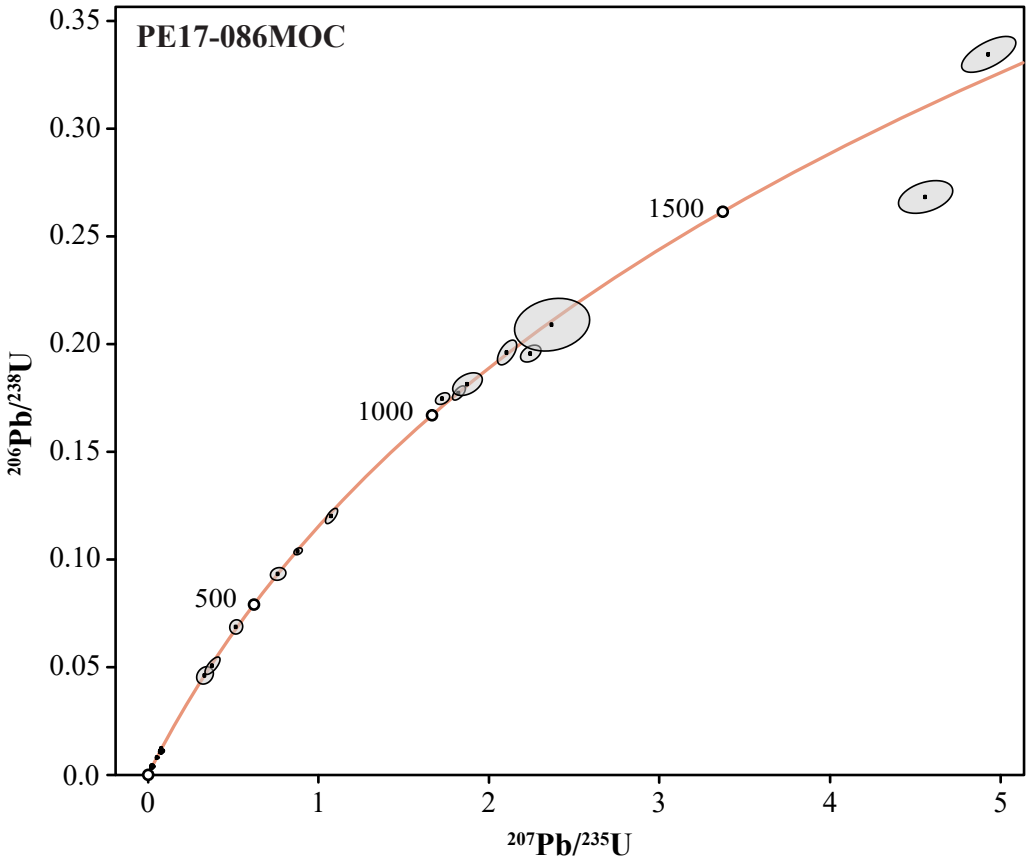
PE17-086MOC
0.35
0.30
0.25
0.20
0.15
0.10
0.05
0.0
0
1
2
3
4
5
500
1000
1500
$^{206}Pb/^{238}U$
$^{207}Pb/^{235}U$

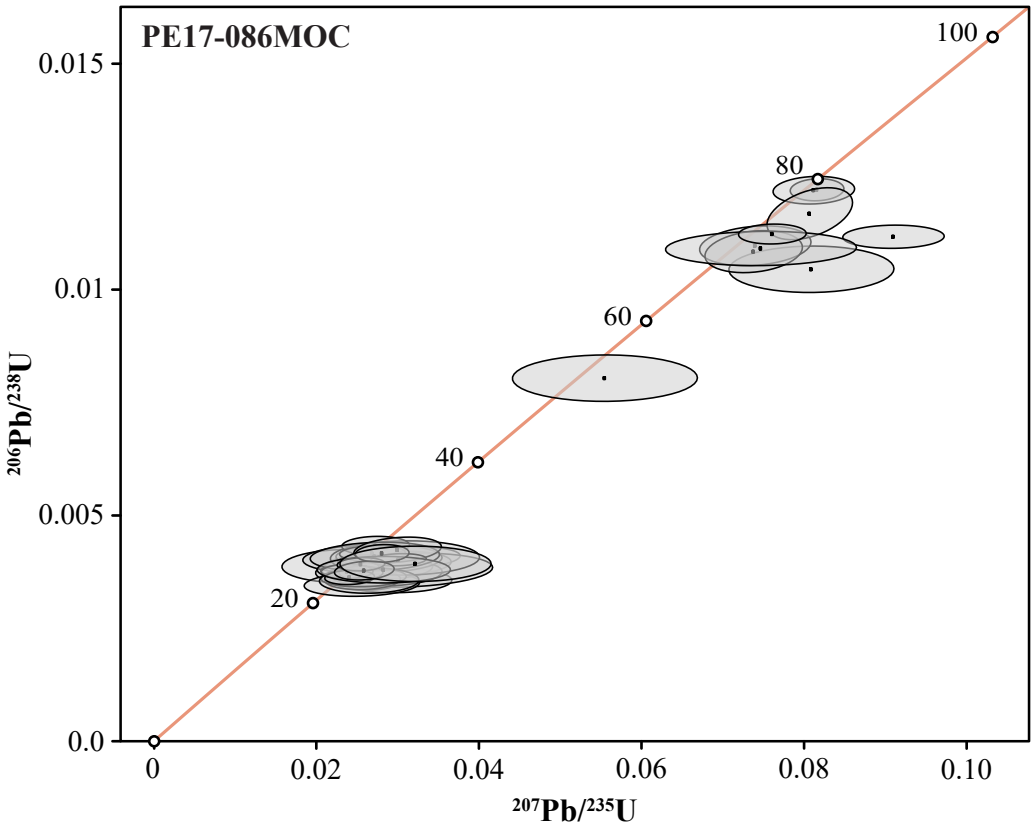
PE17-086MOC
100
80
60
40
20
0.015
0.01
0.005
0.0
0
0.02
0.04
0.06
0.08
0.10
206Pb/238U
207Pb/235U

Miocene Corire Stratigraphy

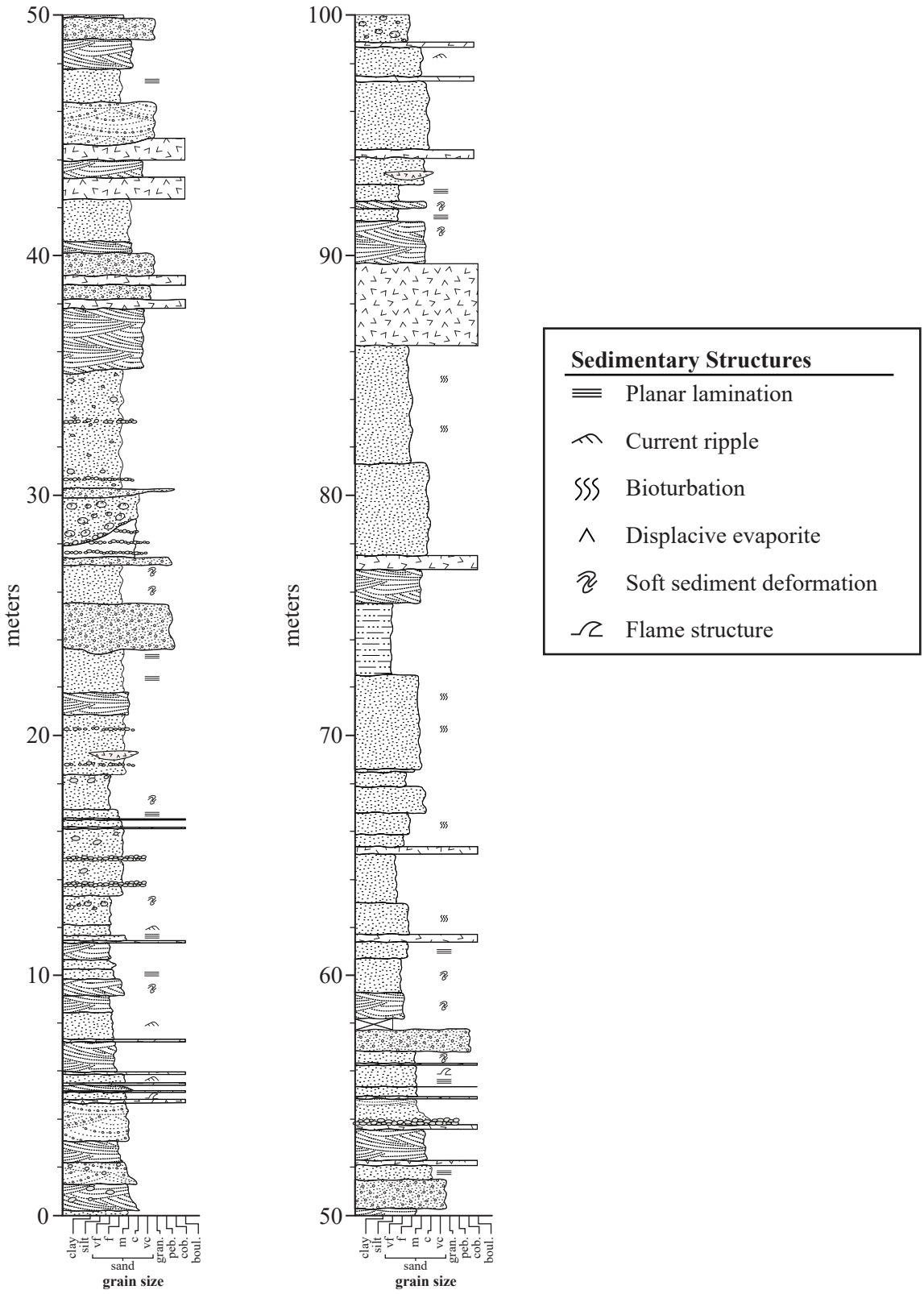

Miocene Corire Stratigraphy

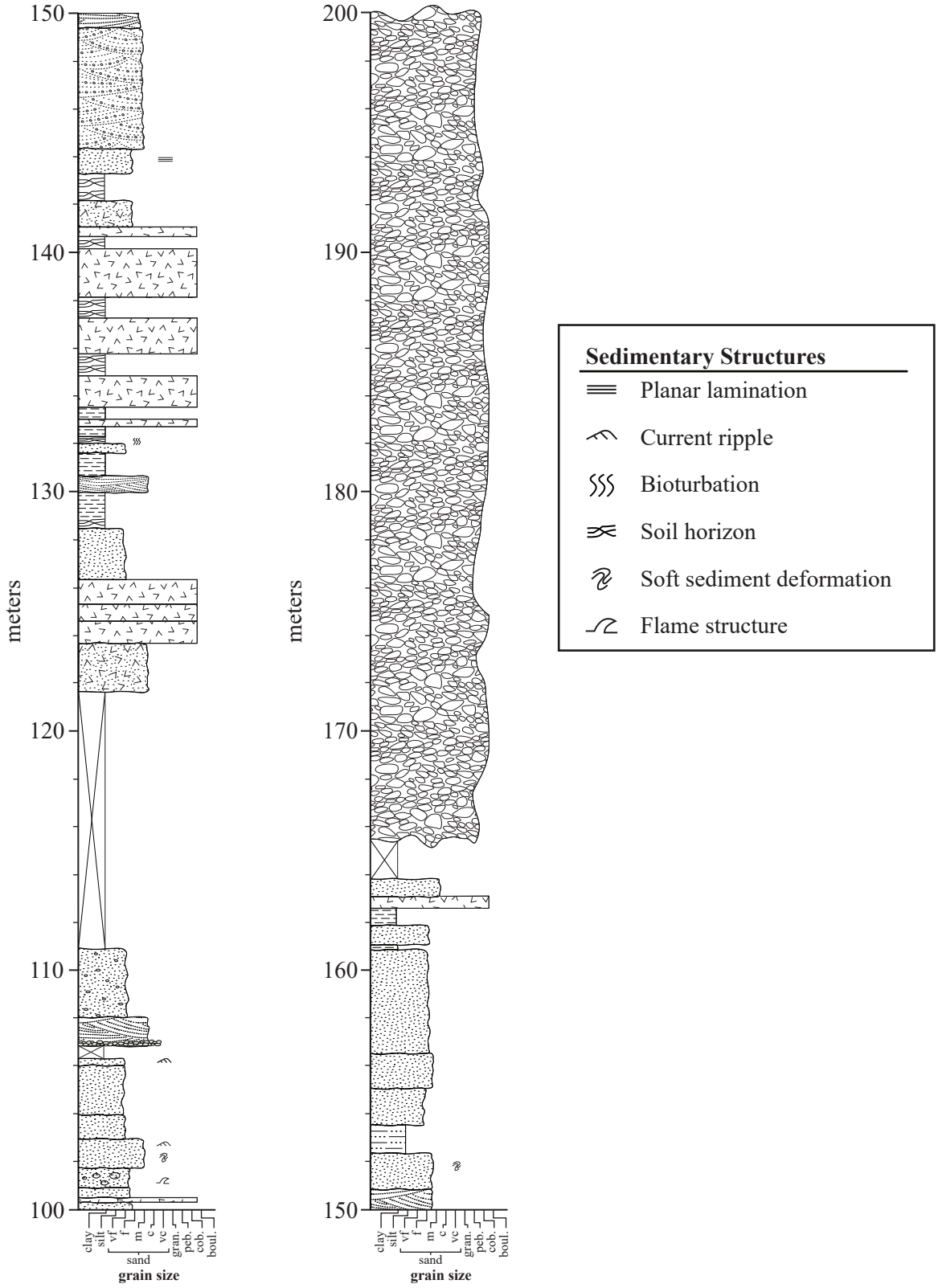

Miocene Moquegua Basin Stratigraphy

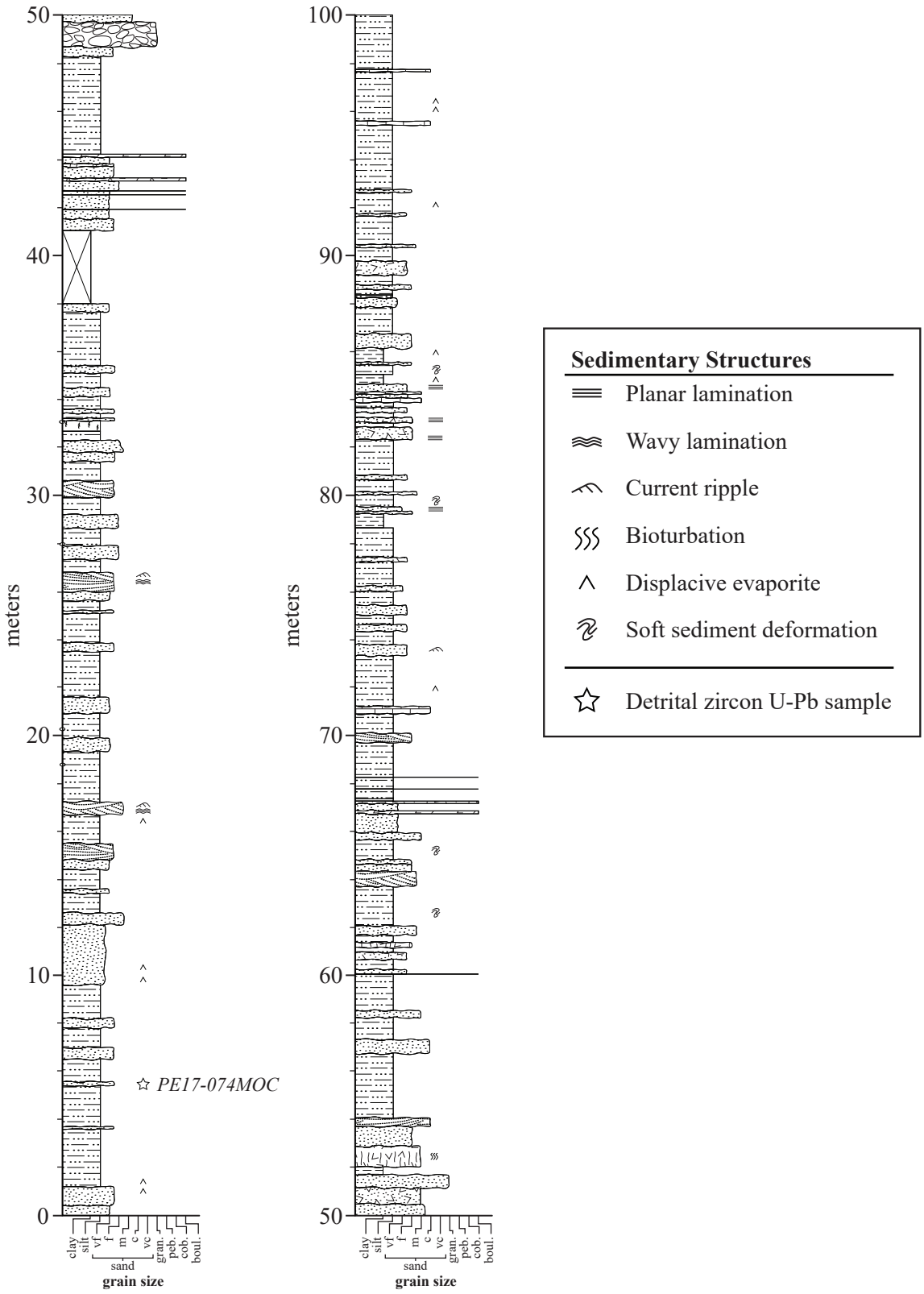

Miocene Moquegua Basin Stratigraphy

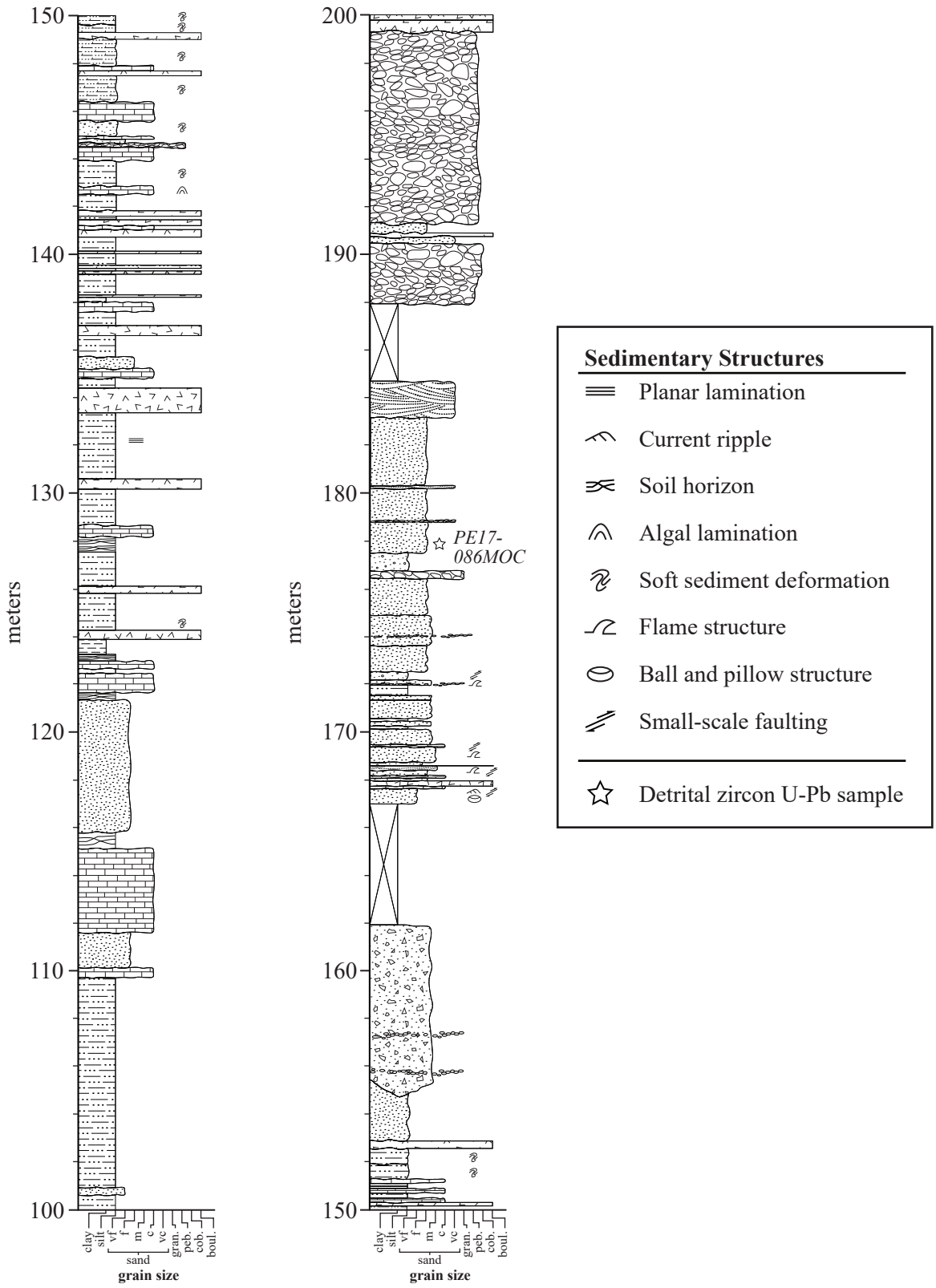

Miocene Moquegua Basin Stratigraphy